Integrated Fluorescence Detection System for Lab on a Chip Devices

by

Keith Mo

A thesis
presented to the University of Waterloo
in fulfilment of the
thesis requirement for the degree of
Master of Applied Science
in
Systems Design Engineering

Waterloo, Ontario, Canada, 2007

I hereby declare that I am the sole author of this thesis. This is a true copy of the thesis, including any required final revisions, as accepted by my examiners.

I understand that my thesis may be made electronically available to the public.

Abstract

This thesis focuses on the design of a versatile, portable, and cost-effective fluorescence detection system for LOC devices. Components that are widely available are used, such as LEDs for excitation and a microcontroller for processing. In addition, a photoresistor is tested for the feasibility of being used as a fluorescence detector, instead of the more commonly used photomultiplier tubes. The device also focuses on upgradeability and versatility, meaning that most of the major components can be replaced as long as power requirements remain unaffected. This allows for future additions to the device once they are available, as well as giving the user the power to choose which add-ons are needed since not all users may have the same requirements. The performance of the device after testing with fluorescein dyes and stained yeast cells indicate that it is capable of executing simple tasks, such as determining the presence and concentration of an analyte if given a sufficient amount. It also provided similar readings to commercial fluorescence analysers, which proves its ability to function as a fluorescence detector device.

The thesis also proposes a MEMS diffraction grating that can be used for wavelength tuning. By being able to selectively measure across a range of wavelengths, the capability of the device is increased. Examples include being able to detect multiple fluorescent emissions, which will complement the multicoloured excitation LED nicely. In addition, the device will not be limited to a predetermined set of filters. This effectively allows more fluorescent dyes to be used with the device since any wavelength in the visible range can be selectively filtered for. Simulations of the proposed diffraction grating were performed in ANSYS to confirm the validity of the calculated values. In addition, tests were performed on a slide fabricated with diffraction gratings using values as close to the calculated values as possible. All of the results indicate that there is great promise in the proposed diffraction grating design and that it should be further investigated.

Acknowledgements

I would like to thank my supervisor, Dr. John Yeow, for his support and faith in my abilities. He has given me the opportunity to expand my knowledge and helped me grow as an individual. The experience I gained during my Masters program is something that I will always be able to draw upon, for which I am grateful. I would also like to thank Dr. Perry Chou and Dr. William W. Melek for taking the time to be my thesis readers. Many thanks to Dr. Perry Chou, Dr. Jean Duhamel, and their respective labs, as well as Zhenyu Cheng for helping me prepare my fluorescent and biological samples.

My friends and members of my lab have also played a big role in helping me stay focused and pointed me in the right direction when needed.

Finally, big thanks to my family for their patience, support, and for helping me keep sight of what is truly important.

Contents

List of Tables

List of Figures

Chapter 1

Introduction

The continued advancements in technology have typically resulted in a better quality of life for the general population. With developments in wireless technologies and the Internet, people are now accustomed to the idea of service on demand. It is now possible for a person to instantly communicate with others via cell phones or access the vast database of information from almost anywhere in the world. This notion is also perpetuated by the fast paced lifestyle that is becoming more predominant in today's society. Consequently, it should be of no surprise for the general population to expect most services to respond in a timely fashion. This is especially true for medical services, which is normally one of the main indicators of the quality of life. As society grows, it is expected of the medical community to keep pace with the advancements and ensure that the well-being of the population is maintained. Unfortunately, the increase in population, improved accessibility, and the emergence of new diseases are beginning to adversely impact parts of the medical sector.

One of the challenges being faced by the medical sector today is to maintain

or improve their current level of service while minimizing the operating cost due to limited funds. This means that they cannot just acquire additional personnel and equipment to account for any rise in demand. The result of this is that if there is an increase in the number of patients, then a virtual bottleneck may be formed since the number of resources available will still remain the same. For example, some biological samples have to be processed at a central laboratory due to their requirements of specialized equipments and materials, as well as trained technicians for their proper operation. But these laboratories are typically responsible for servicing several clinics in the region. With an increase in patients and a corresponding increase in samples, there may now be an accumulation of tests that must be performed. Even if there is no backlog, both the physician and the patient must still wait for the sample to be delivered to the facility and processed. It is not uncommon to have to wait for a week before results are obtained and an accurate diagnosis can be made. This wait time is unacceptable, especially if immediate urgent care is needed. A procedure normally encountered by a patient is shown in figure 1.1: It outlines two possible scenarios that patients at a clinic may encounter. The first scenario is that the physician can accurately diagnose the illness and prescribe the proper medication. If the physician is not certain of the illness, then medication may still be prescribed based on the symptoms observed, as well as the most probable illness at the time. For example, if several local residents exhibit the same symptoms, then there is a greater chance that the patient also has the same illness. However, prescribing medication in this fashion may not be prudent amidst growing concerns of antibiotic resistant pathogens. In order for the physician to be certain, test samples must be obtained and sent to the laboratories to be processed, which is listed in the second scenario. By the time the results are obtained, the patient might have already recovered or, in the worst case, the

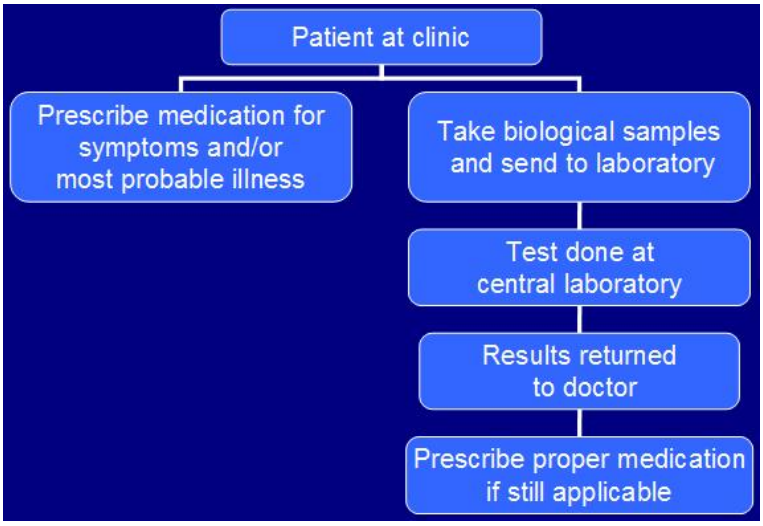

Figure 1.1: Typical scenario currently encountered by patients and their physicians at clinics.

condition might have worsened. Consequently, it is desirable to minimize this wait time if possible. Fortunately, several possible solutions exist, one of which is the popularized Lab-On-a-Chip (LOC) device.

1.1 Motivation

A LOC device is a fitting solution to the previously described problem in this technological day and age since it can apply various technologies and concepts from different disciplines. It is typically composed of sample inlets and outlets, sample amplification units (such as for polymerase chain reaction or PCR), reaction chambers, and a detection mechanism. That means they require proper design in terms of materials, structures, fluidics, and signal processing. Ideally, the LOCs should be small, portable, easy to use, and inexpensive. These properties are

in direct contrast to the currently used biological analysers, which are typically large, expensive, and may require specially trained personnel to properly operate them [1]. This does not mean that the commercial analysers currently being used are inferior and should be replaced. In fact, it is usually because they are capable of performing a wide variety of tasks that they are expensive and require skilled users. Consequently, the equipment might be used for both simple as well as complex analysis. This is an inefficient use of costly machines and skilled technicians, and can be remedied by specifically designed LOCs. By designing various LOCs to do some of the simple tests that are currently being performed by the commercial analysers at the main laboratories, their use can help alleviate the burden placed on these facilities and improve patient care in terms of the speed of diagnosis [2]. LOCs will effectively enable pipelining by allowing for the parallel processing of biological samples. Part of this concept is demonstrated in figure 1.2. Since LOCs are ideally easy to use and portable, anyone can use the device anywhere. By using LOC devices, a physician may now be able to directly perform tests on the sample at the clinic or in the field. The physician only has to send samples to the laboratory when the LOC device is not able to perform the test. The total operating cost will also be reduced since laboratory technicians can now focus on executing tests that are beyond the capabilities of LOCs. In addition, because of the minimalist nature of LOCs, smaller amounts of reagents and samples are required, which will also result in a corresponding decrease in wastes or by-products. The overall outcome of all this is a lower operating cost as expensive resources are better utilized, and fewer accessories and consumables are needed [3].

Currently, a variety of biological tests being performed are based on the principle of fluorescence. Although there are several other detection methods, such as those based on chemical, thermal, or electrical properties, optical detectors are

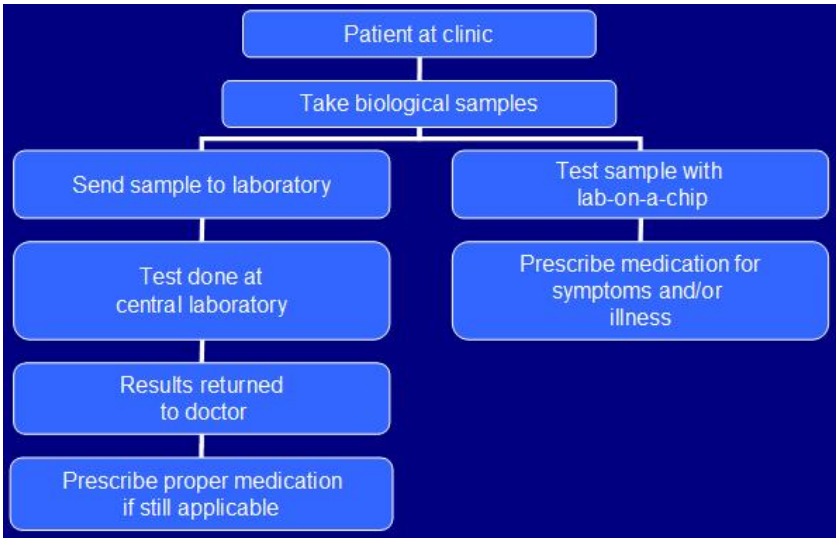

Figure 1.2: LOCs enable on-site diagnosis by the physician, thus providing an alternate avenue for diagnosis.

predominant due to their sensitivity and repeatability [1]. Applications of these tests can include determining the presence and concentrations of pathogens, cells, nucleic acids, and proteins. Identification is also possible by targeting for specific antibodies that are unique to the specimen and monitoring for a corresponding fluorescent response. An example of an application of fluorescence is the Enzyme-Linked Immunosorbent Assay (ELISA). In the case of ELISA, antibodies specific to the desired antigens are attached to multiple wells. The wells are then flooded with various reagents, biological samples and rinsed, after which a second batch of antibodies are then washed over the samples. Since antibodies normally only interact with their corresponding antigens, if the targeted antigen is present in the initial solution, then they will adhere to their antibody counterpart and remain in the well after rinsing. The second set of antibodies that are then applied over the newly formed antibody and antigen complex have enzymes linked to them. These

antibodies will attach to the complex and their enzymes will react with a substrate, that is subsequently added for fluorescence. The fluorescent signal can then be detected by various photodetectors or by visual inspection under a microscope. Therefore, as a result of their numerous applications, a fluorescence detection system for LOC devices is the focus of this thesis. By helping to bring the fluorescence detection capability to LOC devices, it is hoped that the full potential of LOCs can be realized.

1.2 Research Objectives

There are two main objectives for this thesis, and they are summarized as follows:

- *To design and build a prototype fluorescence detection system*
  Since fluorescence detection systems are of significant importance in terms of biological analysis, one of the main goals of this thesis is to design and build a working prototype. Thus, it shall be demonstrated that it is possible to create a self-sufficient fluorescence detection system while using only cost-effective solutions. The proposed system will be consistent with the overall ideology of LOC devices in terms of portability and low cost. It should be noted here that for the time being, the proposed device is only designed to complement existing analysers. As a result, it only needs to be able to perform simple measurements to allow expensive analysers to focus on more complex tasks.

- *To introduce a MicroElectroMechanical System (MEMS) based diffraction grating*
  A MEMS based diffraction grating will also be introduced as a method for wavelength tuning. The objective is to demonstrate the feasibility of the con-

cept of using a MEMS diffraction grating for the purpose proposed above. MEMS technology is suggested since MEMS based devices have the potential of keeping cost and size to a minimum, both of which are ideal for LOC devices.

1.3 Contributions

The research objectives previously listed are designed to produce the following general contributions:

- *Introduce a cost-effective, versatile, integrated fluorescence detection system*
  There are already numerous developments in terms of a fluorescence detection system for LOC devices. However, they are usually focused on one particular aspect of the system, as will be shown in later sections. As a result, one of the main goals is to further their research and design a completely self-sufficient system such that they can be used anywhere. This contribution should greatly help in realizing a fully developed LOC device.

- *Propose and simulate a MEMS based diffraction grating for LOC devices*
  One feature that will greatly enhance the versatility of optical based LOC devices is the ability to detect different wavelengths. This ability can be achieved in a variety of ways. Possible solutions range from using a selection of fixed filters, such as a filter wheel, to wavelength tuning based on the principles of interferometers or diffraction gratings. Through indirect tests and simulations, it will be shown that a MEMS diffraction grating is a viable solution.

1.4 Outline

The remainder of this thesis is divided up into four sections, and they are described in the following:

- *Chapter 2 - Literature Review*

  This section is used to give a brief discussion about previous developments already achieved in the field. It is important to establish in the readers a basic understanding of the current progress in terms of fluorescence detection systems for LOC devices. This will also make it easier to identify the contributions presented in this thesis. Although the majority of this section will be devoted to both visible fluorescence detection systems and MEMS diffraction gratings, other similar topics will also be briefly examined to attempt to provide a complete overview. A generic overview is required since it is greatly hoped that by introducing the background in this section, the reader will be encouraged to explore other similar works. There are numerous accomplishments in the field that are both exciting and illuminating, and should be studied by those interested.

- *Chapter 3 - Fluorescence Detector Design*

  In this section, the basic background theories of some of the different components used in the device are reviewed. Insights into the design of the device will also be provided, such as reasons why one particular component was chosen over another. A phenomenon known as the inner-filter effect will also be introduced since it will help explain and evaluate the performance of the device. The section will also include experimental results in the form of graphs and tables. The results obtained by the fluorescence detection system are also

compared with measurements provided by other commercial devices to assess its capabilities. Errors and discrepancies between different measurements will also be examined to help understand the limitations of the system.

- *Chapter 4 - Diffraction Grating Design*

  The basic theory of diffraction gratings and the fabrication process involved will be covered in this section. This is to help the reader become familiar with the design, as well as to understand the purpose of the MEMS diffraction grating proposed in this thesis. By implementing a diffraction grating similar to the suggested design, it is hoped that the capability of the fluorescence detection system is increased. In addition to proposing a MEMS diffraction grating design, the overall diffraction concept is tested and the grating is simulated to demonstrate the feasibility of the idea. Calculated values are also used and compared to help determine the accuracy of the simulations and the design.

- *Chapter 5 - Conclusions and Future Work*

  This section will provide a brief summary of each of the results obtained from chapters 3 and 4. The main points are once again reviewed, and any errors or discrepancies encountered are discussed. Possible extensions or additions to the device in terms of future work will also be suggested to help bring about the realization of a true LOC device.

Chapter 2

Literature Review

2.1 Introduction

Since the field of LOC devices can encompass a wide variety of research, it is the goal of this literary review to narrow the scope to those that are most related to the contents of this thesis. The first section will cover some of the research related to a fluorescence detection system, ranging from individual components to complete systems. The second section deals with MEMS diffraction gratings and their applications, specifically wavelength tuning. It is hoped that the accomplishments discussed in this chapter will be sufficient for the reader to establish an understanding of the current developments and help identify the contributions of the thesis.

2.2 Fluorescence Detection Systems

Many of the biological tests and analyses being performed today are based on the principle of fluorescence. As a result, there is a significantly large amount of research in the field of fluorescence detection systems. A typical fluorescence instrument will consist of an excitation source and a detection unit. The excitation source is used to provide energy in the form of photons for the fluorophores to absorb, which will then radiate energies with longer wavelengths. This newly emitted wavelength is usually the subject of interest in fluorescence analyses. Current fluorescence instruments use high powered, high intensity excitation sources such as lasers and lamps. They are commonly found in microfluidic fluorescence experiments, in setups similar to those described in [4] and [5]. Unfortunately, these sources are also normally quite expensive, so another solution must be found if LOC devices are to remain inexpensive and portable. As a result, solutions such as using laser diodes or LEDs in fluorescent tests are becoming popular. Dasgupta *et al.* [6] even published a paper entitled "Light emitting diode-based detectors: Absorbance, fluorescence and spectroelectrochemical measurements in a planar flow-through cell" that reviewed various LED based detectors. Kuo *et al.* [7] also wrote a similar paper studying high power blue and UV LEDs for sensitive detection. They successfully implemented the LEDs for flow cytometry (for applications such as cell counting or determining cell properties), capillary electrophoresis or CE (for cell or analyte separation), as well as for the imaging of single-molecules [7]. Considering the fact that all of these are possible applications for LOC devices, their results show the feasibility of using LEDs as an alternative excitation source. The capability of LEDs is further investigated by Sakamoto *et al.* [8]. They studied the performance of the retail Agilent 2100 Bioanalyzer, which uses a 470 nm blue LED along with a 630 nm red

laser diode, for on-chip flow cytometry and concluded that the results were similar to those measured by direct microscopic count [8].

At least two groups have investigated the subject of tunable LEDs [9, 10]. The result is that instead of requiring several different band-pass filters in conjunction with a wide spectral light source, or having to include different coloured lasers or LEDs, only one LED is needed to provide different excitation wavelengths. This can help promote the use of these cost-effective and low power devices. Dodabalapur *et al.* [9] described a design whereby their LED is capable of emitting the three primary colours of blue, green, and red. Their LED is based on the theory of Fabry-Perot microcavity LEDs, where the thickness of the cavity determines the mode and the wavelength emitted. By adding a silicon nitride filler layer and then etching it down to different thicknesses, a microcavity with varying thickness can be achieved. Thus, specific wavelengths can be designed for by selecting thicknesses that will produce certain cavity lengths. Using this principle, Dodabalapur *et al.* designed a step-like filler layer, with each different step height corresponding to one of the three primary colours [9]. Although their research was not directly related to excitation sources for LOC devices, it is still highly applicable to the area. As previously mentioned, Chen *et al.* [10] have also proposed a tunable LED based on porous silicon. By taking advantage of the multiple energy states on the surface of a layer of porous silicon, they designed a device that could emit at peak wavelengths of 455, 590, and 675 nm when voltages of 80 to 90, 50, and 30 V were applied [10]. Although their results indicated that higher voltages will produce a greater amount of blue spectral emission [10], their research is still relevant since proper filters can be applied to select the desired wavelengths. Thus, a narrow spectral emission can still be achieved. Just from these two developments, it can be seen that there are already promising replacements for the expensive and high

powered sources that are currently being used. Using semiconductor solutions to provide a wide spectral bandwidth is highly attractive. The reason is that since the semiconductor industry is relatively well established, it is comparatively easier to mass produce semiconductor based optoelectronic solutions. This will also lower the overall cost in terms of manufacturing, and possibly simplify the design by allowing for the direct integration of optical components with electronic components. Semiconductor optoelectronics also usually have a longer lifetime than typical thermal and gas based light sources. This will also help further reduce the overall cost since the components do not have to be replaced as often. So for setups similar to those described in [4] and [5], it may translate into a considerable amount of savings. Consequently, even if some of these LEDs have difficulty providing a specific narrow spectral bandwidth, they are still feasible replacements. Additionally, being able to provide a wide selection of wavelengths is greatly desired since different fluorescent dyes may be designed to absorb different excitation wavelengths. The result is that in a complicated analysis where more than one fluorescent dye is used, two different excitation wavelengths may be required.

Although the development of inexpensive tunable light sources is quite important, a large number of developments related to fluorescence detection systems for LOC devices have been focused on both the detection aspect, as well as the overall system. In fact, researchers in the 1990s were already building their own fluorescence systems to be used for their experiments. For example, Guttman [11] constructed an optical platform that consisted of a fibre optic bundle, a 532 nm Nd-YAG laser, a series of lens and filters, an avalanche photodiode (APD), readout electronics, and a computer for monitoring fluorescence in electrophoresis. He collected the excitation light from the laser with a pair of aspheric lens and a filter into a fibre optic cable, which was then surrounded with collecting fibres and formed

into a bundle [11]. This bundle acted as a waveguide for both the excitation light, as well as the fluorescent light traveling in the outer collecting fibres. Using the bundle also simplified the alignment process since, by adjusting the lens system to focus the excitation light onto the sample, the same lens system will now also direct the fluorescent light back into the surrounding collection fibres. As his setup was designed to monitor fluorescence during electrophoresis, he demonstrated the viability of using such components in a fluorescence system. Years later, a paper titled "An integrated microfluidic device in polyester for electrophoretic analysis of amino acids" was written by Guo *et al.* [12]. Their results show how much have progressed when comparing their device as they were able to embed a 479 nm blue LED and a collecting fibre connected to a photomultiplier tube (PMT) into a microfluidic chip, removing the need for many optical components. With the sensitivity of a PMT detector, a detection limit of 0.5 mM of phenylalanine was achieved [12]. Irawan *et al* [13] also constructed a similar device, but optical components such as objective lens, convex lens, and filters are required in addition to their CCD detector. Using a 470 nm blue LED, they investigated a phenomenon known as the inner-filter effect, which will be discussed in detail in a later section. Using all of the previously listed components, they achieved a detection limit of 1 to 1000 μg/L of fluorescein in their mylar-D chip [13]. They also investigated crosstalk if there are multiple fluidic channels present since multiple excitations may occur, which is something that should be considered. It should also be noted that fluorescein is a commonly used green fluorescent dye in these types of experiments, so it will also be used as the fluorescent sample for this thesis. Schult *et al.* [14] also published a paper on an optical sensor system for immunochemical assays. Their device consisted of a disposable sensor chip made of primarily polymethylmethacrylate (PMMA) as well as an optical readout device composed of a 638 nm laser diode, a prism, a set of

lens, an optical filter, and a PMT [14]. An advantage of their system is the ability to rapidly measure different samples with the use of a disposable chip. In addition, since their system is based on evanescent field excitation, washing or separation steps during sample preparation and analysis are not mandatory [14]. However, although their device is well suited for certain applications, it has still yet to be determined how the device will respond under different excitation and fluorescent wavelengths. Portable fluorescence instruments capable of multiple wavelength detections have been proposed though. There are several reasons for this feature. In addition to allowing for a wider variety of biological reagents or fluorescent dyes to be used, characteristics based on specific windows or emission ranges can be identified. An example of an instrument capable of this is a duo wavelength fluorescence device developed by Barócsi *et al.* [15] to measure chlorophyll fluorescence. It includes a 635 nm laser diode, optical fibres, two PIN photodiodes, interference filters, LCD display, and a single board computer (SBC) for processing [15]. The filters are used to help observe fluorescence at 690 and 735 nm since the ratio of those two wavelengths for fluorescing chlorophylls are of importance [15]. By adding the LCD display and a SBC, they have helped make the device portable and self-sufficient. Measurements can now be performed on-site without requiring any additional equipment. Thus their fluorescence measurement system demonstrates how it is possible to design the instrument for different applications by simply choosing the corresponding excitation and emission wavelengths.

Minor alterations to fluorescence microscopes or systems, such as the one in [4], are also quite common. Yan *et al.* used an inverted fluorescence microscope along with a photon counter and PMT to achieve high sensitivity [5], but at the cost of using expensive components. Lacoste *et al.* [16] constructed a confocal microscope capable of multicolour scanning by adding either a dichroic mirror with two APDs,

or a diffractive element, such as a prism, and a detector array. Years later, Ocvirk *et al.* [17] developed a similar optical setup using a laser and a PMT. It can be seen that while their microfluidic part is relatively small, the optical components are still large and complex, thus making it costly. The need for such systems suggests that if it is possible to implement similar capabilities in a LOC fluorescence detection system, then perhaps the same analysis can be performed by the LOC device. This transferring of their ability of multicolour detection to a portable fluorescence detection system is one of the main objectives of this thesis, and will be discussed in a later section. A portable fluorescence instrument capable of both multicolour excitation and detection was developed shortly after Lacoste by Belgrader *et al.* [2]. They built a real-time PCR device that can analyse nucleic acids using fluorescence. It is composed of four InGaN LEDs to provide excitation wavelengths at 470, 510, 540, and 574 nm, as well as four photodiodes to detect emission wavelengths at 520, 550, 585, and 628 nm with the use of lens and filters [2]. Although their device is battery operated, allowing it to be used on-site, it still needs to be interfaced with a notebook computer for processing and readout. So while their instrument is highly compatible for their applications, it is not truly self-sufficient due to the need of an external readout system such as the notebook computer. Reports of other portable PCR devices were published a couple of years later by Higgins *et al.* [18], Lagally *et al.* [19], and Cady *et al.* [20]. Higgins' group constructed a handheld nucleic acid analyser that consisted of two LEDs (490 and 525 nm), a detector, an Intel microchip, a built-in display system, and a 12 V battery pack [18]. With all these components, their device is truly portable and self-sufficient. But while their device works well for their application, they are limited to the two excitation wavelengths. Lagally's group built an integrated portable genetic analysis system that was comprised of a 488 nm laser diode and a PMT for a limit of detection of a

few bacterial cells [19]. However, they require the use of an external readout system since the built-in display is for PMT voltage settings only. Still, it is impressive in terms of helping to make a typical tabletop fluorescence instrument more portable. The PCR system for bacteria detection developed by Cady *et al.* also uses a PMT for detection, but it uses a 480 nm blue LED for excitation [20]. Using these components, its limit of detection is approximately 2×10^3 cells when measuring *S. typhimurium* stained with SYBR green fluorescent dye [20].

Another evidence of the transition towards a more portable fluorescence detection system is the setup used by Ng *et al.* [21]. For their microfluidic system, a blue LED with a fibre optic cable is implemented as the excitation source while an APD embedded in polydimethylsiloxane (PDMS) is used for the detection aspect [21]. This is similar to the instrument built by Belgrader *et al.*, but it should be capable of handling more applications since the device was designed with fewer constraints on the sample to be tested. However, like Belgrader's device, an off-chip system is required to process the detector's signal [21]. This type of setup is later demonstrated again in [22], where a computer is needed to read the PMT values, but with the difference that this time a HeNe laser is used instead of an LED. Wolff *et al.* [23] published a paper in the same journal about a fluorescence activated cell sorter, where the design is similar in terms of utilizing a microfluidic channel and PMT, except they used a mercury lamp as the light source instead. But if it is possible to replace the mercury lamp with LEDs or laser diodes, then there is a great possibility of creating a LOC device for that application. Additionally, a computer is again necessary to process the PMT. Fu *et al.* [24] also implemented a setup that used a mercury lamp for excitation, but used an APD and computer for detection and processing. This recurring issue of having to use an external readout device suggests that there is a need to remedy this general problem. Other

examples of this common setup include a flow cytometer developed by Wang *et al.* [25] and a micro-optical fluorescence detection system for microfluidic applications as described by Kruger *et al.* [26]. The flow cytometer by Wang's group uses a HeNe laser for 632.8 nm excitation, and PMTs for detection [25]. They were measuring the forward scattering, large angle scatter, and extinction signal of polystyrene beads to determine their properties, with the idea that the beads can mimic fluorescently dyed cells. The main drawback with their device is that like other devices with one or two laser diodes, the excitation wavelength is relatively limited. Kruger's device also requires the use of an external computer for signal processing, an APD for detection, and they also use either laser diodes or InGaN LEDs for fluorescence excitation [26]. In addition to what appears to be a popular recurring theme of a combination of photodiodes and LEDs, they have also implemented micro-lenses, micro-prisms, and diffraction gratings for leaky waveguide coupling in their device [26]. These optical devices can help collect and focus wavelengths of interest onto both the sample and the detector. It is interesting to note their use of a holographic diffraction grating for coupling, since the diffraction grating aspect is also being proposed as a major component for the device presented in this thesis. However, for the thesis, the diffraction grating is used for spectral separation, which will be described in detail in a later chapter. It should be noted that photodiodes and APDs are not the only solution. There is research on photodiode arrays and related detectors for on-chip analysis, such as one performed by Iordanov *et al.* [27] for an integrated sensor array. Chiou *et al.* [28] and Fixe *et al.* [29] showed that photoresistor or photoconductor based systems may be feasible. They demonstrated through their experiments that fluorescence can be detected by these sensors, thus providing another option in terms of possible detectors for LOC devices.

Not all LOC devices are designed for a liquid sample or a fluorescent dye. Since the main objective is to develop a fluorescence detection system, all related systems for any LOC devices is applicable. Takabayashi *et al.* [30] developed a LOC device to measure trace nitrogen dioxide gas in the atmosphere using typical components such as an UV LED for excitation and a PMT for detection. Similar to the device for measuring chlorophyll, another group that built a device to measure intrinsic fluorescence is Estes *et al.* [31]. Like Barócsi *et al.*, their device does not measure fluorescent dyes. Instead, it is designed to directly detect for the presence of microbial contamination via intrinsic fluorescence of nucleic acids. For example, by providing UV excitation at 340 to 360 nm, some biological materials will fluoresce at 425 to 500 nm [31]. From their work, it appears that any system capable of providing and detecting those ranges of wavelengths can also function as a microbial contamination measurement system. For their instrument, they used a xenon lamp, PMT to maximize signal detection, and a microcontroller for processing and debugging [31]. Although their device works well, being capable of detecting approximately 20 cells/cm^2 in seconds [31], there was no mention of the power requirement and using components such as PMTs and lamps can easily increase the cost of their device. However, their wireless feature is attractive for remote sensing on the field. More details related to their research can also be found in [32]. To help reduce the cost of an optical detection system, a couple of simple and cost-effective implementations are proposed by Novak *et al.* [1] and Chediak *et al.* [33, 34]. Just this year Novak's group developed an inexpensive miniature fluorescence detection system with a limit of detection for fluorescein of approximately 1.96 nM [1]. A neat feature with their device is that by using a lock-in amplifier tuned to a specific frequency, the device is able to measure fluorescence while under ambient light. Filtering for a specific frequency will also improve the signal to noise ratio as noise

from other frequencies are removed. A few years prior, Chediak's group used a technique known as laser lift-off to combine a separately grown blue LED with a pre-made PIN photodiode, thereby significantly minimizing the footprint of the device. In addition, they also implemented a CdS filter to block the excitation light, allowing for a minimum detectable concentration of approximately 1.2×10^{-7} M [34]. Since most of their major components are based on semiconductors, it is conceivably easy to mass produce their device, which will significantly reduce the cost of the detector system. However, the main drawback with their design is that it requires the use of an external readout system, thus it is not totally self-sufficient.

Another related research on an integrated filter and a PINN$^+$ photodiode is performed by Namasivayam *et al.* [35]. Their on-chip fluorescence system is capable of detecting 0.9 mg/L of DNA even when using a blue LED as the source [35]. At around the same time Nivens *et al.* [36] wrote a paper on bioluminescent bioreporter integrated circuits for LOC applications. They took a different approach in that they do not require the use of any excitation light at all since their application is for bioluminescence instead of fluorescence. For bioluminescence, the emitted light to be detected is produced by biochemical reactions [36]. This has a few advantages, including lower power requirement and minimal noise signal, as no light source is used. There is no added burden to the power system nor do precautions have to be made to filter out the excitation light. A detection limit of 50 μg/L was achieved after 45 minutes of exposure to the analyte using photodiode based circuits [36]. So although their device is not directly related to a fluorescence detection system for LOC devices, lessons can be learned from their concept to help create better systems. As well, since similar detection components are used, if a fluorescence detection system is capable of performing bioluminescence, then the capability of the LOC device may be increased. It should also be noted that from [35] and [36],

it can be seen that proper detector design should be further investigated if possible. In a related study, Schaefer *et al.* [37] tested an integrated chip with an amorphous silicon photodiode for optical detection. The result of their investigation is that their device was capable of detecting 260 fmol of anthracenyl-oxazoline, which is supposedly comparable to results by Fixe *et al.* [37]. Another factor to be considered is the autofluorescence of plastic materials commonly used in microfluidic and LOC devices. In a study by Piruska *et al.* [38], it was determined that longer wavelengths yielded less autofluorescence, and PDMS had the lowest autofluorescence when compared to other materials such as PMMA, cyclic olefin copolymer (COC), and polycarbonate (PC). This study is important since in order to achieve extremely low detection limits, it is important to reduce ambient noise. Having the device itself fluoresce will undoubtedly increase the noise level, which will reduce the overall signal to noise ratio and raise the minimum detection limit.

2.3 MEMS Diffraction Gratings

Several MEMS based diffraction gratings and diffraction based devices proposed by other groups are introduced in this section. Although the main goal for this thesis is wavelength tuning, not all gratings presented are for that application; however, they can all be applied for such a purpose. The results being presented in this section are grouped into reflection grating or transmission grating for organization.

2.3.1 Reflection Gratings

Reflection gratings are commonly used due to their simplicity. They can be fabricated by simply patterning the substrate using binary masks to create the required

grooves. They may not necessarily have reflective surfaces, such as metal deposited on the surface. In order for them to be tunable for specific wavelengths, a method is required to change the spacing between the grooves. This relationship is discussed in a later chapter in equation 4.4. This can be accomplished if the substrate is of a deformable material, as demonstrated by Wong *et al.* [39]. Using materials such as Pt/Ti and piezoelectric actuators to transversely stretch the membrane, it was possible to change the spacing of the grooves. Their device required both surface and bulk micromachining to incorporate the lead zirconate titanate (PZT) piezoelectric actuators with the platinum membrane. Because of the analog piezoelectric actuation, it is capable of finer angular resolution, lower power is required, and fast responses are possible; however, it loses the large tuning range that digitally actuated gratings can offer [39]. In addition to piezoelectric actuators, it is also possible to actuate a MEMS grating device by using comb drives. This is demonstrated by Shih *et al.* [40] with their silicon on insulator (SOI) device. Similar to the design described by [39], it also trades deflection range for angular resolution due to the limited lateral movement. According to the authors, it is capable of an angular tuning range of approximately 600 μrad or a change in grating period of 150 nm at only 31 V [40]. Their device was fabricated using deep reactive ion etching (DRIE) to form deep vertical beams and springs, and the beams are deposited with a reflective material for increased reflectance power. Their device is to be used to help counter the effects of blurring when using limited numerical apertures (NA). Since the grid spacings are not fixed, the grid period can be slowly changed while sampling until they have a series of data that they can use to extrapolate the desired information. This technique would not be possible in a system where the grid periods are set. In such a system, a large aperture is needed for each wavelength to strike only their corresponding pixel on the detector [40]. However, using large apertures to prevent

wavelengths from overlapping is not always possible. Thus this idea can be used for LOC fluorescence devices also since the same problem may also be solved by the use of a diffraction grating. Another form of actuation to change the grating period is via thermal actuation. Zhang *et al.* [41] introduced a MEMS pitch tunable grating that is actuated by rhomboid "heatuators." The "heatuators" are current driven, where upon heating due to current flow, the flexures will stretch and force the structure to deform from a grating period of 13 μm to 18 μm [41]. Using equation 4.4, it can be seen that this grating is capable of tuning across a relatively wide range of wavelengths in the IR spectrum. Their device is designed to be used with a focusing lens for wavelength division multiplexing. The changes in the grating period will result in wavelengths shifting from one set of optical fibres to the next set. However, the same grating can be applied to the application of wavelength tuning.

Some groups have even developed tunable blazed gratings [42, 43]. Burns *et al.* fabricated several variable blaze gratings using the multi-user MEMS process (MUMPs). They investigated peak-to-valley curvature with respect to various thicknesses, such as by using only one polysilicon layer, stacking polysilicon layers 1 and 2, or using both layers and an intermediate oxide layer [42]. They showed that as thickness increased, the curvature of the slat decreased. These curvatures are typically the result of residual stresses created due to the different stresses across different materials. In the case of MUMPs, the stress difference between the gold and polysilicon layer can cause the curvature. The flatness of the gratings is important and should be taken into consideration as it is essentially the reflecting surface and unwanted curvatures should be avoided to reduce any chromatic errors. They have also demonstrated that it is possible to control the blaze angle via electrostatic as well as thermal actuation, suggesting future work in either area is possible. Li *et*

al. [43] also fabricated tunable blazed gratings by using a combination of KOH etching, DRIE and the SOI fabrication process. Their design differs in that each of their blazed gratings can be actuated individually along the transverse direction while the overall substrate is at an angle [43]. By orienting them directly against the normal of the incident light, the transverse movement along the substrate will result in a path length change for the beams according to basic trigonometry. This difference in path length will effectively result in a phase delay and create either constructive or destructive interference. By changing the separation between different blazed elements, the phase difference can be modified so that only specific wavelengths will benefit by constructive interference. As a result, it can operate as a tunable spectral filter [43].

One can also adjust the incident angle with respect to the diffraction grating in order to change the other parameters in equation 4.4. This was accomplished by a scanning device fabricated by Kiang *et al.* [44] using the MUMPs process. It possesses a fixed grating period of 4 μm, and is to be operated in the first diffraction order [44]. The grating is mounted vertically on torsion bars at an angle and actuated electrostatically by comb-drives. Electrostatic forces will pull on the comb-drives to change the tilting angle of the grating plate. Using a set of optical fibres, collimating lens, focusing lens and an optical power meter, the authors demonstrated that multiple diffraction orders could be detected with the grating plate [44]. Unfortunately, each increasing order resulted in decreased efficiency. Therefore, if only low order diffractions are used, then it can operate as a scanner capable of colour identification.

Research on diffraction gratings capable of planar rotation by using mechanisms developed for MEMS micromotors was also performed [45]. The result was a planar

diffraction grating scanner that was capable of out of plane scanning due to the many out of plane diffraction orders. Because of their relatively large reflective surface, chemical mechanical polishing (CMP) during fabrication is critical for their device to reduce abnormalities. The authors illustrated the significance of CMP by comparing between polished and unpolished polysilicon, as well as single-crystal silicon. In addition, the rotor has to be of sufficient thickness after polishing to counter any residual strain in the polysilicon to minimize any curving [45]. Although wavelength tuning was not specifically proposed as an application by the authors, it is still possible to tune for specific wavelengths if the position of the input beam as well as the detector is constant. Rotating by a few degrees will effectively change the incident angle, and hence, the wavelength. This type of design is well suited for cases where lateral and out of plane movement is prohibited due to space limitations.

Another popular design is to change the path length of the incident beam by manipulating the height of each individual reflector. Although it does not directly modify equation 4.4, it does still produce diffraction if the electrodes are activated such that the beam heights are alternating between high and low. The result is a modulation of light to produce either a bright or a dark state. A popular example is the Grated Light Valve (GLV) developed by Silicon Light Machines. It possesses an array of beams or ribbons where alternating ribbons can be lowered to produce a diffraction grating. If the ribbons are not actuated, then it will effectively act as a planar mirror and causes the light to be directly reflected back along the normal angle. This will result in the dark state. If the ribbons are actuated and an alternating height is produced, then light will be diffracted at an angle and can be collected to produce a light state. Gray scale production is also possible if the ribbons can be switched fast enough [46]. Although this does not directly tune the wavelength of interest, variations of this type of grating can. If this design

was mounted on a scanning mirror type of support, wavelengths can be tuned by simply changing the tilt angle and it would be capable of modulating the intensity of that specific wavelength by activating the ribbons. Another possible design is to use an array of thinner beams and actuating a set sequence of beams to change the effective grating width and period. The polychromator developed by Hocker *et al.* [47] is also an array of reflective mirror beams like the GLV, but differs in that the height separation between the individual beams in their polychromator is adjustable. By using various voltages, the depth of each pit can be adjusted [47]. This means that this grating can be designed for various wavelengths by using a phase delay method since different heights will correspond to different phase shifts, and consequently, wavelengths. The result is that one can tune across a range of wavelengths by simply changing the depth of the pits. Hocker *et al.* used their polychromator to synthesize a polychromatic spectrum for applications such as remote detection. Because each beam can be actuated independently of each other, the changes in height between adjacent beams can vary across the array. The resulting grating profile will selectively reflect multiple wavelengths while ignoring others and can change when a different polychromatic spectrum is required. The advantage of this system is that it can replace reference samples that may be needed for chemical detection since it can generate any reference spectrum as long as it is programmable. This could be beneficial for biological devices since it can simulate a reference spectrum to compare fluorescence results with.

One common use of reflection based grating is for spectroscopy. A concave grating is typically used to spread the spectrum onto a planar array of detectors, where each wavelength should ideally only occupy one pixel or optical fibre. The setup is normally placed such that the entrance slit, the gratings, and the detectors or exit slits are sitting on the perimeter of a circle. This circle is usually denoted

as the Rowland circle and the radius of curvature of the concave grating is set to be equal to the diameter of the Rowland circle so that all wavelengths will be focused onto the perimeter of the Rowland circle. Thus, if the detector array or exit slits lie on the circle, then the incident beam arriving at the array or exit slits will be focused to minimize any overlaps. The disadvantage of such systems is that a relatively large area is required and the cost of having a large pixel array can be significant.

2.3.2 Transmission Gratings

Transmission grating is the other type of diffraction grating available. The main difference between transmission and reflection grating is that the surface does not have to be covered with reflective material, as optically flat, and there is no pit depth for phase delay. In addition to semiconductor materials presented thus far, other materials can be used for diffraction gratings. For example, a simple diffraction grating nanoimprinted on PDMS and actuated by silicon comb-drives was developed by Tung *et al.* [48]. An advantage of PDMS diffraction gratings is that they may be easier to directly integrate with microfluidic devices since those devices are typically already composed of PDMS. PDMS is also optically transparent and relatively elastic, making them well suited for optical and mechanical applications [48]. The authors reported that applying a voltage of 0 to 50 V yielded a peak wavelength that tuned from 557.7 to 572.3 nm [48]. This demonstrates that PDMS is a material that may possibly be used for diffraction gratings and should be further investigated due to their direct use in microfluidics. Being able to build tunable diffraction gratings directly into a microfluidic channel should result in fewer external optical components, helping to meet the goal of a cost effective device. However, the tuning

range of the gratings will need to be drastically increased.

Another variation of a MEMS diffraction grating device uses the fact that silicon is relatively transparent to wavelengths longer than 1.1 μm [49]. Kong *et al.* developed an IR microspectrometer by patterning aluminum gratings on a silicon wafer and mounting the wafer on top of an array of thermopiles. While using the thickness of the wafer as the optical path length, the stacked wafer has the added advantage of using silicon to filter out any visible light from the thermopile to minimize noise. Using a grating period of 4 to 20 μm, a spectrum from 1 to 9 μm was measured, demonstrating the ability of the device to tune across a range of wavelengths in the IR spectrum [49]. This type of design should be further investigated as it can inherently filter out ambient light to reduce noise levels.

Several groups have also performed research into producing transmission gratings that are integrated with waveguides and detector arrays [50, 51, 52, 53, 54]. The advantage of such systems is the possible reduction in the number of external optical components that are required for proper operation. This can also result in a smaller and less expensive system if all of the parts are pre-integrated. Krawczyk [52] demonstrated how add/drop filters can be integrated into directional couplers. Goldman [53] created an integrated device for chemical analysis using buried diffraction gratings, an ultra-thin planar waveguide and a detector array. The diffraction grating is used to couple light into the waveguide at an angle so that many internal reflections can occur. If numerous reflections at the waveguide-sample interface can be achieved, then the path length of the beam interacting with the chemical under test is effectively increased [53]. Another diffraction grating is used at the exit to spread the spectrum across a detector array in order for each wavelength to be measured. Another possible chemical sensor is to use an inte-

grated spectrometer similar to the one reported by Kwa *et al.* Using silicon bulk micromachining, they implemented a spectrometer with integrated grating and detector array [50]. It is designed to operate in the visible and near-IR range, and with a path length of 4 mm through the cavity of the device, it may be possible to be used to monitor absorbance of gaseous or liquid samples in the cavity. The increased path length due to the cavity also serves to minimize the number of different wavelengths overlapping across a pixel [50]. Although there are no moving parts in both of these devices, one can tune or select a specific wavelength by simply measuring across the corresponding photodetector. Chaganti *et al.* [54] also developed a miniature spectrometer composed of a planar waveguide grating coupler, as well as an additional external plano-convex lens. The lens is focused onto a CCD whose position can be adjusted such that the spectrum of interest is spread across the detector array. An advantage of using planar waveguide grating coupling is that one can integrate planar waveguides with microfluidic applications, and thus, it is possible to integrate miniature spectrometer systems of similar design with lab-on-a-chip devices [54].

Chapter 3

Fluorescence Detection System Design

Since optical detection methods are prevalent due to their sensitivity and repeatability [1], one of the objectives of this thesis is to design and build a prototype fluorescence detection system. A working prototype has been designed, constructed, and tested. The details of this study will be discussed in this chapter. It shall be shown that it is possible to build a self-sufficient fluorescence detection system while using only cost-effective solutions. This will help achieve the overall goal of LOC devices to be both portable and inexpensive.

3.1 Background Theory

A good understanding of semiconductor physics in addition to the well developed semiconductor fabrication technologies have allowed for the development of high

performance and cost-effective optoelectronics. These components are essential to produce an inexpensive and portable LOC device. Additionally, since the materials used for fabrication are semiconductors, it may be relatively simple to integrate several solid state electronic components such as transistors and amplifiers along with the optoelectronics. By combining these components during manufacturing, and using the mass production capability of semiconductor devices, it should be relatively easier to produce cost-effective optical devices. Minimizing any handling during post-production will also help increase the overall yield, further reducing the cost of fabrication.

In order to help keep the cost of the device down, the excitation of fluorescent dyes is achieved by a semiconductor-based optoelectronic solution: LEDs. For the application of fluorescence detection for LOC devices, two main candidates that use similar technologies are being considered in this thesis: (i) photoresistor and (ii) photodiode. Both are relatively inexpensive, so if they can perform suitably well in terms of low light detection, then they are ideal for fluorescence detection systems for LOC devices. The background of these components will be briefly reviewed in the following sections, as well as a discussion on an observable effect known as the inner-filter effect.

3.1.1 Excitation Source

The basic operation and design of an LED will be described in this section. Although this information can be found in many semiconductor optoelectronic books, such as Ungar's "Fibre Optics: Theory and Applications" [55] or Kasap's "Principles of Electronic Materials and Devices" [56], a short description is summarized here to facilitate the reader if necessary.

A typical light emitting diodes' light production is based on the principle of light emission in a semiconductor. In a normal semiconductor, there are usually two energy bands, the conduction band (Ec) and the valence band (Ev). The difference between these bands is called the bandgap or the forbidden band (Eg):

$$Ec - Ev = Eg \tag{3.1}$$

which can also be rewritten as:

$$Ec - Ev = hf \tag{3.2}$$

where h is Planck's constant of $h = 6.626 \times 10^{-34}$ J/s or $h = 4.136 \times 10^{-15}$ eV·s and f is the frequency of the photon. However, since the frequency is inversely proportional to the wavelength of the photon according to the equation $c = f\lambda$, then combining equations 3.1 and 3.2 will yield the well known equation:

$$\lambda = \frac{hc}{Eg} \tag{3.3}$$

where λ is the peak emitted wavelength and c is the speed of light of $c = 3.0 \times 10^8$ m/s. Essentially, these equations state that electrons with energies greater than the bandgap energy have a chance of traversing across the bandgap from the lower valence band to the conduction band. Conversely, electrons in the conduction band may fall to the valence band by releasing energy either non-radiatively or radiatively. This is the basis of how light is emitted from semiconductors; that is, when the energy is released radiatively in the form of photons. To encourage the transition of electrons from the conduction band to the valence band for light production, the material can be doped to provide additional holes in the valence band. Applying

an external bias will help to ensure this process will continue, thus allowing for a constant production of photons.

As the name light emitting diode suggests, LEDs are fundamentally diodes. Diodes are formed by doping the semiconductor with n and p regions next to each other to form a p-n junction. The result is that a space charge region will be formed at the boundary, creating a potential energy barrier that opposes the flow of electrons from the n-type semiconductor to the p-type semiconductor. The barrier created is due to the internal electric field generated across the p-n junction as a result of the positive and negative ions in the n-side and p-side of the depletion layer respectively. These ions are created when electrons from the n-side combine with holes in the p-side, forming a depletion region that repels the diffusion of carriers across it. The potential energy barrier, which has a value of eVo and where Vo is the built-in voltage, is shown in the band diagram in figure 3.1. Consequently, a

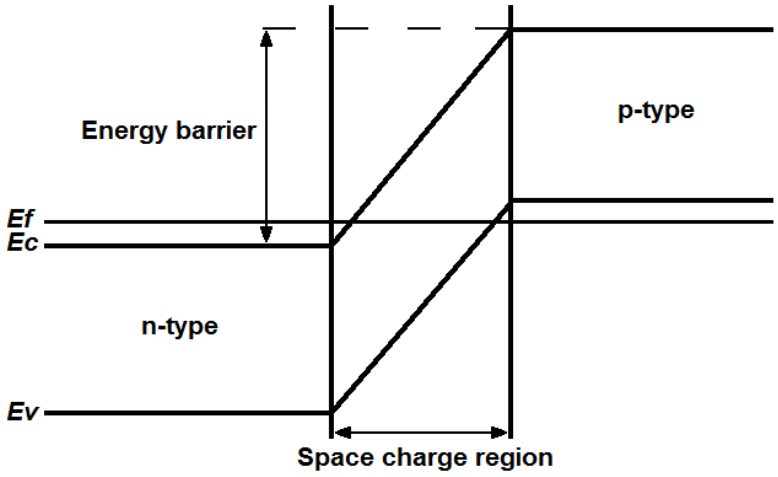

Figure 3.1: Energy diagram of p-n junction without biasing. The Fermi energy levels (Ef) are equal during equilibrium without any bias.

forward bias must be applied so that some electrons will have sufficient energy to

surpass the energy barrier and allow current to continue to flow. Once high energy electrons in the conduction band enter the p-side, they will tend to fall back to the valence band as previously described to fill the holes to form a more stable state. These are also illustrated in figure 3.2, where forward biasing reduced the potential energy barrier, allowing electrons to flow across. Also illustrated are the electrons in the p-side falling to the valence band and recombining with holes to release photons. From equation 3.3, it can be determined that by choosing or designing the proper

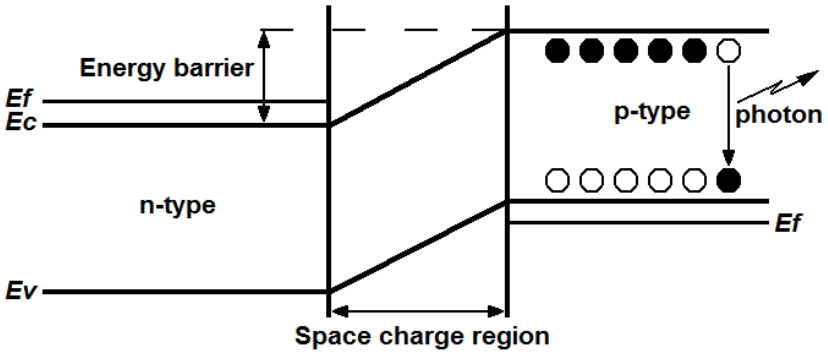

Figure 3.2: Energy diagram of p-n junction with forward biasing. The energy barrier has been reduced by the applied bias to the amount of $Vo - V$, allowing the electrons to diffuse across.

semiconductor material, which will effectively determine the bandgap, it is possible to control the emitted colour of the LED. For example, some of the possible semiconductor materials for LEDs include GaAs for red to infrared wavelengths [55,56], GaP for green [55, 56], InGaN for 450 to 574 nm excitation [2, 6, 26], and AlGaInP for 650 to 690 nm wavelengths [6, 57]. More examples and specific wavelengths are given in Ungar's and Kasap's textbooks [55,56] for readers interested in further pursuing this topic. It should be noted at this point that the wavelength in equation 3.3 is not necessarily the only wavelength being emitted. There are several reasons for this. The first reason is that electrons in the conduction band and holes in the

valence band may have slightly different energies. The second reason is that there may be multiple energy levels between the bandgap, such as due to impurities. The additional energy levels can act as transitional levels, allowing for electrons having energies different than the bandgap to still traverse across and release photons. Consequently, purposely implanting impurities to create indirect bandgap semiconductors can result in the emission of photons of different wavelengths. The drawback is that indirect bandgap semiconductor LEDs are typically less efficient than direct bandgap LEDs due to the dependency on impurity concentration [56].

Since semiconductors can also reabsorb the photons, which will be discussed later in a section for detectors, it is beneficial to minimize the amount of photons reabsorbed by the LED to maximize the net light output. By creating a junction between two semiconductors with different bandgaps, it is possible to reduce the absorption of photons and increase the output efficiency. This type of junction is typically denoted as a heterojunction. By using mismatching bandgaps, it is possible to confine the electrons to a desired region. In addition, if the bandgap of the material is larger than the energy of the photons, then the photons will not be reabsorbed and can be reflected back out through the material to increase the overall external efficiency. This is illustrated in figure 3.3, showing the energy diagram of a sample heterojunction formed by using materials with different bandgaps. From the figure, since the bandgaps of the first and third materials are larger than the bandgap of the second layer, meaning that bandgaps *Eg1* and *Eg3* are larger than the energy of the emitted photons (*Eg2*), no photons are absorbed in the first and third layers. The energy difference between the conduction bands of materials two and three also forms an energy barrier that effectively limits the active light production region to only within the second material. Additionally, adding a reflective surface behind the third material can allow for the reflection of

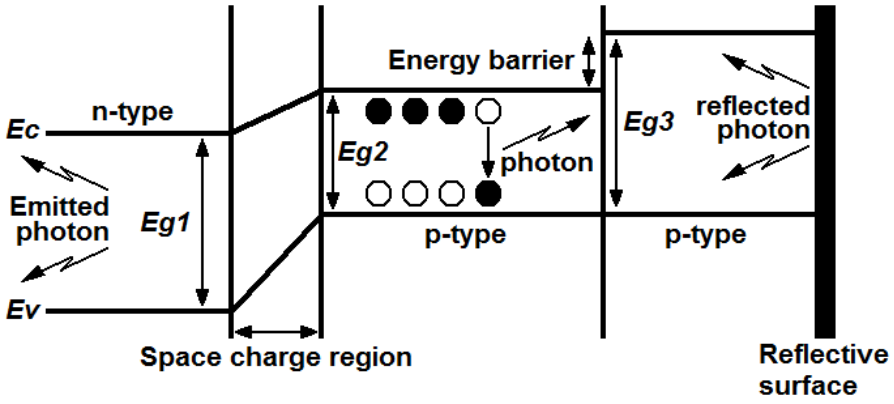

Figure 3.3: Energy diagram of a heterojunction LED under forward biasing.

photons back out through the first two layers to increase the overall efficiency of the LED.

Much has been mentioned about LED efficiency. During the course of transit from photon generation to being emitted from the LED, there are several instances where the overall efficiency can be affected. Starting from the photon generation itself, as was just mentioned, using indirect bandgap semiconductors usually results in a lower efficiency. This is due to the fact that there is now a dependence on the impurity doping and no longer relying purely on the bandgap [56]. To help improve the net output efficiency, heterojunctions can be implemented to help direct the emission of photons through a specific output solid angle. As mentioned before, the semiconductor may reabsorb some of the photons. Intuitively, it suggests that the longer the photons have to travel in the material, the greater the chance they will be reabsorbed. Thus the relationship is of an exponential one with respect to distance [55]:

$$\rho_{Absorption} = e^{-\alpha x} \tag{3.4}$$

where $\rho_{Absorption}$ is the absorption efficiency, α is the absorption constant, and x is the distance the photons have to travel. So to minimize any absorption loss, attempts are made to decrease the distance the photons have to travel, such as the depth of active region, as well as to use materials with relatively low absorption constants. Once the photon exits the semiconductor, two other types of losses may occur. Both losses are due to the behaviour of light when traveling from one medium to another with different indices of refraction. The first loss is known as Fresnel loss, which occurs because of the mismatched index of refraction. The result is that there will be some reflection of photons back into the semiconductor as shown in figure 3.4. The effect of this on waves is determined by Fresnel's equations, and

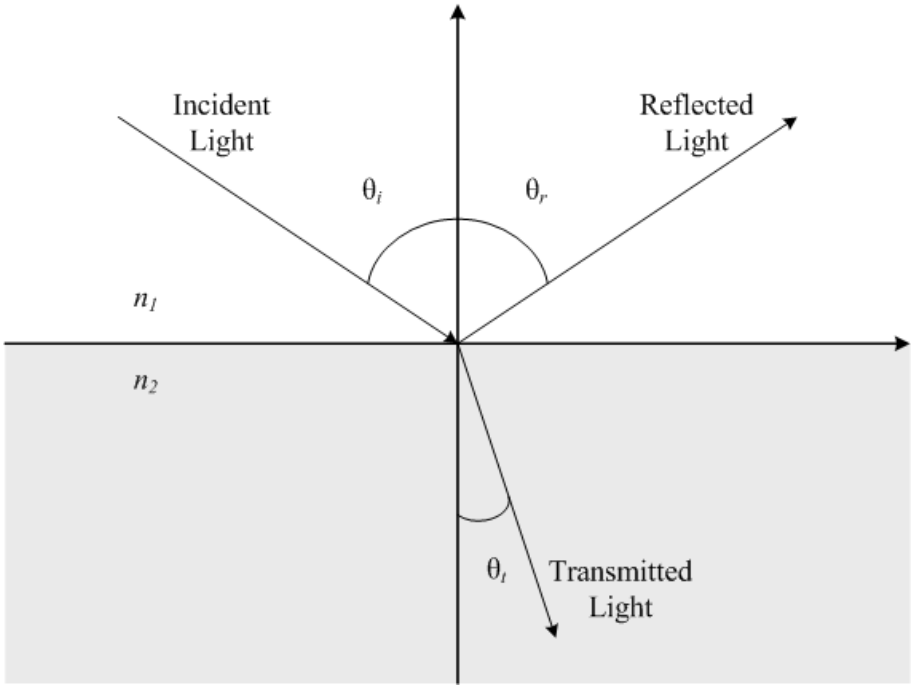

Figure 3.4: Diagram showing reflection and transmission at the boundary of two materials with mismatching indices of refraction.

light is susceptible as it exhibits properties of both particles and waves. Since light

is essentially an electromagnetic wave, the general case for Fresnel's equations of an EM wave traveling between two materials of different indices of refraction will be considered. The reflection coefficient is determined by [58]:

$$R_s = \left[\frac{n_1 \cos\theta_i - n_2 \cos\theta_t}{n_1 \cos\theta_i + n_2 \cos\theta_t}\right]^2 \tag{3.5}$$

for s-polarised light or for p-polarised light:

$$R_p = \left[\frac{n_1 \cos\theta_t - n_2 \cos\theta_i}{n_1 \cos\theta_t + n_2 \cos\theta_i}\right]^2 \tag{3.6}$$

where n_1 and n_2 are the refractive indices of the two materials and θ_i and θ_t are the incident and refracted angles respectively. Through trigonometric identities and Snell's law, equations 3.5 and 3.6 can be rewritten as:

$$R_s = \left[\frac{\cos\theta_i - \sqrt{n^2 - \sin^2\theta_i}}{\cos\theta_i + \sqrt{n^2 - \sin^2\theta_i}}\right]^2 \tag{3.7}$$

$$R_p = \left[\frac{\sqrt{n^2 - \sin^2\theta_i} - n^2\cos\theta_i}{\sqrt{n^2 - \sin^2\theta_i} + n^2\cos\theta_i}\right]^2 \tag{3.8}$$

where $n = n_2/n_1$. In the special case of the incident angle $\theta_i = 0$, these equations will yield:

$$R = \left(\frac{n_1 - n_2}{n_1 + n_2}\right)^2 \tag{3.9}$$

Thus the percentage of photons actually traveling across the interface is the remainder and is given as the transmission coefficient T:

$$T = 1 - R$$

$$T = \frac{4n_1 n_2}{(n_1 + n_2)^2} \tag{3.10}$$

Since the coefficient is with respect to unity, it is essentially the transmission efficiency, $\rho_{Transmission}$. As in an example given by Ungar, it is ideal to insert a material with an index of refraction of somewhere between that of the external medium and the semiconductor to increase the transmission efficiency. Using Ungar's sample values of $n_{semiconductor} = 3.4$ and $n_{plastic} = 1.5$ [55] the following efficiencies are calculated:

$$\begin{aligned}
\rho_{Transmission\ A} &= \tfrac{4n_{semiconductor}n_{air}}{(n_{semiconductor}+n_{air})^2} \\
\rho_{Transmission\ A} &= 0.7025 \\
\rho_{Transmission\ B} &= \tfrac{4n_{semiconductor}n_{plastic}}{\left(n_{semiconductor}+n_{plastic}\right)^2} \cdot \tfrac{4n_{plastic}n_{air}}{\left(n_{plastic}+n_{air}\right)^2} \\
\rho_{Transmission\ B} &= (0.8496) \times (0.96) \\
\rho_{Transmission\ B} &= 0.8157
\end{aligned}$$

Thus the example shows that by simply adding another material with an index of refraction of between those of the two mediums can increase the transmission efficiency by more than 10%. Along the same lines, the well known Snell's law also dictates that transmission from one material to another with different indices of refraction will indirectly yield a critical angle. Thus any photons that strike the interface above this angle will be reflected back into the material. From Snell's law, the efficiency of the critical angle can be obtained [55]:

$$\rho_{Critical\ Angle} = \left(\frac{n_2}{n_1}\right)^2 \tag{3.11}$$

Similar to the previous example, adding an intermediate plastic layer can help increase the efficiency. Using a hemisphere shaped plastic cover instead of a flat

shaped one will also help increase the output. The reason is that the photons that have refracted at an angle while traveling from the semiconductor into the plastic cover will then exit the hemisphere cover at a relatively low angle with respect to the normal of the LED. This minimizes the spreading of the photons when they exit the plastic cover as well as reducing internal reflection. Finally, multiplying all three efficiencies together will then yield the overall efficiency from photon generation to emission from an LED [55]:

$$\rho_{Overall\ Efficiency} = \rho_{Absorption} \cdot \rho_{Transmission} \cdot \rho_{Critical\ Angle} \tag{3.12}$$

Thus maximizing any of the above efficiencies will help improve the overall efficiency. This is important since LEDs are not inherently powerful light sources. However, considering that they are significantly inexpensive, they can prove to be feasible excitation sources if they can provide sufficient power.

3.1.2 Detector

Some of the most commonly used components for sensitive optical detection are photodiodes, PMTs, and photon counters. Photodiodes are the least expensive of these components since they are not designed for extreme low level light measurement that PMTs and photon counters are designed for. Consequently it is being investigated as a photodetector for the application of fluorescence detection. In addition, because photoresistors are evaluated for specific use in LOC devices since they are also inexpensive components, a brief discussion describing them is given in the following section.

3.1.2.1 Photoresistor

A photoresistor is a very basic and inexpensive optical detector. Their resistance is dependent on the intensity of the incident light. The range of resistance values can span from several hundred ohms when exposed to light to several mega-ohms in dark conditions. Like an LED, it uses the bandgap property of the semiconductor to determine the wavelengths that the photoresistor is sensitive to. As a result, it follows equation 3.3, where in this case Eg is the minimum energy of the photon needed to free the bound electrons to the conduction band to form electron-hole pairs. The result of this effect is that the conductivity of the material changes, thus allowing for the conduction of electricity.

A material commonly used for photoresistors is cadmium sulphide (CdS). It has a bandgap of approximately 2.41 eV [59], which corresponds to a peak wavelength of 515 nm according to equation 3.3. Although the peak resides in the green region, the overall spectral response of this material should cover the entire visible band [60,61]. Consequently, it is reasonable that CdS is well-suited for applications that require sensitivity within the visible spectrum. The ability to detect the visible spectrum also suggests that CdS photoresistors can be used in cases where only a simple visual inspection by the naked eye is involved. Examples include the ELISA test, where if there is fluorescence, then the specimen being tested for is present. This binary form of detection is well within the capability of the photoresistor if there is sufficient concentration to stimulate a response in the detector. In addition, it is possible to fabricate small photoresistors due to their semiconductor nature. That allows for greater portability and flexibility in device design, making them well suited for fluorescence-based LOCs. However, a disadvantage with CdS photoresistors is that they do not demonstrate a linear response with respect to the intensity of the

incident light [61]. This can be rectified by using a microcontroller with tables of values if the photoresistor can behave in a consistent manner. If the overall response of the photoresistor is known for the required wavelengths and intensities, then the linearity problem can be solved by storing multiple tables with values for each of the corresponding intensities and wavelengths.

3.1.2.2 Photodiode

Another popular light sensitive device similar to the photoresistor is the photodiode. It is also relatively inexpensive and operates by generating photocurrent when in the presence of light. The total output current is mainly composed of the sum of three distinct currents. The three main currents are the photocurrent generated as a result of photons creating electron-hole pairs from equation 3.3, the saturation current as given by the Shockley equation, and the generation-recombination current [62]. The generated photocurrent density can be determined by:

$$J_\phi = q \int_0^{\lambda_c} \eta(\lambda) F(\lambda) d\lambda = q\eta F \quad \frac{\text{A}}{\text{cm}^2} \tag{3.13}$$

where q is the electron charge of 1.6×10^{-19} C, η is the quantum efficiency averaged over the spectral band of the integral, and F is the photon flux density averaged over the same integral as given by [62]. Equation 3.13 essentially states that the photocurrent generated is dependent on the flux of the incident light as well as the efficiency of the material at producing electron-hole pairs across the spectral band at a given light intensity. Because the photodiode has the structure of a diode, so it consists of at least a p-n junction, there exists an internal diffusion flow. This is determined by the saturation current density and the equation is given as

follows [62]:

$$J_{diff} = q\left[\frac{D_p p_n}{L_p} + \frac{D_n n_p}{L_n}\right]\left[\exp\left(\frac{qV}{kT}\right) - 1\right] \quad \frac{\text{A}}{\text{cm}^2} \tag{3.14}$$

where D_p is the hole diffusion coefficient, D_n is the electron diffusion coefficient, L_p is the hole diffusion length, L_n is the electron diffusion length, p_n is the hole concentration in n-type region, n_p is the electron concentration in p-type region, V is the applied bias across the junction, k is Boltzmann's constant of 1.381×10^{-23} J/K and T is the operating temperature in Kelvin. The diffusion coefficients and lengths found in equation 3.14 above can be calculated by the well known semiconductor equations shown in 3.15 and 3.16 respectively:

$$D_p = \frac{kT\mu_p}{q} \quad \text{and} \quad D_n = \frac{kT\mu_n}{q} \tag{3.15}$$

$$L_p = \sqrt{D_p \tau_p} \quad \text{and} \quad L_n = \sqrt{D_n \tau_n} \tag{3.16}$$

where μ_p and μ_n are hole and electron mobilities while τ_p and τ_n are the respective carrier lifetimes. Equation 3.14 determines the current generated as a result of the applied bias, the drift due to the internal electric field across the p-n junction, the diffusion based on the doping, material properties, as well as the operating temperature. However, not all generated electron-hole pairs produced by the incident photons will remain separated. Some of the generated carriers may recombine during transit, reducing the overall photodiode current. This is undesirable as that essentially means the signal is decreased since the photodiode gives the measurement in terms of output current. Therefore, the amount of charges recombined or lost need to be calculated and can be determined by the generation-recombination

current density [62]:

$$J_{G-R} = \left[\frac{n_i W}{\tau_o} \frac{\sinh\left(\frac{qV}{2kT}\right) kT}{V_{Bi} - V} \right] \quad \frac{\text{A}}{\text{cm}^2} \tag{3.17}$$

where n_i is the intrinsic carrier concentration, W is the depletion layer width, τ_o is the effective carrier lifetime in the depletion region, and V_{Bi} is the junction built-in potential or contact potential. The depletion layer width can be calculated by

$$W = \sqrt{\frac{2\varepsilon}{q} \left(\frac{N_a + N_d}{N_a N_d} \right) \left(V_{Bi} - \frac{2kT}{q} \right)} \quad \text{cm} \tag{3.18}$$

where $\varepsilon = \varepsilon_o \varepsilon_r$ is the permittivity of the semiconductor, N_a is the acceptor concentration and N_d is the donor concentration. The built-in potential of V_{Bi} used for calculating depletion layer width and the generation-recombination current density can be calculated by using the following equation:

$$V_{Bi} = \frac{kT}{q} \ln \left(\frac{N_a N_d}{n_i^2} \right) \quad \text{V} \tag{3.19}$$

Summing the three current densities, $J_\phi, J_{diff}, \text{and } J_{G-R}$, should approximate the generated photocurrent. When operating without an external bias, the photodiode is in the photovoltaic mode and J_ϕ becomes the dominant current density. However, if an external voltage is applied, then the photodiode is operating in photoconductive mode and all three currents should be considered. In photovoltaic mode, the response range is usually smaller than when operated in photoconductive mode. The drawback is that applying a bias increases the noise current generated, which can reduce the overall signal-to-noise ratio.

A variant of the photodiode is the APD. It operates similarly to a photodiode

in photoconductive mode, but differs by providing significant internal gain when applying a reverse bias. This allows the APD to be highly sensitive when compared to typical PIN photodiodes. Consequently, APDs are excellent candidates for low light measurements. Since LOCs should ideally require only a small sample for measuring, APDs are well suited for detecting the minute fluorescence emitted from the limited samples. The applied bias is usually relatively large, such that a high electric field can be generated in the APD to energize the carriers. With greater amounts of energy, the carriers can ionize atoms in the semiconductor to create additional electron-hole pairs. The newly created pairs are then energized in the same way by the electric field and the process is repeated, resulting in an avalanche effect. This typically occurs in a specially designed region of the APD [63]. Depending on the material used, the rate of ionization can differ for electrons and holes, and are denoted by α and β respectively. The ratio of the two, $k = \beta/\alpha$, should ideally be much smaller than unity to improve the gain-bandwidth product and multiplication noise [64,65]. It should also be noted that for high gain $M, k = k_{eff}$ as determined by the equations derived by [66]. Since silicon has a ratio of approximately $k = 0.05$, it is a good material to use in APDs for wavelengths smaller than 1.06 μm [64].

3.1.2.3 Photomultiplier Tube (PMT) and Photon Counters

As previously mentioned, PMTs and photon counters are some of the commonly used components for ultra low level light detection. They will be briefly described here since some optical bioanalysers use these components, such as those discussed in section 2.2. These components are also introduced to the readers should they become interested in learning more about these devices. However, details will be

kept to a minimum since these components are not ideal for LOC devices. The reason is that these devices are costly and require a considerable amount of power to achieve their high sensitivity.

PMTs are similar to APDs in the fact that the photo-generated electrons are further multiplied to increase the overall output signal. Part of an excellent handbook on PMTs by Hamamatsu [67] is summarized here to describe their basic operation. Most PMTs are essentially vacuum tubes containing the following parts: a transparent window through which the light of interest enters, a photocathode that generates electrons per incident photon, electrodes to focus and accelerate the photo-generated electrons, a series of dynodes to multiply the number of electrons, and an anode to collect the electrons. Applying a high electric field to the metal electrodes has the effect of accelerating electrons towards the dynodes with sufficient energy to release additional electrons from the surface by secondary emissions. This has an avalanche effect analogous to that in an APD. Another method of multiplying electrons is to use microchannel plates (MCP) instead of dynodes. For these PMTs, commonly referred to as MCP-PMTs, an array of channels is constructed in such a way that electrons bouncing inside the channels will create additional electrons via secondary emissions. These devices and their physics are described in much greater detail in [67].

For even greater sensitivity, photon counters can be used. These devices measure the intensity in terms of number of photon counts per second. They typically use either PMTs with a discriminating logic circuit [68] or APDs operating in Geiger mode. When operating APDs in Geiger mode, the APD is briefly biased above its breakdown voltage to achieve significantly higher gain with minimal risk to the component. The result is that each incident photons will produce a large current

pulse that can be counted before being quenched and reset for the next count [69]. However, since all of these components require relatively sophisticated circuitry and greater power, they are not investigated for use in LOC devices.

3.1.3 Inner-Filter Effect

One concept that must be introduced to the readers since it will be demonstrated later in the thesis is an effect called the inner-filter effect. It is a phenomenon that can occur when the concentration of a fluorescent sample reaches a certain threshold. At sufficient fluorophore concentrations, the fluorescent solution will noticeably reabsorb some of the emitted light [13, 70, 71]. This occurs because most fluorophores typically have overlapping absorption and emission spectrums, meaning some wavelengths emitted by the fluorophores will be reabsorbed. A sample plot of the absorbance and emission spectra of fluorescein is shown in figure 3.5. It can also be seen that parts of the absorption and emission spectra overlap, as is usually the case for fluorescent dyes. The result of this internal quenching is that the overall fluorescence emission is reduced. For example, one research group has estimated that the relationship between the fluorescence intensity and dye concentration stops being linear when the fluorescein dye concentration is greater than 20 mg/L [13]. After that point, the light intensity should increase at a slower rate. The inner-filter effect can also occur if the overall photon density is not uniform or the shape of the container is designed in such a way that not all fluorophores are uniformly excited [71]. In this case, various regions of the sample may experience different amounts of excitation. This is known as primary inner-filtering, as shown in figure 3.6. In the simplest case of a square container, fluorophores that are furthest away from the excitation source have the lowest probability of being excited

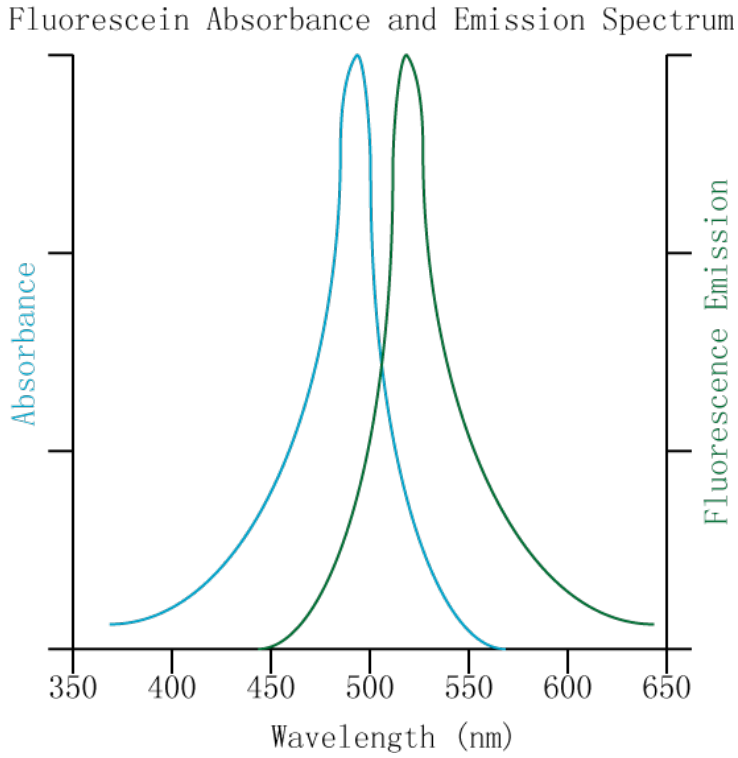

Figure 3.5: Typical absorbance and emission spectra for fluorescein dye.

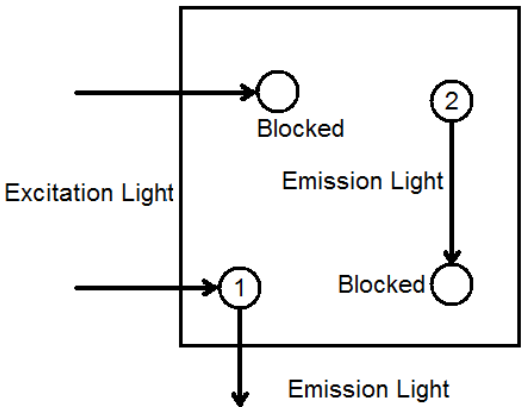

Figure 3.6: Diagram of primary and secondary inner-filtering as described by MacDonald *et al.*

by an incident photon. This is due to the fact that there is a chance photons will be absorbed by other fluorophores along the way, as shown in figure 3.6. In the illustration fluorophore #1 was able to be excited whereas fluorophore #2 was not. Likewise, emissions from fluorophores that are located far away from the detector have a greater chance of being reabsorbed by other fluorophores along the path than emissions from fluorophores located closer to the detector. In this case, if fluorophore #2 is able to be excited to emit a photon, there is a chance it will be absorbed as illustrated in the figure. This reabsorption of the emission is known as secondary inner-filter [71]. Taking the entire inner-filter into account, the overall fluorescence can be approximated by:

$$F = k\phi I_o \alpha_f(\lambda_{ex}) \int_{x_1}^{x_1+\Delta x} \exp\left[-\alpha_{ex}(\lambda_{ex})x\right]dx \cdot \int_{y_1}^{y_1+\Delta y} \exp\left[-\alpha_{em}(\lambda_{em})y\right]dy \qquad (3.20)$$

where k is the proportionality constant, ϕ is the quantum yield per incident photon, I_o is the intensity of the excitation light, $\alpha_f(\lambda_{ex})$ is the absorption of the fluorophore at a given excitation wavelength λ_{ex}, $\alpha_{ex}(\lambda_{ex})$ is the absorption of all materials in the solution along the excitation path at λ_{ex}, $\alpha_{em}(\lambda_{em})$ is the absorption of all materials in the solution along the exit path at a given emission wavelength λ_{em}, Δx is the width of the excitation light beam, and Δy is the width of the emission light beam [13,71]. It should be noted that equation 3.20 is in exponential form, so the absorbencies, α, that are given in base 10 will need to be converted by multiplying by $ln(10)$ or 2.303. The equation basically describes that as the distance from the origin, x_1 and y_1, increases relatively to the excitation source and the detector respectively, the fluorophores at those locations will contribute less to the overall fluorescent intensity. This is determined by the integrals of the equation, x for the excitation path and y for the emission path. The integrals are

related to the Beer-Lambert law since the law determines the absorption of photons based on the property of the medium that the light is traveling through. Thus the absorbencies in the integrals, α_{ex} and α_{em}, must include all materials in the solution in addition to the fluorophores, such as impurities, since they may also absorb some of the excitation and emission photons. This equation also suggests that fluorescent solutions with high absorbencies for both excitation and emission wavelengths will yield lower overall fluorescent intensities than solutions with high absorbencies for excitation wavelengths and low absorbencies for emission wavelengths. This is intuitive as it makes sense that any absorption of the emission photons will result in a decrease in the signal. Thus the ideal case would be $\alpha_{em} = 0$ so that the exponent would be maximized at unity. In addition, as determined by equation 3.20, it is desirable to minimize the distances between the fluorophores, the excitation light, and the detector to reduce fluorescent intensity loss.

3.2 System Design

This section discusses the exact components used in the device and provides insight into the design of the device. It is hoped that it will clarify for the readers why certain components are used when compared to other devices developed by other groups.

3.2.1 Fluorescence System

The fluorescence system for the device proposed in this thesis is composed of: (i) multicoloured LED(s) for multiple wavelength excitation; (ii) an APD or photoresistor for fluorescence detection; and (iii) the respective filters for the fluorescent

dyes. LEDs are chosen as the light source instead of laser diodes and high power lamps due to their low power consumption, low cost, and relatively long lifetimes. High power lamps are not viable options since they are typically large, expensive, and have a fairly limited lifetime. Investigation into alternative excitation sources such as LEDs as evidenced by [6] is becoming fairly common. Laser diodes, which are built by microfabrication technologies similar to those used to manufacture LEDs, are possible excitation sources. However, they are usually more expensive and difficult to fabricate than LEDs due to their unique device structure for creating coherent light. LEDs are used because they are readily available off-the-shelf and for their low cost. Their relatively simplistic solid-state structures also lend well to mass fabrication when compared to laser diodes. There are situations where a laser diode is a more suitable choice than LEDs. For example, the following cases would require laser diodes in order to provide extremely limited spectral bandwidth: (i) monochromaticity for excitation is required; or (ii) a good band-pass filter is not available. These criteria are unnecessary for the applications of the proposed device, so the decision to use LEDs is still appropriate. The LED chosen for the device is an integrated three colours in one LED (LE1011) purchased from LED Shoppe. It is a simple off-the-shelf component capable of emitting red (630 nm), green (525 nm), and blue (470 nm) wavelengths with ratings of 5000, 6000, and 5500 mcd respectively. By integrating an LED capable of emitting at multiple wavelengths, it minimizes the overall size required for the device and also leaves space to allow for additional light sources in the future. For example, another identical LED can be used to increase the overall excitation power for all three wavelengths or an UV LED can be added to make the device capable of UV excitation. This type of flexibility has not been seen thus far, where a low cost device is capable of emitting at these wavelengths without any user modifications. Since different dyes may have differ-

ent excitation spectrums, its multiple excitation capability has the added advantage of allowing for the concurrent use of several different fluorescent dyes. Using an Orion PD power meter equipped with a PD300-1W head, it was determined that the LED provided a maximum of 0.525, 1.15, and 1.08 mW of power respectively when biased at 7 V and using a 330 Ω resistor to limit the current. According to the manufacturer, the power meter automatically takes the responsivity curve into consideration when displaying the light power. The specifications and measured results of the LED are summarized in table 3.1 and figure 3.7. The plastic cover

		Red	Green	Blue
Wavelength	(nm)	630	525	470
Forward Voltage	(V)	2.1	3.3	3.3
Brightness Rating	(mcd)	5000	6000	5500
Measured Power	(mW)	0.525	1.15	1.08

Table 3.1: Specifications of the three coloured LED

was retained to minimize beam spread as discussed in section 3.1.1. Although the LED still has a native viewing angle of ±40°, if it is placed sufficiently close to the fluorescent sample, then most of the excitation light can be directly collected by the sample. Components such as objective lens for the collection and collimation of the excitation and fluorescent light were avoided to reduce the overall cost of the device, as well as to minimize any unnecessary absorption loss when operating at such short distances. Adding expensive optical components to the device only serves to hinder the ultimate goal of creating a cost-effective LOC device.

As previously listed in section 2.2, the use of LEDs for excitation is not new. Sakamoto *et al.* used an Agilent 2100 Bioanalyzer that is equipped with an LED for their on-chip flow cytometry research [8]. However, that device is a retail device and a quotation of it was in the tens of thousands of dollars. While the Bioanalyzer

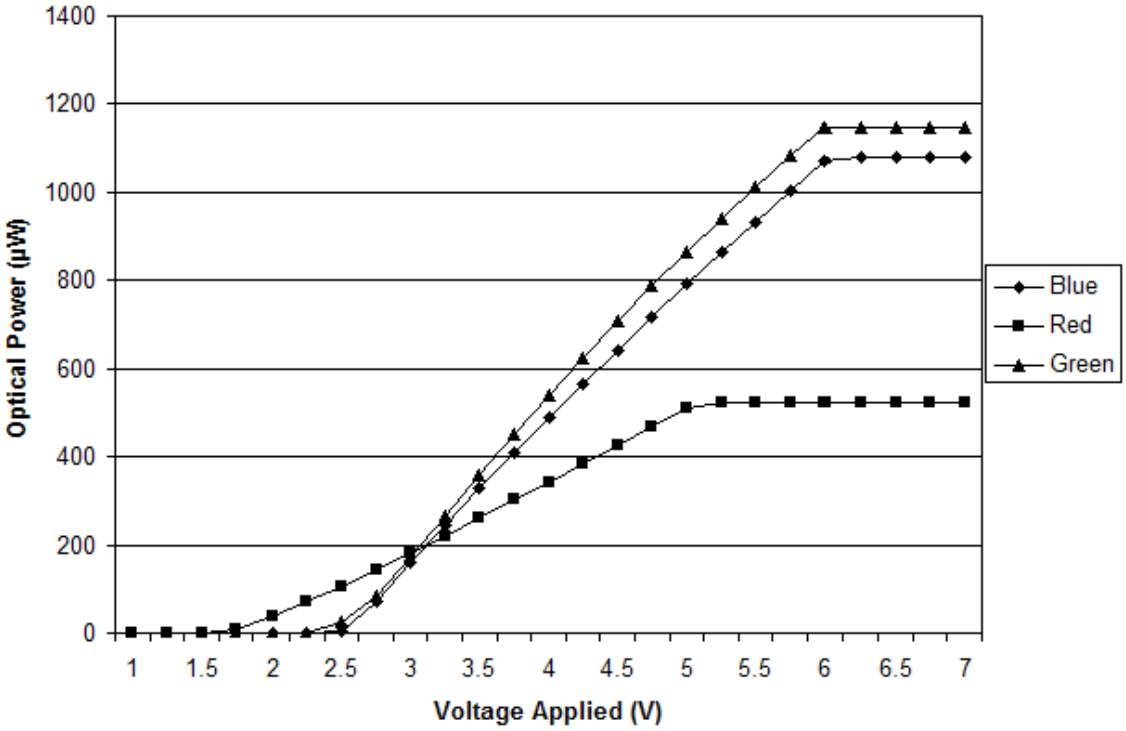

Figure 3.7: Graph of LED output power for each colour with respect to bias voltage. It can be seen that the LED operates in a linear fashion with respect to input voltage power.

is capable of performing many functions, the goal is not to create an identical device. In fact, the Bioanalyzer is not designed to be a handheld device. Since not all functionalities are required by some users, it is desired to design a device that can only be used for certain simple applications. By limiting the functionality of the proposed device, it is much simpler to keep the cost down and reduce the size of the device for improved portability. Also discussed in section 2.2 is the fact that many researchers who have used LEDs usually have also used a combination of microscope optics or special lens and mirrors [1, 7, 13, 30] to focus the excitation and emission light, fibre optics to help the transmission [12, 13, 21], and a PMT for

weak signal detection [7, 12, 20, 30]. The proposed design differs in that optics, such as objective and aspheric lens, for the collection and collimation of light are not used to reduce the overall size and cost of the device. Dichroic mirrors that are designed for specific wavelengths are also not suitable for the proposed device since it should be capable of operating at a multitude of wavelengths. Waveguides such as optical fibres are also unnecessary since the distance between the sample and the detector is extremely short, and waveguides in this case will only absorb the emission signal. Instead of PMTs, a photoresistor or an APD is used to minimize the power consumption and cost. Since the device is to target relatively large fluorescent samples, the high sensitivity of the PMT is sacrificed as they normally require very high voltage for operation and are also fairly expensive. Several groups have used both photodiodes and LEDs in their device [1, 2, 33, 34, 35], but they did not implement a built-in readout system as is provided by the proposed device. Higgins *et al.* developed a device that also uses LEDs for fluorescence and includes a built-in display, but they are limited to excitation wavelengths of 490 and 525 nm due to their specific PCR applications [18]. The device proposed in this thesis is capable of more excitation wavelengths and the modular design allows for future upgrades since the device is not targeting any one specific application.

For one implementation, an off-the-shelf photoresistor is used as the detector for proof-of-concept. Photoresistors are simple and inexpensive detectors, properties that are ideal for LOC devices. However, few groups seem to use photoresistors as the primary detector for their microfluidic devices as mentioned in section 2.2. This is possibly due to the fact that they are non-linear, which can be resolved by the use of a lookup table in the future. The photoresistor was measured to have a resistance of 3 MΩ under dark lighting conditions to as low as 110 Ω when exposed directly to the green LED light. It also consistently yielded 200 and 560 Ω when

directly exposed to the blue and red emissions respectively. This suggests that its spectral response curve is not perfectly flat since it does not follow the optical power trend previously measured by the Orion PD power meter. This has to be taken into account when the table of values is generated. For now, the ability of the photoresistor to provide a consistent reading is considered to be more important since other factors can be compensated for later on with the table of values. The photoresistor is connected in series with another resistor, as shown in figure 3.8, whose value is deliberately chosen to maximize the signal swing between when

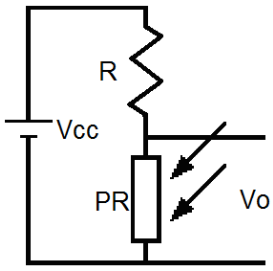

Figure 3.8: Schematic of photoresistor readout circuit. This circuit will essentially behave as a voltage divider, with the output V_o varying with optical intensity.

there is fluorescence and when there are none. From numerous tests, it has been determined that the photoresistor consistently yielded resistances of 3.5 and 5.24 kΩ under maximal fluorescence and no fluorescence respectively. Using these values and using the voltage divider equation for the orientation shown in figure 3.8,

$$\mathrm{V_{o,dark}} = \mathrm{Vcc}\frac{\mathrm{R_{photoresistor,dark}}}{\mathrm{R+R_{photoresistor,dark}}}$$
$$\mathrm{V_{o,light}} = \mathrm{Vcc}\frac{\mathrm{R_{photoresistor,light}}}{\mathrm{R+R_{photoresistor,light}}}$$

the following values are calculated:

Thus it is determined that a 4.3 kΩ resistor should be used in series with the photoresistor.

Resistor (Ω)	Vcc (V)	$R_{photoresistor,dark}$ (Ω)	$R_{photoresistor,light}$ (Ω)	$V_{o,dark}$ (V)	$V_{o,light}$ (V)	Voltage Swing (V)
4200	9	5240	3500	4.995763	4.090909	0.904854
4250	9	5240	3500	4.969442	4.064517	0.904925
4300	9	5240	3500	4.943396	4.038461	0.904935
4350	9	5240	3500	4.917623	4.012739	0.904884
4400	9	5240	3500	4.892116	3.987342	0.904774

Table 3.2: Sample output voltages calculated using the voltage divider equation. It can be seen that using a resistor value of 4.3 kΩ will provide the greatest signal or voltage swing.

The second implementation is to use an APD as the detector instead of a photoresistor. Although APDs can require high voltages for internal gain, they can also be operated as a normal photodiode with little to no biasing. This provides great flexibility in the design of the proposed device since one can design a circuit with biasing and one without. Other groups have also used photodiodes or APDs as their primary detector [1,2,11,15,16,21,24,26]. However, they typically use lasers as their source of excitation [11, 15, 16, 26], as well as optics and lenses [1, 2, 11, 16, 24, 26]. They also usually require a separate computer to show the values measured by their device [1, 2, 11, 16, 21, 24, 26], which is different from the proposed design since it is intended for the device to be truly stand-alone for ease-of-use and portability. Hamamatsu's silicon APD, S9073, was selected for use in the proposed device since it has a relatively wide spectral bandwidth to provide maximum flexibility with a minimal need for external, basic components. The wide bandwidth provided by silicon allows for the device to detect other fluorescence wavelengths by simply turning on the corresponding LED for the excitation wavelength required and applying the proper emission band-pass filter. The datasheet for the S9073 APD can be found on their website at [72]. Its responsivity is also acceptable for the range of interest

of 500 to 700 nm. It has a peak spectral response centred at 620 nm, and whose slopes for the spectral response curve become greater at higher gains. This means in order to maintain a relatively flat response curve, the biasing should be kept to a minimum. The APD was characterized with a Keithley 236 SMU by exciting it with the LED at various intensities and measuring the output photocurrent. Because figure 3.7 shows that the LED's output intensity varies linearly with the input power, it is reasonable to assume that the output optical power can be controlled and the response of the APD can be measured by a similar setup. Changing the input power to the LED should yield a graph similar to figure 3.7 since if the APD behaves in a linear fashion, then the output current should be proportional to the incident optical power. This can be seen in figure 3.9a) and confirmed in figure 3.9b).

3.2.2 Processing System

One special feature about the proposed device that is different than most is the integrated readout system. Thus far very few groups have integrated a readout system in their fluorescence system so that measurements can be directly read on-site [15,18]. For the readout display used in the proposed device, a three digit seven segment LED, LTC-561G from LITE-ON, is used. This means no external computer system is needed to receive and display the data. Before the values can be shown, the measured signal must first be processed. If the APD is used, then measurements must first be converted from current form into a voltage signal that can be more easily processed. This is accomplished by using a transimpedance amplifier circuit. As no biasing is used for this implementation, the circuit shown in figure 3.10 is used. It serves to convert the current signal from the APD into a voltage signal. The

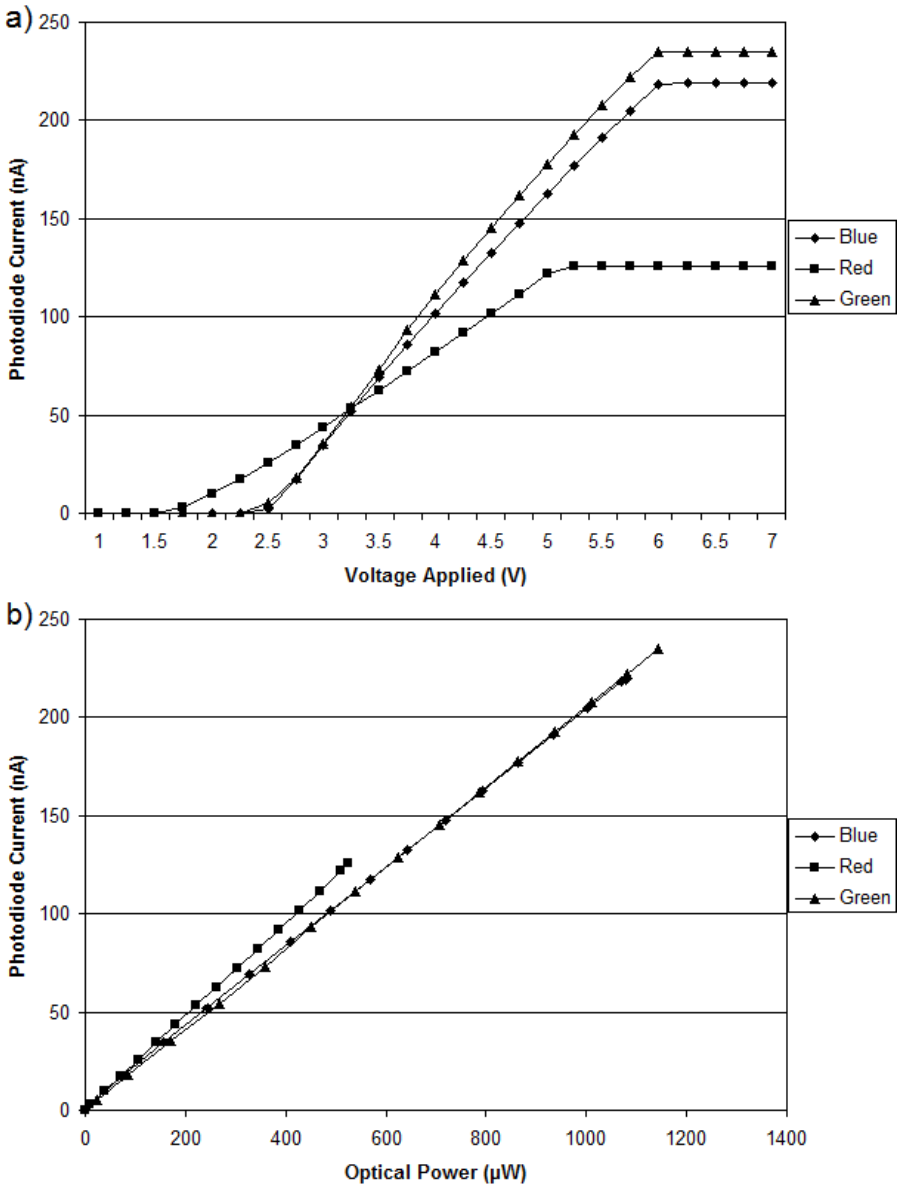

Figure 3.9: Graph of photodiode output current for each colour with respect to (a) LED bias voltage and (b) incident optical power by matching the LED bias voltage used. It is evident that the response is linear.

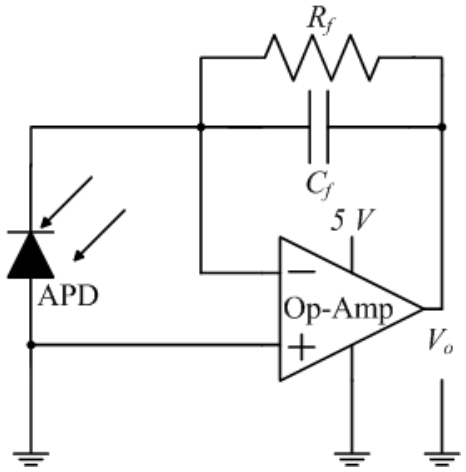

Figure 3.10: Schematic of the APD readout circuit.

operational amplifier used in the circuit is the AD8627 by Analog Devices. It has a comparatively low input bias current and low offset voltage. All of the information about the amplifier can be found at [73]. The low bias current property is important since it is desirable to minimize any noise when reading the photocurrent. It also has rail-to-rail output and supports single supply operation. These features are attractive as it simplifies the power aspect of the circuit considerably since only one voltage source is required. It is not necessary to provide a negative supply and having rail-to-rail output makes calibration much simpler. The feedback capacitor, C_f, has a total value of 2 nF and the feedback resistor, R_f, has a total value of 88 MΩ. This will give a bandwidth of approximately 0.9 Hz as determined by:

$$BW = \frac{1}{2\pi R_f C_f}$$

This low bandwidth is sufficient since it is not expected for the intensity of the samples to change quickly during measurements. The output voltage is measured

across V_o and should be approximately $V_o = I_{ph} \times R_f$ where I_{ph} is the photocurrent generated by the APD.

Regardless of whether the photoresistor or the APD is used, a microcontroller has been integrated to process the measured voltage signal into a readable form. While other researchers used Intel based processors for their applications [15, 18], a simple microcontroller is sufficient for the proposed device. The microcontroller being used is the PIC16F818 by Microchip. It has a built-in analog to digital converter (ADC), two 8-bit input/output pins, 1.75 kilobytes of program memory and 128 bytes of data memory. Full specifications can be found at [74]. The ADC feature is used to convert the analog voltage signal into a digital value so that the microcontroller can look up the corresponding values to output to the LED display. Since the LED display has eleven input pins, at least two 8-bit ports are required to drive the display instead of one. Thus far the amount of memory provided by the PIC16F818 is sufficient to display output values, but if additional tables are to be added, such as for calibration, then a microcontroller with more memory will be required. A program was written in assembly code to perform all of the tasks, such as accepting the analog signal, instructing the microcontroller to perform the analog to digital conversion, and to output to the correct pins so that values can be shown via the LED display in human readable form. Using a microcontroller also simplifies future modifications to the device should the need arise. This concept is very important since the device is initially limited in functionality to reduce the manufacturing cost. As a result, it should be able to be easily upgraded to increase its capabilities when the user needs to. The scalability of the proposed device is quite uncommon since most devices developed are targeted for specific applications.

3.2.3 Power System

Since the system is designed to be portable, the power source in mind is a common battery. With the exception of the APD, all of the components can be operated by a 9 V battery. If the APD is to be biased, then several additional 9 V batteries will need to be added into the transimpedance amplifier circuit. However, the need to do so has not yet arisen since the measurements obtained without biasing are acceptable. But to help increase the battery life of the device, two 9 V batteries are used instead of one. The microcontroller and the LED display each require approximately 5 V to operate, so a 5 V regulator, TPS7150 by Texas Instruments, was implemented to down convert the 9 V supply into 5 V. More information regarding the low-dropout voltage regulator can be found at [75]. Since the output of the microcontroller cannot surpass the supply voltage of 5 V, the LED display can be safely and directly driven by the output pins of the microcontroller as long as current limiting resistors are included. Consequently, to limit the LED display current to less than 20 mA, 255 Ω resistors are used.

3.2.4 Overall Layout

A diagram of the proposed device and a picture of the first prototype are shown in figures 3.11 and 3.12 respectively. All of the main components, such as the display and power systems, are located on the PCB block in the lower left corner of the picture. The PCB block includes the LED display and the PIC16F818 microcontroller on the top PCB while the power components are located on the bottom PCB. The aluminium holder that houses the sample, excitation LED(s), APD or photoresistor, and emission filter is located in the top centre. There is a

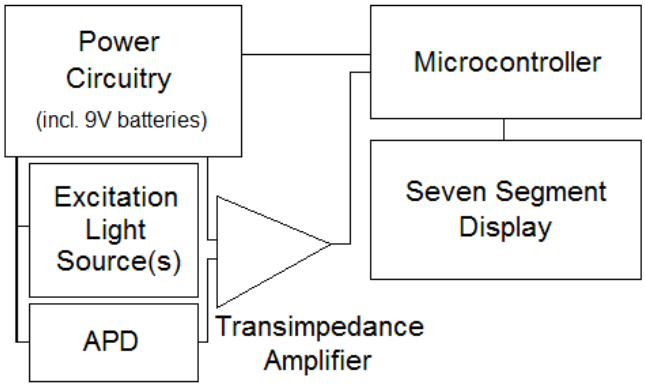

Figure 3.11: Block diagram of the major systems in the proposed device.

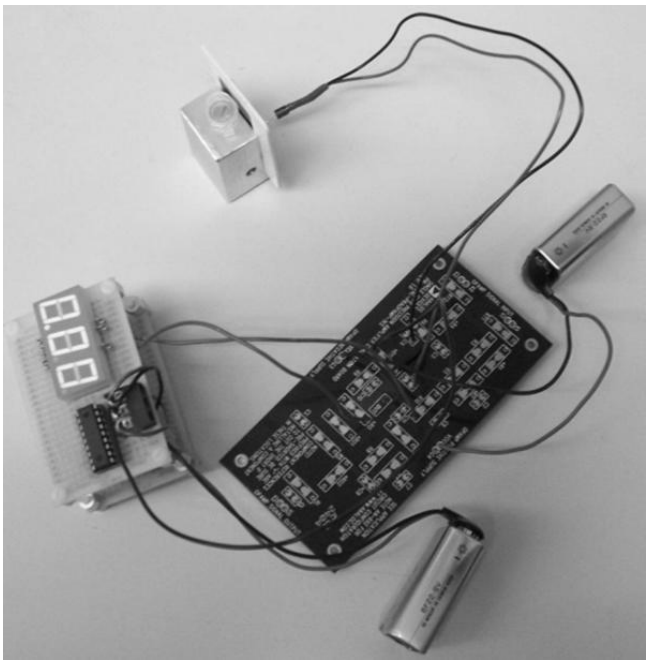

Figure 3.12: Image of the first version of the proposed device. The device is currently displaying zero intensity since the sample is not being excited (excitation LED not included in the picture).

slit in the holder for the filter, and adjacent to the filter is a small crevice that can house the detector. On the other side of the filter is a large hole that the sample is to be inserted into or pumped through. At right angles to the detector are two holes that the LEDs can be secured into. Right angles are used to minimize the amount of excitation light being aimed directly at the detector. Although band-pass filters should only allow the emission wavelengths through, not all filters have a perfect cut-off wavelength. In addition, due to the relatively wide spectral bandwidth inherent in an LED source, there may be photons from the LED that will be allowed through the band-pass filter. Consequently, precautions should be taken to prevent excitation photons from reaching the detector since they will result in noise. Everything that is needed for the operation of the device is shown in the picture, and it can be seen to be completely powered off of two 9 V batteries. It should be noted that while one battery is sufficient, dividing the power requirements and using two batteries should result in a longer operating lifetime. From figure 3.12, it is also evident that the space this device requires is considerably small. Even the first version of the device, where an evaluation board (EVAL-PRAOPAMP-1KS) provided by Analog Devices was used, is relatively small. Figure 3.13 shows the second version where all of the main components are now mounted on one small PCB and it is apparent that this device is highly portable. The first switch is used to turn the LED display and the detector on and off, while the remaining switches correspond to a possible excitation wavelength (e.g. red, blue, and green.) It may also be noticed that most of the components are socketed, thus improving the serviceability and upgradeability of the device since those components can be updated. Even the microcontroller is embedded in a dip socket so that it can be easily removed to be reprogrammed or even replaced.

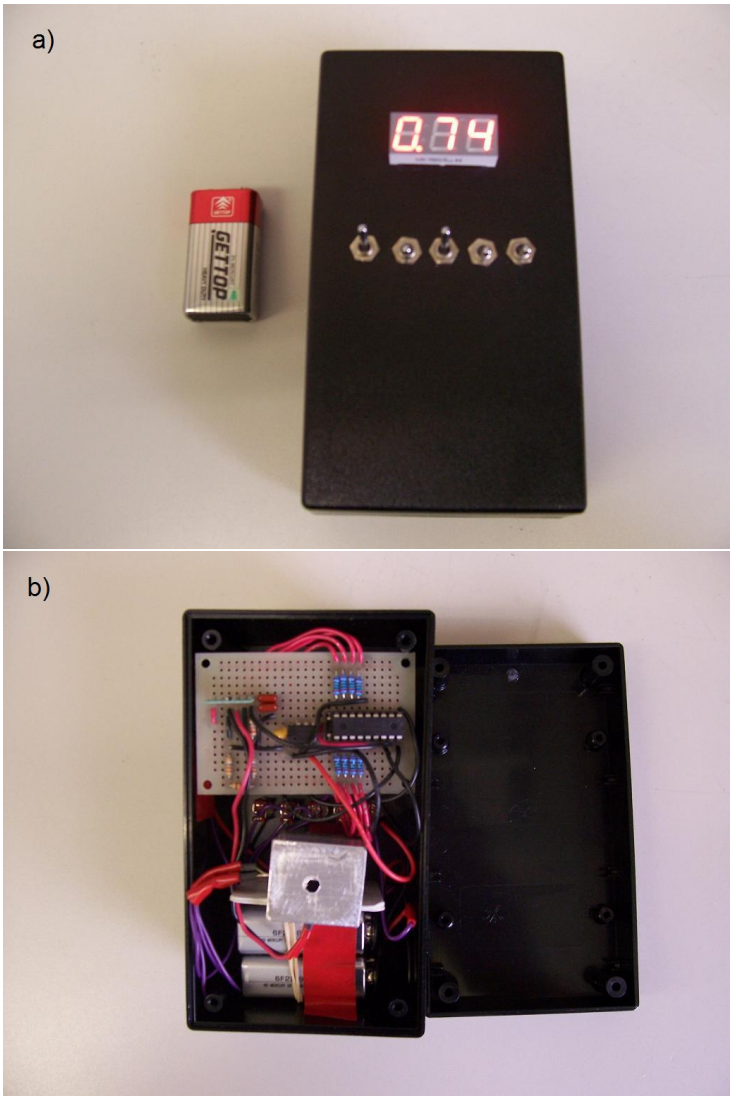

Figure 3.13: Images of the second version of the proposed device. (a) A 9 V battery is also shown to help make evident the small size of the device. (b) Image of the interior of the prototype device. It can be seen to be powered off of two 9 V batteries. Most of the space used is due to excessive wiring and the prototyping board, both of which can be easily remedied with better cabling and specifically designing a new PCB board.

3.3 Detector Results

Two main experiments were performed to characterize and determine the capability of the proposed device. The first experiment involved only fluorescein dye as the fluorescing sample under measurement. Fluorescein is a very commonly used fluorescent dye for applications such as flow cytometry and detector characterization. They are relatively inexpensive compared to other fluorescent dyes, are easy to prepare and use, and are fairly safe to work with. The second experiment uses a variation of the fluorescein dye to stain yeast cells. Since the main goal is to use the device for biological purposes, it is only sound to at least perform a measurement with real biological samples such as yeast cells.

3.3.1 Fluorescein Dye Measurement

Controlled experiments were performed to characterize the device and to ensure the repeatability of the experiments. Since one of the most basic applications is to determine the concentration of a specific analyte, such as fluorescing cells, solutions of different concentrations of fluorescein dyes were prepared as test sets. Fluorescence intensity measurements were first performed on the test sets by a PTI LS-100 fluorometer. The results from the highly sensitive commercial fluorometer will be compared with the results from the proposed device to help evaluate its performance. Two sample sets were initially created to help increase the number of test samples and in addition, the second set could help verify the measurements obtained with the first set. Each set should ideally contain concentrations of 5, 10, 15, and 20 mg/L of fluorescein dissolved in phosphate buffered saline (PBS). The PBS serves to keep the acidity level constant since fluorescein's excitation and

emission spectrum may change when the pH level shifts. Both products, fluorescein (CAB28406-32) and PBS (CA6508), were purchased from VWR International. Since the PBS purchased was in powder form, where 100 g of the powder mixed with 1 L of distilled water will make 10X concentrate, 10 g of PBS was mixed with 1 L of distilled water to create a 1X concentrate PBS solution. Because the fluorescein obtained was also in powder form, a stock solution of fluorescein was first created by mixing 100 mg of fluorescein powder in 50 mL of 1X PBS. This should yield a heavily concentrated solution of 2 g/L of fluorescein in PBS. Since the vials that were used to hold the samples can only store a maximum of 1.5 mL of any given solution, 2.5, 5, 7.5 and 10 μL of stock fluorescein at 2 g/L were mixed with 997.5, 995, 992.5 and 990 μL of 1X PBS to form 1 mL fluorescein concentrations of 5, 10, 15, and 20 mg/L respectively. This last process was then repeated to prepare the second sample set. The measured fluorescent intensities of both sample sets are shown in figures 3.14 and 3.15. Before readings of the actual fluorescein samples were obtained, a reading of distilled water was performed to warm the equipment up and for calibration. Each sample fluorescein concentration was then measured in order, and when all concentrations and samples have been measured, the process was repeated again. Readings of each concentration was spread out because the intensity of the excitation source may fluctuate over time. As a result, spreading out the reading for each sample instead of performing multiple readings of each sample at once will significantly reduce the overall error when the results are combined. Figure 3.14 shows the emission intensity of the fluorescein dye at each emitted wavelength for each concentration sample while figure 3.15 shows the total fluorescent intensity across the measured emission spectrum for each concentration for both sample sets. The PTI was set to an excitation wavelength of 470 nm since the LED excitation wavelength is at approximately that wavelength. It

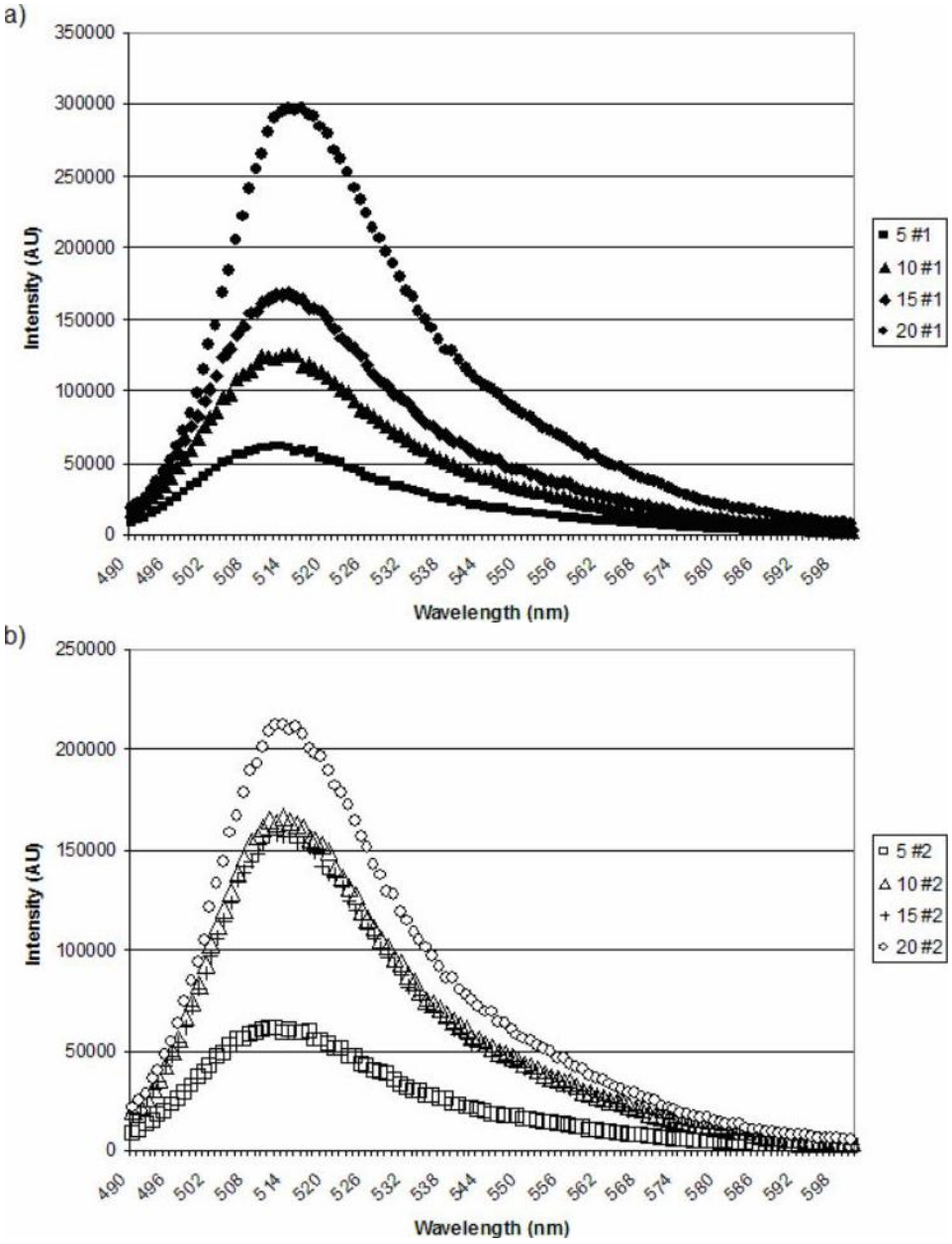

Figure 3.14: (a) Measured fluorescence intensities for sample set #1 and (b) set #2 by the PTI LS-100 fluorometer.

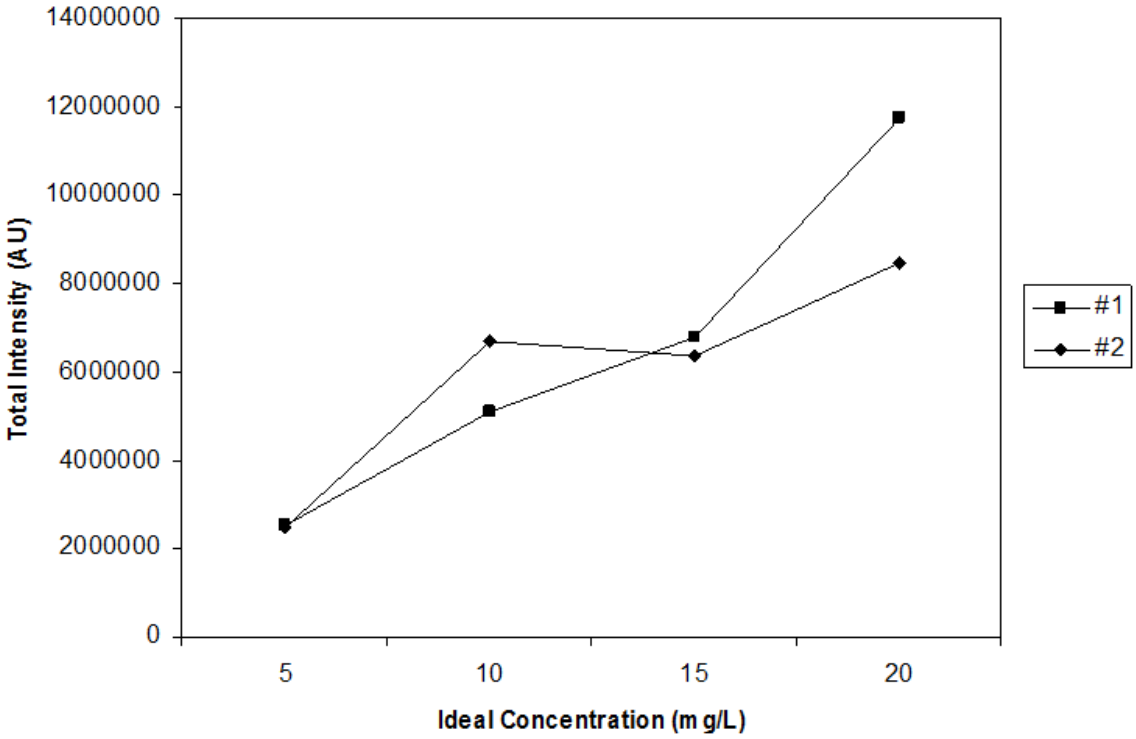

Figure 3.15: Total measured fluorescent intensities for both sample sets.

should be noted that summing the whole measured spectrum means wavelengths typically outside of the band-pass filters are included, so this will have to be taken into consideration. Although both sets of fluorescein dye should be identical to each other, figures 3.14 and 3.15 suggests that the concentrations between the two samples are not identical. For example, fluorescein concentrations of 10 and 20 mg/L differ significantly between the two sets. It is suspected that when these samples were created from the highly concentrated stock solution of fluorescein, not all fluorescein powder was dissolved properly in the PBS solution since the solution was already heavily saturated. Consequently, when samples were taken from the stock solution, there may be cases where a higher concentration was obtained

by the accidental intake of fluorescein in their highly concentrated powder form. However, because both sample sets were carefully tracked, it is still possible to use these sample sets in terms of comparing device performance. Although the exact concentrations of each of these samples are now uncertain, repeated measurements still yielded similar results. The repeatability factor is of greater importance since it verifies the stability of the solutions and that future measurements of the mixtures will still be indicative of its current state.

Several measurements were obtained using the first configuration, where the photoresistor was the detector, and their averages are shown in figure 3.16, along with the fluorometer readings for comparison. Since a coloured filter was used to block any excitation light coming from the blue LED, this effect has to be incorporated into the fluorometer readings. It was decided to be simulated by summing only the range of wavelengths that the filter allows through for the fluorometer measurements. Thus, it is assumed that the filter is an ideal filter with 100% and 0% transmission efficiencies for both the band-pass and band-reject areas respectively, and that the filter's transmission curve is perfectly square at the cut-off frequencies. It can be seen that by doing so, the fluorometer readings (dashed and semi-dashed lines) become significantly more similar to the measurements that the prototype device provided (diamond, solid line). Although the percentage error is considerable with a maximum of approximately 15% for the 15 mg/L sample in set #1, the device is still able to follow the trend or slopes outlined by the PTI LS-100 fluorometer. There are several possibilities for these errors, one of which is that when measuring with the PTI fluorometer, their cuvette had to be used. As a result, the fluorescein samples were transferred back and forth between each sample's container and the cuvette for each measurement. This transferring of solutions greatly increases the chance of contamination of the sample. Because of the

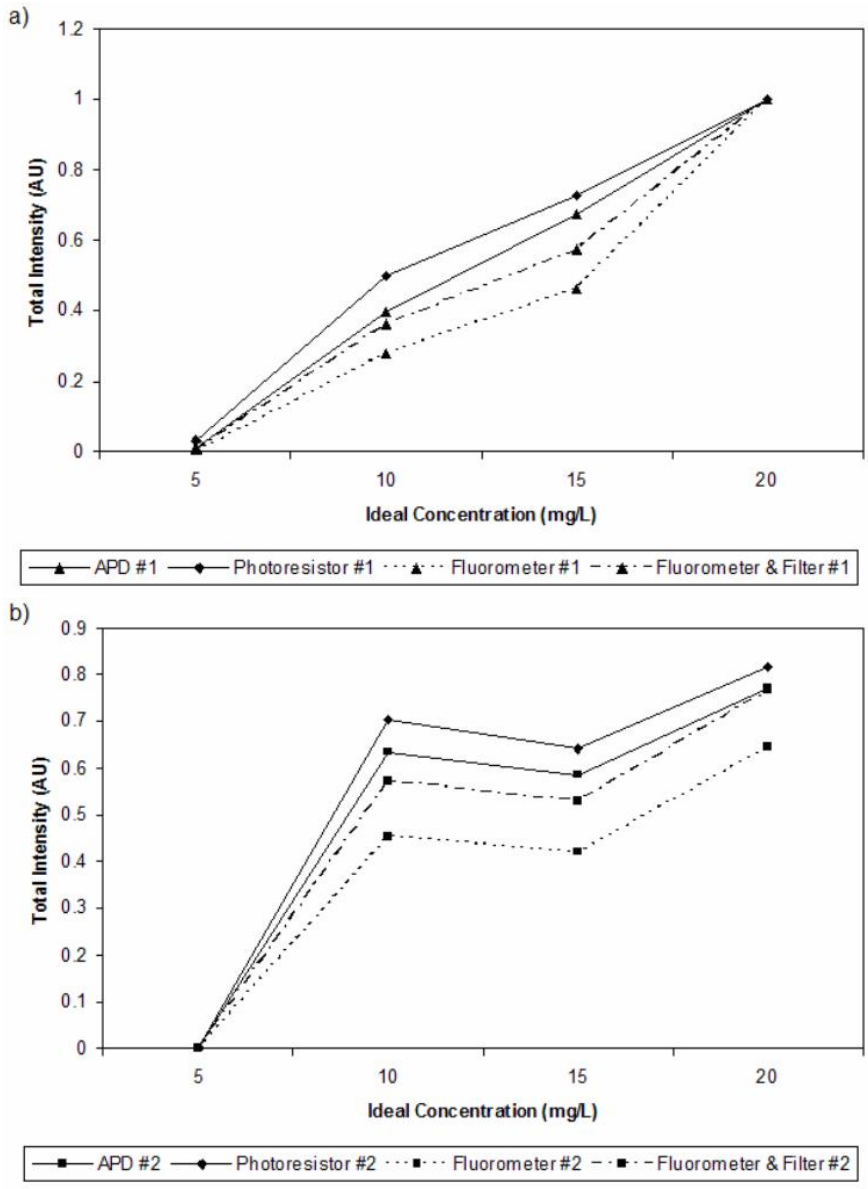

Figure 3.16: (a) Comparison of average fluorescent intensities as measured by the proposed APD and photoresistor based device to those measured by the PTI LS-100 fluorometer for sample sets #1 and (b)#2. Each pairs of data have been normalized for easier comparison.

low concentrations used, any slight change in concentration will be quite noticeable. In addition, photoresistors behave nonlinearly with respect to light intensity and a lookup table to compensate for the nonlinearity is not yet implemented to show the raw data; however, once the lookup table is included, it is expected that the readings will become considerably closer to those of the fluorometer. Comparing the photoresistor to the PTI fluorometer, the dip in sample #2 for the supposed 15 mg/L concentration are both quite noticeable and both have similar, albeit not identical, overall slope patterns. Nonetheless, the relative positions for each concentration in both devices are similar. Plots of sample #1 show the greatest differences, possibly due to the reasons listed above, but the overall plot is still present. This at the very least proves that the photoresistor is indeed capable of detecting relative fluorescent intensities and demonstrates to be a promising detector. If it is taken into account that an off-the-shelf photoresistor that costs only a couple of dollars was used, then this suggests that further investigations of using photoresistors as fluorescence detectors is warranted. They become even more attractive since a large number of similar devices can be manufactured at low cost due to their optoelectronic semiconductor nature. These devices can be used for simple applications such as determining the presence of fluorescence. Doing so will help make commercial devices available to be used for more complex applications such as cell counting. If the difference in concentration is expected to be reasonably large, then photoresistors can also be used for relative comparison purposes. In addition, if one were able to design the photoresistor being used, then the responsivity of the photoresistor can be more accurately controlled and determined. This should in theory further improve the accuracy of the device since the designer can control all variables and set the constraints.

For the second configuration, where the non-biasing setup shown in figure 3.10

is used instead of figure 3.8, several measurements under blue excitation were also obtained. Again, their average results are shown in figure 3.16 along with the other plots to help make the comparisons easier. It is immediately clear that the performance of the APD is considerably closer to the results of the fluorometer than the photoresistor. The percentage error was reduced considerably, to an average of approximately half as much as those produced by the photoresistor. This is to be expected since the APD has a linear response and greater sensitivity. Errors should be able to be further reduced with the implementation of a calibration lookup table. However, errors due to contamination cannot be corrected and can still be observed in the plots yielded by sample sets #1 and #2. Their dissimilarities with each other are still quite apparent, but this proves that the APD is also able to follow the slopes and peaks that the fluorometer plotted. In fact, they are more representative of the fluorometer plots. This supports the fact that APDs are also capable detectors for use in fluorescence detection and that they should be seriously considered for LOC devices.

A larger set of samples was also prepared to try to obtain a more accurate assessment of the prototype. Fluorescein concentrations of 4, 8, 12, 16, 20, and 24 mg/L were first measured in a FP-6000 series spectrofluorometer manufactured by Jasco. They were then measured by the prototype under blue LED excitation with the APD installed. Both results are shown in figure 3.17. It can be seen that the curve determined by the proposed device closely follows the curve that the spectrofluorometer plotted. The smallest possible concentration sample that was accurately prepared (4 mg/L) was also detected. Furthermore, it can be clearly seen that the rate of change of intensity decreases as the concentration increases to a point where the slope becomes negative, which is approximately after 12 and 16 mg/L for the fluorometer and APD readings respectively. This is most likely

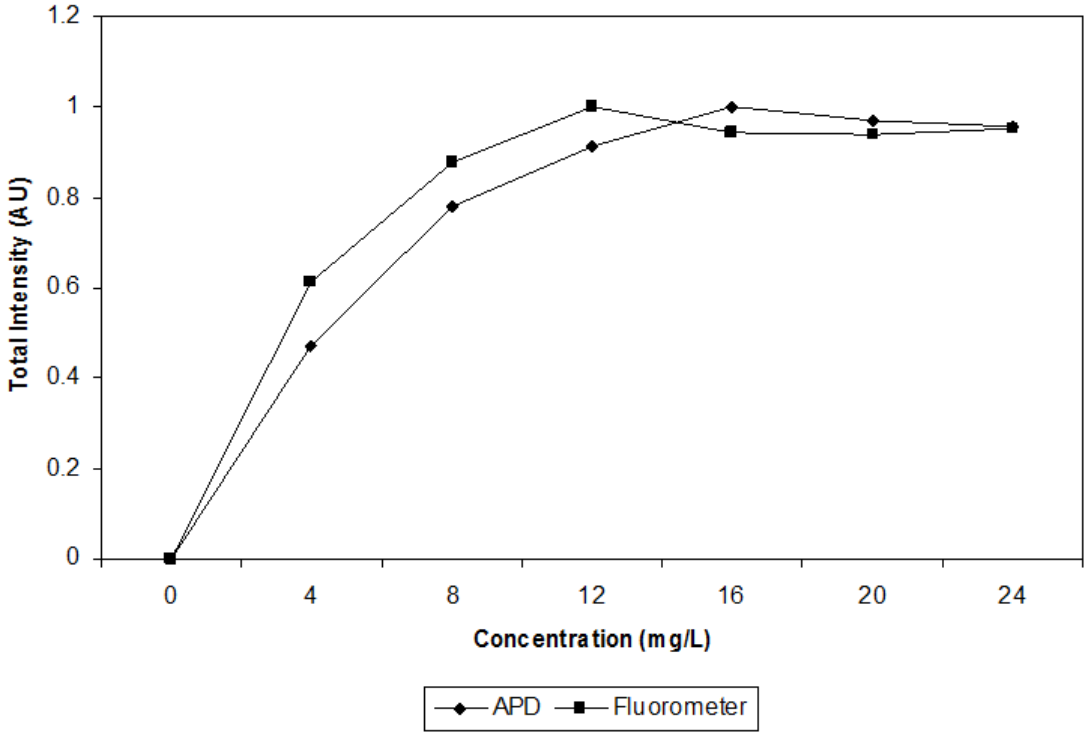

Figure 3.17: Comparison of average fluorescent intensities as measured by the APD based prototype to those measured by an FP-6000 series spectrofluorometer. Values have been normalized again for comparison.

due to the inner-filter effect that was explained in section 3.1.3. The FP-6000 series spectrofluorometer yielded relatively noisy results, so several measurements had to be taken to generate the curve. This should not be surprising because although the cause of the noise is unclear, it is suspected that since the cuvettes used to hold the samples during measurements were made of disposable plastic with frosted windows, slight differences in alignments between various readings could significantly impact the dispersion of the photons when they pass through the rough surface. This added to the fact that since the FP-6000 uses a PMT detector, so it is highly sensitive, the dispersion of photons through the rough surface can

be quite appreciable. However, the general trend is still present, including the dip after the peak due to what is suspected to be the inner-filter effect. Although the concentrations at which the slopes become negative are different for the two devices, they are relatively close to each other in terms of intensity, so they are still in relative agreement with each other. It should again be noted that no additional optics were used for all of the measurements. That means components such as objective lens, aspheric lens, and fibre optic cables were not used for the collection, focusing, and propagation of light. In addition, the APD was not biased when the measurements were obtained. Taking these facts into consideration, these results are very promising for a low cost, versatile, integrated fluorescent LOC device as that means even normal photodiodes should produce similar results since no bias was applied to the APD. The S9073 APD used costs approximately $72 USD. That price is relatively inexpensive when compared to the other highly sensitive detectors, such as PMTs and photon counters, which are commonly found in fluorometers and other large fluorescence analysis systems. This also suggests that normal silicon photodiodes may be obtained at an even lower cost, thereby further reducing the cost of the LOC fluorescence system.

To ensure that this result is only due to the fluorescent dye, several controlled experiments were performed. Measurements of various fluorescein and PBS concentrations were taken. Figure 3.18 is a plot of fluorescein sample set #2 and a pure water sample (0 mg/L data). For those measurements, the filters used were as close to the excitation wavelengths as possible. This helps in the investigation and determination of the inner-filter effect, which can be readily seen in the figure. Because fluorescein is not excited by the red LED, the red plot yielded no fluorescence compared to a pure water sample. However, when the green LED and filter is used, it is immediately apparent that the dye is emitting its own green light since

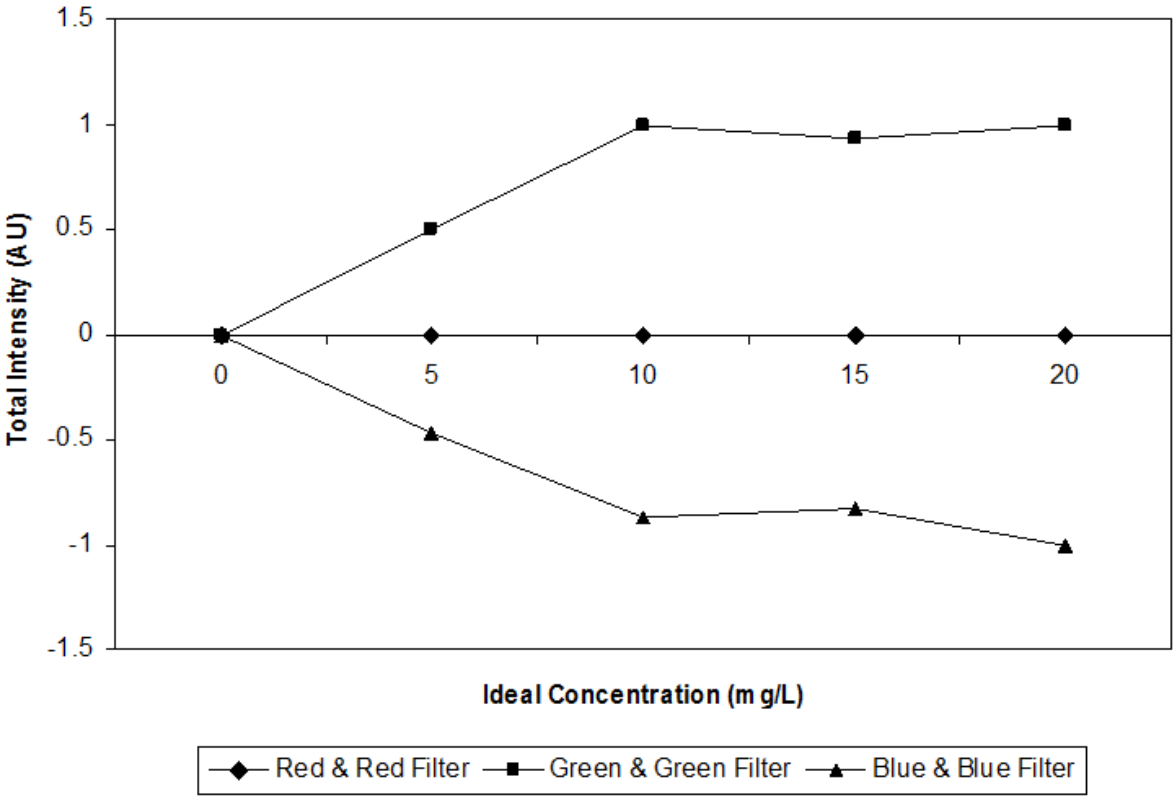

Figure 3.18: Average intensity plot of fluorescein in three different settings. Each plot has been normalized to account for different spectral response curves for the different filters and wavelength region used.

the measurements were significantly greater than when compared to the pure water sample. Although fluorescein's peak absorbance wavelength is approximately 470 nm, its absorbance spectrum does spread into the green wavelength (figure 3.5), so it is being excited by the green LED. When the blue LED and filter is used, the green fluorescence emitted by the dye is blocked by the blue filter, and the overall intensity decreases when compared to a pure water sample as the fluorescein concentration increases. Since it is known that fluorescein is excited by the blue LED, then this suggests that the blue light is being absorbed by the fluorescein

dye, resulting in a lower intensity than the pure water sample. This is a sign of the primary inner-filter effect. Since any green light emitted by the dye will be blocked by the filter, the secondary inner-filter effect cannot be accurately measured by this method. When measuring varying concentrations of PBS, it was determined to have the same response as a pure water sample, which is to be expected, so the results of that are not shown.

3.3.2 Stained Yeast Cells Measurement

Since one of the objectives of the device is to determine the concentration of cells in a sample, a test set of yeast cells stained with carboxyfluorescein diacetate, succinimidyl ester (CFDA-SE) was also prepared. The Vybrant CFDA SE Cell Tracer Kit from Invitrogen was used to prepare the dye. Because the CFDA dye is a fluorescein derivative, it is expected to perform similarly to a sample of pure fluorescein dye. The procedure to stain the cells is as follows. First a concentrated stock solution of 7.5 mL of yeast cells with an optical density of 0.85 OD^{600} was prepared. The OD^{600} is a measure of the absorbency of the solution or sample at 600 nm. This wavelength is used since many biological cells absorb this wavelength, thus concentrations of cells may be obtained by measuring the amount of light absorbed across the sample. The solution was then centrifuged to obtain pellets of yeast cells and thoroughly mixed with 3.5 mL of CFDA solution to stain the cells. After letting it sit and incubate to stain, the 3.5 mL cell and CFDA solution was centrifuged again to recover the yeast cell pellets, which were then thoroughly mixed with 3.5 mL of PBS. This effectively removes the CFDA dye from the solution, so any remaining dye should be those confined in the cells. By removing the dye from the solution, it is ensured that any fluorescence measured is due to the stained cells

and not from the CFDA dye in the solution. Then 1, 0.75, 0.5, and 0.25 mL of stained cell samples were obtained from the solution and 0.25, 0.5, and 0.75 mL of PBS were added to the latter three cell samples to create four samples, each with a volume of 1 mL. This should in theory result in relative cell concentrations of 100%, 75%, 50%, and 25%. Measurements of the stained cells were taken by the APD based prototype in non-biased mode, and the results are shown in figure 3.19. It can be seen that as the concentration of the stained yeast cells decrease, the

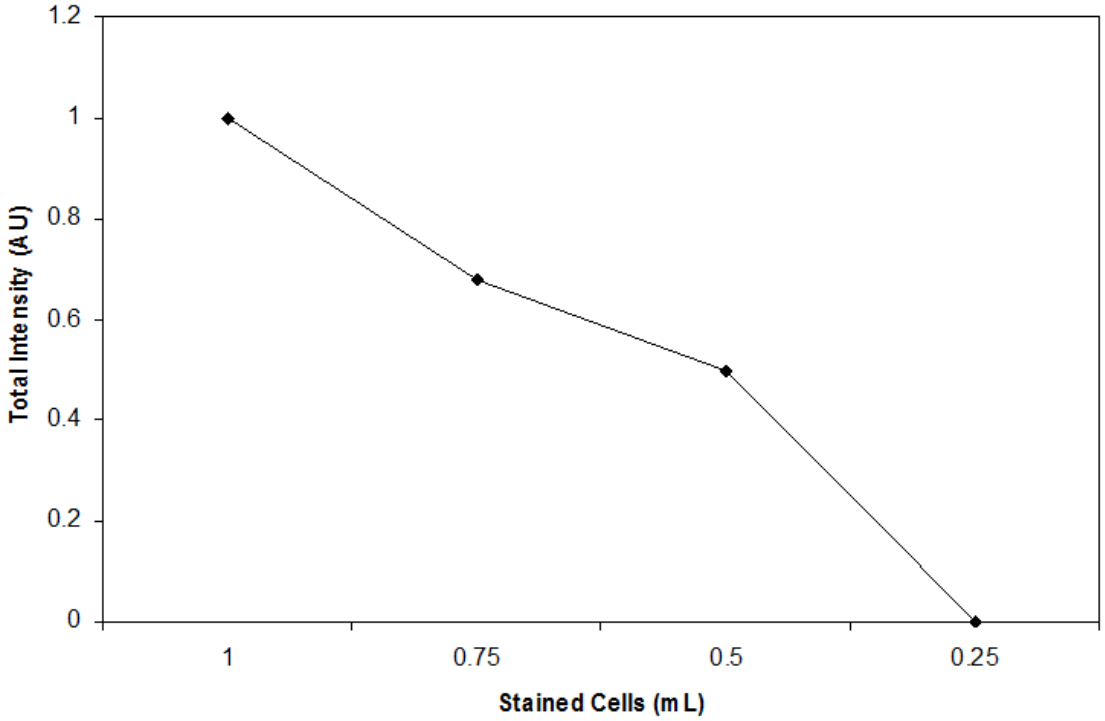

Figure 3.19: Normalized average intensity plot of yeast cells stained with CFDA.

intensity decreases as well, which is expected. However, there appears to be a hump at 0.5 mL, and at 0.25 mL the fluorescence intensity was too weak to be accurately detected, yielding results comparable to pure PBS, which is not shown. This shows that there is a minimum sensitivity for the prototype of between 0.25

and 0.5 mL of material stained with CFDA if made from a 7.5 mL stock solution at 0.85 OD^{600}. Nevertheless, the overall trend using real, stained yeast cells is plotted, showing that the concept of the proposed device is promising for applications where the sample is abundant.

Again, to ensure that the results of the test is only due to the CFDA dye, measurements of various concentrations of unstained yeast cells were performed under red, blue and green excitation. The averaged results are shown in figure 3.20. For

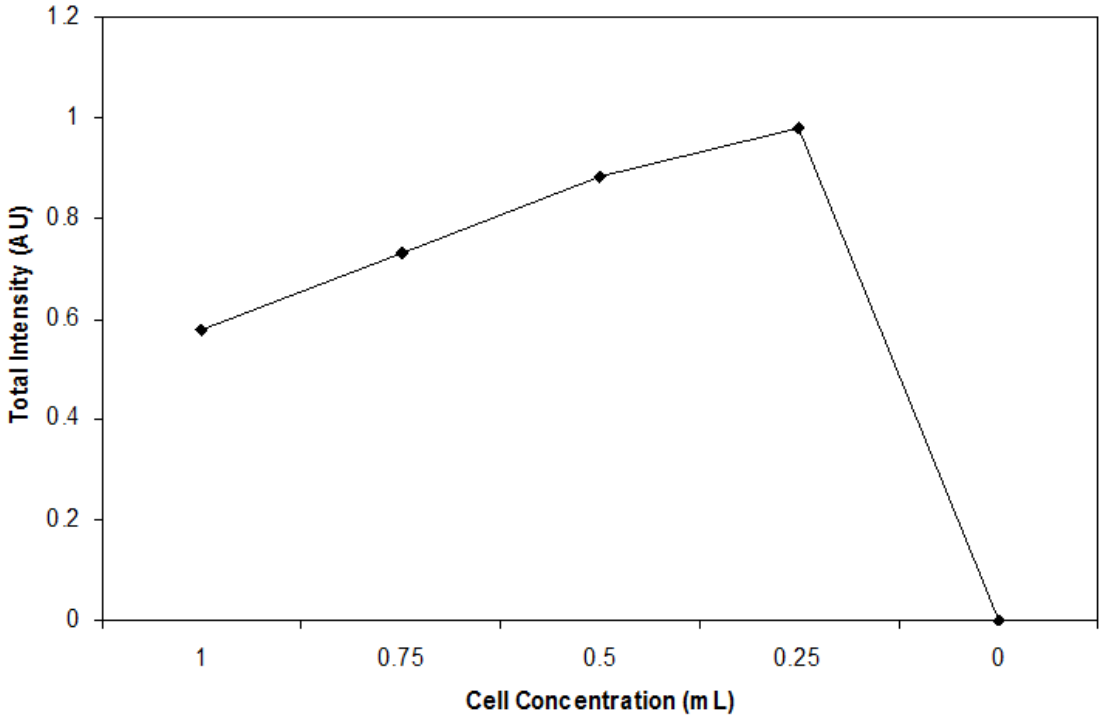

Figure 3.20: Normalized average intensity plot of unstained yeast cells.

this measurement, a highly concentrated solution of yeast cells was prepared and then centrifuged to obtain the yeast cell pellets. The pellets were then thoroughly mixed in the same volume of distilled water, from which 1, 0.75, 0.5, and 0.25 mL of clean yeast cell solutions were drawn and mixed with 0, 0.25, 0.5, and 0.75 mL

of distilled water respectively. A pure distilled water sample was also created as a control sample. The transferring of yeast cells to distilled water was necessary since the medium that the cells were incubated in was not transparent, so they would considerably affect the intensity readings. The plot shown in figure 3.20 shows that as the concentration of the cells decrease, the intensity increases. This is suspected to be due to fewer cells blocking or absorbing the light on their way to the detector. However, it is obvious that samples with cells yielded higher intensities than when compared to the pure distilled water sample (0 mL cell concentration). This further suggests that the cells themselves are scattering light from the LED into the detector. Consequently, another possible application for the device is to determine the concentration of cells without even staining them by simply measuring the amount of reflected light. This result also further verifies the results in figure 3.19 since when the amount of CFDA stained cells decreased, the intensity decreased instead of increasing. That means the smaller concentration sample absorbed less excitation light, so fewer emission photons were generated. Conversely, for the greatest cell concentration sample, there were a larger number of cells absorbing the excitation light, so more emission light was given off.

3.4 Summary

It is shown that it is possible to integrate a multicoloured LED, a detector such as a photoresistor or APD, an LED display, a microcontroller, and various filters to create a truly portable, versatile, stand-alone fluorescence detection system. The results obtained by the prototype device follow closely with those recorded by bulky, expensive fluorescence analysis systems. Thus it is shown that it is possible to use

relatively inexpensive and very few components to create a device that can yield similar results. This allows the currently used, more expensive, machines to be assigned to more complex tasks. The result should be an overall improvement in operating costs. Because the prototype requires very little power, few components, and has a built-in LED display, it is possible for it to be completely handheld and truly portable. By running off of batteries, simple tests can be performed on-site. New applications for the device are possible with a proper excitation source and detector, and the microcontroller can be updated, increasing its versatility. With multiple excitation wavelengths due to the three colour LED and additional LEDs, various fluorescent dyes can be used concurrently. Based on the promising results of these experiments, further work, such as to design a detector tailor made for the device should be considered. Developing a tunable filter is also an objective, which will be discussed in the following chapter. Although multi-wavelength excitation is currently possible with the prototype, the detection filter still has to be manually changed. Being able to automatically tune across a range of wavelengths will significantly improve the functionality and automation of the prototype.

Chapter 4

MEMS Diffraction Grating Design

Most optical analysers incorporate a method of wavelength selection. This ability is important to be able to selectively pick the signal or wavelength of interest. Wavelength selection can be achieved in a variety of ways. Possible solutions range from using a selection of fixed filters, such as a filter wheel, to wavelength tuning based on the principles of interferometers or diffraction gratings. Because MEMS based devices have the potential of keeping both cost and size to a minimum, both of which are important for LOC devices, the second objective of this thesis is to introduce a MEMS based diffraction grating for wavelength tuning. The feasibility of the concept of using a MEMS diffraction grating will be demonstrated through simulations and indirect tests.

4.1 Background Theory

A good understanding of optical physics have allowed for much progress in the field of optics. Various lens and optical filters have been designed to yield minimal dispersion and attenuation for certain cases. Blazed and holographic gratings are two such examples. They are simply diffraction gratings with a slightly different mechanical structure than the typical gratings to change the optical properties. With the development of micromechanical structures that can be actuated to change the physical shape of the structure, it is logical to implement diffraction gratings using MEMS technology since its structural versatility lends well to diffraction gratings. Their semiconductor nature is also highly suitable for mass production, which will eventually help keep the cost down.

4.1.1 Huygens' Principle

Since most sources on the topic of diffraction will introduce the subject with a brief discussion on Huygens' Principle, it is logical to do the same here. However, the readers are wholly encouraged to consult textbooks such as [58, 76] for greater detail.

In 1678, Christian Huygens made a proposition in favour for the wave theory of light [76]. He made the now famous postulation that every point on the wavefront of an incident wave or disturbance at some aperture can be considered as a new source of secondary spherical waves of identical phase and frequency as the original wave. Adding these secondary wavelets by superposition in the forward direction will result in an envelope or a new wavefront, and it is this new envelope that results in diffraction [58, 76]. This is illustrated in figure 4.1. The diagram illustrates that

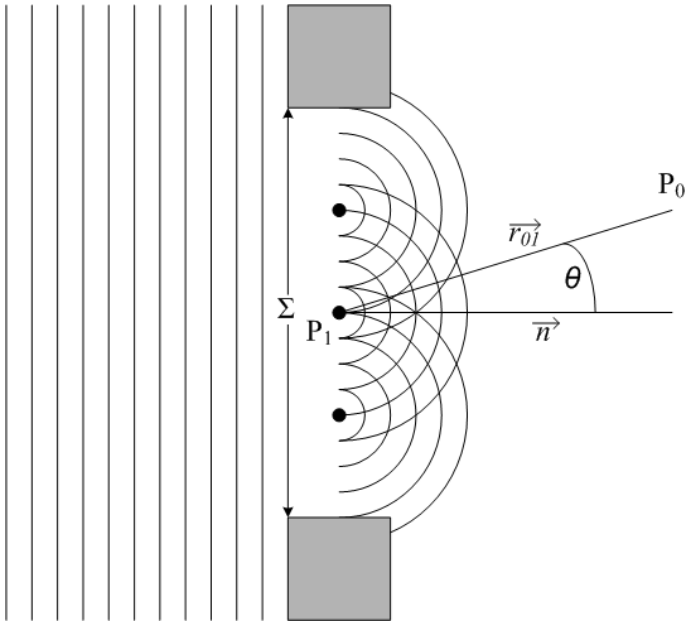

Figure 4.1: Diagram illustrating Huygens' principle, showing secondary spherical wavelets at the wavefront of an aperture.

plane waves incident to a rectangular slit of similar scale will produce diffraction, and that the diffraction pattern, such as when viewed from P_0, can be determined by the interference of an infinite number of individual spherical wavelets in the forward direction. These secondary spherical wavelets originate from points P_1 along the aperture Σ at the original wavefront. This idea was heavily disputed at the time, but in the year 1804, Thomas Young proposed the idea of the interference of light to produce light and dark areas, which could be used to support Huygens' theory [76]. Thus in 1818, Augustin Jean Fresnel combined the two ideas, and in 1882, Gustav Kirchhoff formulated the now commonly known Huygens-Fresnel principle [76]. Although the approximations used to formulate the principle were flawed, the results predicted are still relatively accurate. Several attempts were made to modify Kirchhoff's theory, and one of them was by Arnold Sommerfeld that

resulted in the Rayleigh-Sommerfeld diffraction theory. The Rayleigh-Sommerfeld diffraction formula that describes the Huygens-Fresnel principle is [76]:

$$U(P_0) = \frac{1}{j\lambda} \iint_{\Sigma} U(P_1) \frac{\exp(jkr_{01})}{r_{01}} \cos\theta ds \tag{4.1}$$

where $U(P_0)$ is the observed field at point P_0 and it is the sum of all of the spherical waves originating from every point P_1 along the entire aperture Σ. Other parameters in the equation is λ for the wavelength of the incident wave, k for the wave number, and θ for the angle between the normal vector of the aperture, $\overrightarrow{n}$, and the vector $\overrightarrow{r_{01}}$.

4.1.2 Fresnel and Fraunhofer Diffraction

Diffraction can fall into one of two main categories: (i) Fresnel diffraction or (ii) Fraunhofer diffraction. Equation 4.1 can be rewritten for each case, depending if the screen is far field or close to the aperture [77]. Fresnel diffraction occurs when both the source and the diffraction screen are close to the aperture, and thus is known as near field diffraction. Conversely, far field diffraction, or Fraunhofer diffraction, exists when the source and diffraction screen are very far from the aperture. For Fresnel diffraction, in rectangular coordinates, equation 4.1 becomes the Fresnel diffraction integral [76]:

$$U(x,y) = \frac{e^{jkz}}{j\lambda z} e^{j\frac{k}{2z}\left(x^2+y^2\right)} \iint_{-\infty}^{\infty} \left\{ U(\xi,\eta) e^{j\frac{k}{2z}\left(\xi^2+\eta^2\right)} \right\} e^{-j\frac{2\pi}{\lambda z}(x\xi+y\eta)} d\xi d\eta \tag{4.2}$$

where P_0 and P_1 is now replaced by the coordinates (x, y) and (ξ, η) respectively and z is the distance from the aperture to the screen plane. In the case of Fresnel diffraction, the incident wavefront to the aperture may not necessarily be flat,

especially if the source is a point source. Similarly, the envelope created by the secondary wavelets may not necessarily form a planar wavefront at the diffraction screen due to the close proximity. If the incident wave and the diffracted waves are planar, or at sufficient distances where

$$z \gg \frac{k}{2}\left(\xi^2+\eta^2\right)_{max}$$

then the Fraunhofer diffraction integral can be used, which is just a simpler form of 4.2 [76]:

$$U(x,y) = \frac{e^{jkz}}{j\lambda z} e^{j\frac{k}{2z}\left(x^2+y^2\right)} \iint_{-\infty}^{\infty} U(\xi,\eta) e^{-j\frac{2\pi}{\lambda z}(x\xi+y\eta)} d\xi d\eta \tag{4.3}$$

In either case, it can be seen that the intensity depends on the incident wavelength λ and the angle formed by $\overrightarrow{r_{01}}$ with respect to the normal vector, as determined by (ξ,η) and (x,y). This relationship will play a big role later on in explaining the diffraction grating equation.

4.1.3 Diffraction Grating Equations

At present time, there are numerous types of diffraction based optical elements. One of their main purpose is to separate the incident light based on their constituent wavelengths. Examples of such optical elements include ruled diffraction gratings, holographic diffraction gratings, diffractive lens, and concave gratings. They typically belong to one of two types: (i) transmission grating or (ii) reflection grating. Ruled diffraction gratings are typically fabricated by a ruling engine that directly cuts grooves into the substrate. Consequently, it is more prone to errors due to the direct physical interaction involved. Holographic diffraction gratings are

produced by light interference and photolithography, which should result in fewer errors since little to no physical contact is needed for fabrication. Diffractive lens or Fresnel lens can also be used to help separate a beam of light into its individual components. Concave gratings are essentially concave mirrors with grooves so that the incident light can be separated into their individual wavelengths. It can also be used to focus the light, thus eliminating the need for additional external optics. Diagrams of these diffractive optical elements are shown in figure 4.2 [77]. All of the diffraction based optics previously listed share the same principle of operation and purpose. The most common effect is an angular dispersion of the component wavelengths, as seen in figure 4.2c). This can be explained by the wave nature of light. As light approaches a feature of approximately the same scale as its wavelength, it will behave like a wave and bend around the feature as previously explained by Huygens' principle. Thus, when the wavefront strikes a feature, such as an edge or a corner of a substrate, the interface will become individual point sources with light spreading out in all directions from that point, as shown in figure 4.1. The consequence of this effect is that light will appear to bend around the feature. As a result, this phenomenon can be taken advantage of and specific ranges of wavelengths can be designed for by simply modifying the feature size of the gratings. It was previously determined from equations 4.1, 4.2, and 4.3 that the diffraction pattern depends on the wavelength λ and the diffraction intensity depends on the diffracted angle. Therefore it is reasonable to presume that the diffraction grating equation should contain those parameters as well. Thus, the effect of diffraction of light based on the incident wavelength can be described by the commonly used diffraction grating equation:

$$m\lambda = d(\sin\theta_i \pm \sin\theta_r) \tag{4.4}$$

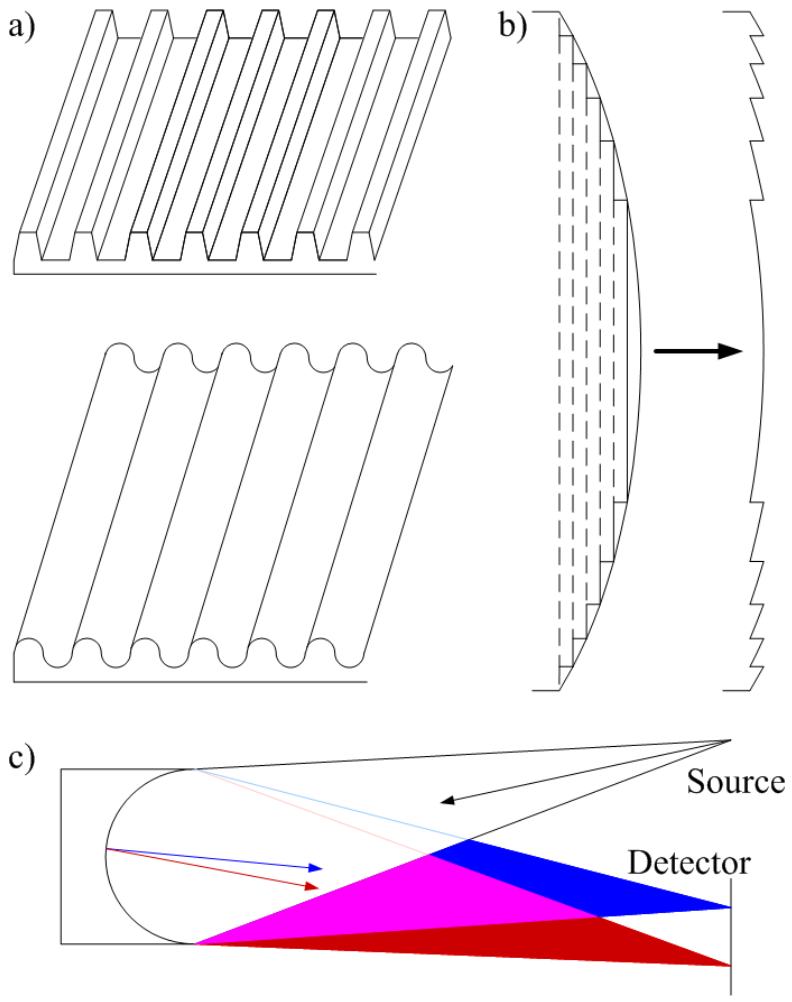

Figure 4.2: Diagrams of different diffractive elements. (a) Ruled and holographic diffraction grating. (b) Diffractive or Fresnel lens. It works on the principle that the diffraction is dependent on phase delay, so by removing blocks of unit wavelengths from the lens, a thinner Fresnel lens can be created to achieve the same effect. (c) Concave grating used to separate incident light into their constituent wavelengths via spectral dispersion. The detector can be a planar detector array, which is a configuration commonly found in spectrometers.

where m is the diffraction order, λ is the incident wavelength, d is the grating period, and θ_i and θ_r are the incident and diffraction angles respectively. The

diffraction order m can be negative and are integers (e.g. 0, ± 1, ± 2, ± 3) and the equation uses subtraction if the reflection or diffraction angle is on the opposite side of the normal to the incident angle. Similar to what was stated previously, the equation also suggests that the order of magnitude of the feature size, the grating period d in this case, should be comparable to that of the wavelength of interest λ to obtain plausible values. It also takes interference into consideration with the incorporation of the diffraction order. This also indirectly suggests that grooves in a reflection grating serve to change the phase of the reflected light by altering the path length. This phase change will result in either constructive or destructive interference when interacting with other light. The constructive interference at the far field will result in a specific diffraction order, appearing as a peak on a screen. However, normally only the first few diffraction orders contain enough light to be useful. The more important aspect of equation 4.4 is how it relates the incident and diffraction angles, θ_i and θ_r, to the wavelength λ and grating period d. It can be seen that by increasing the wavelength of interest and keeping all other variables constant, the diffracted angle will increase. This means that should a beam of white light be focused on the grating, the reflected beams will be spread out with the shorter, blue wavelength closest to the normal and the longer, red wavelength furthest away, as seen in figure 4.2c). Thus, a diffraction grating in conjunction with a detector array to collect the diverging beams can form the basis of a spectrometer. Conversely, it can also be seen that by increasing the grating period and keeping all other parameters constant, the diffraction grating is now effectively designed for a longer wavelength. This effect will be exploited for the purpose of wavelength tuning.

Equation 4.4 also shows that a monochromatic light can be simultaneously diffracted into multiple angles as determined by their diffraction orders. Conse-

quently, the power of the incident light is distributed across all of the diffraction orders, with the zeroth order containing the most power. However, the zeroth order is not normally used since it is wavelength independent. This means all wavelengths share the same zeroth order in terms of angular dispersion. In other words, all of the incident wavelengths will be partly diverted into that angle. As a result, it is usually the first and second diffraction orders that are of interest, but they have lower power compared to the zeroth order. The powers of each diffraction order can be determined by [50]:

$$P(\theta_r) = P_o \frac{\sin^2\left[\pi \frac{w}{\lambda} \sin\theta_r\right] \sin^2\left[N\pi \frac{d}{\lambda} \sin\theta_r\right]}{\left[\pi \frac{w}{\lambda} \sin\theta_r\right]^2 \sin^2\left[\pi \frac{d}{\lambda} \sin\theta_r\right]} \tag{4.5}$$

where $P(\theta_r)$ is the optical power at a given diffraction angle θ_r, P_o is the total optical power at the grating, w is the slit width, λ is the incident wavelength, N is the number of slits, and d is the grating period. From equation 4.5, it can be seen that maximum powers occur when $sin\theta_r$ has a magnitude of 1 and the ratio of the grating period to the product of the slit width and diffraction order, wm/d, satisfies the equation $1/2 + x$, where x is an integer. Thus, by changing the slit width and grating period, it is possible to attenuate specific higher diffraction orders. In their example, if the width to grating ratio is $d = 2w$, then any even diffraction orders (e.g. ± 2, ± 4, ± 6) will be attenuated.

Another reason to use higher diffraction orders is that the resolving power of a diffraction grating is directly proportional to the diffraction order being used. This is given by equation 4.6, where R is the resolving power, m is the diffraction order, and N is the total number of slits in the grating:

$$R = mN \tag{4.6}$$

Thus, according to the equation, the more slits there are in the grating, the greater the resolving power will be. It also provides an incentive to use higher diffraction orders since second order patterns should theoretically have twice the resolving power of the first order. However, as suggested by equation 4.5, higher orders will result in lower optical power. This is a trade-off that must be taken into consideration.

To help direct more incident light into higher order angles to increase their optical power, a technique called blazing is used [42]. Blazed gratings are characterized by their saw-tooth shaped profiles instead of square pits or wells. Consequently, the surface is now at an angle with the plane of the substrate instead of lying perfectly parallel to the plane. The angle created by the saw-tooth and the substrate plane is called the blaze angle, and is unique for each wavelength. This can be taken advantage of since blaze angles can be designed for certain wavelengths of interest. When operating at those wavelengths, they will more likely be reflected into the desired angles or higher diffraction orders. The result is an increase in overall efficiency since a greater portion of the incident light is reflected into the diffraction angles of interest.

It is also sometimes useful to know the angular dispersion of the diffraction grating. If the specification of the grating is known, then it is possible to determine how close the adjacent wavelengths are in terms of angular separation. An equation for this can be found by taking the derivative of the diffraction angle in equation 4.4 with respect to a differential wavelength, and assuming the incident angle is normal to the plane of the grating, then the following equation can be used:

$$\frac{d\theta}{d\lambda} = \frac{m}{dcos\theta_r} \tag{4.7}$$

where m is the diffraction order, d is the grating period and θ_r is the diffraction angle. Equation 4.7 basically determines the angular separation between two adjacent wavelengths in a given direction. This equation can be used to determine how far the detector will need to be placed in order to achieve a certain spectral resolution. Conversely, it determines the minimum detector size if the distance is fixed. Similarly, from equation 4.4, it is possible to formulate a relationship between changes in diffraction angles with respect to changes in grating period, as long as it is in the region of small angles [39]:

$$\Delta\theta \cong \frac{m\lambda\Delta d}{d^2} \tag{4.8}$$

4.2 Diffraction Grating Design

Due to the microscopic nature of MEMS, MEMS based devices are highly suitable for these diffraction elements. From equation 4.4, it can be seen that minute changes, such as in the grating period, can greatly affect the wavelength that the device is tuned for. By taking advantage of the micro-scale precision and actuation that MEMS devices can offer, some diffraction grating devices can be made that might otherwise be very difficult to produce in the macro-scale world. This section discusses a possible MEMS diffraction grating design.

4.2.1 Numerical Computations

4.2.1.1 Sample Beam Calculation

For simulating the deflection of the MEMS grating, ANSYS will be used. However, in order to ensure that the simulation results given by ANSYS are acceptable, test calculations were performed to confirm their results. This should always be done to ensure that the parameters and assumptions used for the simulation are adequate. One of the test calculations is of a beam fixed at one end with a point load at the other end in a direction perpendicular to the structure. This is illustrated in figure 4.3. This type of structure has been previously solved and discussed

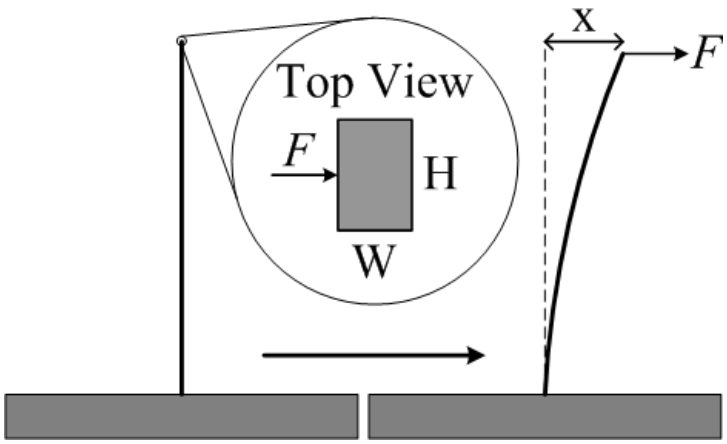

Figure 4.3: Fixed beam with perpendicular point force F to yield a displacement x in the direction of the force.

numerous times, such as in [78], and the deflection of the structure as illustrated can be determined by equation 4.9:

$$x = \frac{FL^3}{3EI} \tag{4.9}$$

where x is the deflection, F is the point force, L is the length of the beam, E is Young's modulus, and I is the moment of inertia. The moment of inertia for this case is:

$$I = \frac{HW^3}{12}$$

Thus, assuming a height, or thickness in this case, and width of 2 μm, a length of 200 μm, a value of 158×10^9 Pa for Young's modulus and 0.22 as Poisson's ratio as listed by the PolyMUMPs design handbook [79], and a test force of 1 μN, these values will yield:

$$I = \frac{2(2)^3}{12}$$
$$I = 1.333$$
$$x = \frac{1\times10^{-6}(200)^3}{3(158\times10^3)(1.333)}$$
$$x = 12.66\mu m$$

In ANSYS, the 2D Beam elastic element (BEAM3) is used. It has 3 degrees of freedom, translations in the X and Y direction, and rotation about the Z axis. To ensure that the element is a reasonable approximation of the polysilicon material used in the PolyMUMPs process, the same structure and force is simulated. The result is shown in figure 4.4. With both results being essentially identical to each other, yielding a displacement of 12.66 μm, it is therefore safe to assume that the element BEAM3 accurately models the material in mind.

4.2.1.2 Diffraction Grating Calculations

The grating design will first begin by determining the range of wavelengths the device should be capable of processing. Since the device should be able to manage fluorescent dyes that would otherwise be detected by the naked eye, it has been determined that the wavelengths of interest will span the visible spectrum. This

Figure 4.4: Fixed beam with perpendicular point force of 1 μN to yield a displacement of 12.66 μm in the direction of the force.

will also meet the spectral requirements of the APD being used. That means the range of wavelengths will span from blue to deep red, which correspond to wavelengths of 470 to 700 nm respectively. Thus, assuming an incident angle of 0° and a range of wavelengths of 470 to 700 nm, one can use equation 4.4 to determine the diffracted angle. One other parameter that must also be determined is the grating period d. Because the minimum feature size for the PolyMUMPs process is 2 μm, the grating period must be at least 4 μm. The PolyMUMPs process is chosen since it is a well established platform in which MEMS devices are fabricated. Using these

parameters, the following sets of values for each order are calculated:

Wavelength (nm)	Order				
	1	2	3	4	5
470	6.75°	13.59°	20.64°	28.03°	35.98°
520	7.40°	14.92°	22.72°	31.00°	40.07°
570	8.19°	16.56°	25.31°	34.75°	45.44°
700	10.08°	20.49°	31.67°	44.43°	61.04°

Table 4.1: Computed angles of diffraction at 0° incident angle for their respective orders. It is evident that higher orders will be vulnerable of overlapping with other orders.

From table 4.1, another important drawback to operating at higher orders appears. In addition to having lower optical power, it is noticeable that the higher orders will overlap with each other. The table shows that the blue wavelengths from order 4 will overlap with the deep red wavelengths from order 3. That means higher orders should not be used when trying to separate the wavelengths into their constituent parts or there will be a risk of diverting more than one wavelength into a certain diffraction angle. Although one can technically employ secondary filters behind the first to further separate the wavelengths, that solution is too complex for the purpose of this application. Minimal components are desired to keep the cost to a minimum, or one of the benefits of LOC devices is lost. One possible implementation that is suggested by the table is that wavelength tuning can be achieved by using a planar or curved detector array that can cover the range of the calculated diffraction angles, with each incremental width or arc length of the detector corresponding to a specific wavelength. However, this type of detector is not always available. If using a standard photodetector of limited dimensions, then another possible solution is to have the detector physically move laterally along a track across the entire range of angles or arc length. This type of design can become

quite complex since extra care must be taken to ensure the accurate positioning of the detector. In addition, it requires the use of several additional components, such as micro linear motors, which can be quite expensive and should be avoided to minimize the cost. Thus, if the source and the detector are to remain at a fixed position, then the only remaining option is that the grating itself must move or change. Consequently, by using the MEMS ability to actuate and deform their shapes, the diffraction grating period can be changed while keeping the other parameters constant to selectively modify the wavelength of interest. The new values are shown in table 4.2:

Wavelength (nm)	Grating Period (μm)	Beam Displacement (nm)	Order				
			1	2	3	4	5
470	4.000	0	6.75°	13.59°	20.64°	28.03°	35.98°
520	4.383	383	6.75°	13.59°	20.64°	28.03°	35.98°
570	4.851	851	6.75°	13.59°	20.64°	28.03°	35.98°
700	5.957	1957	6.75°	13.59°	20.64°	28.03°	35.98°

Table 4.2: Computed angles of diffraction at 0° incident angle for their respective orders, wavelengths and diffraction grating periods.

The table shows that at those grating periods, the corresponding wavelengths will have the same diffraction angles for each order as other wavelengths at their corresponding grating periods. This confirms the fact that in theory by changing the separation of the beams, and in effect changing the beam period, then at a fixed diffraction angle the wavelength of interest is changed. Therefore, a beam separation of up to 2 μm is required to be able to tune to the deep red wavelength of 700 nm.

Additional calculations were made to ensure that no overlaps will occur between different wavelengths at low orders for each of those diffraction grating periods. It

can be seen in table 4.3 that overlaps for each grating period starts from orders 3 and 4. However, the angular difference between 700 nm of order 2 and 470 nm of order 3 is too small to comfortably work with. Larger angular separation is desirable to minimize any possibility of overlap due to alignment errors. Consequently, order 1 will be used. The table also confirms that the diffraction angles listed in table 4.2 exist at their corresponding wavelength and grating period.

Wavelength (nm)	Grating Period (μm)	Order				
		1	2	3	4	5
470	4.383	6.16°	12.38°	18.77°	25.40°	32.42°
520	4.383	6.75°	13.59°	20.64°	28.03°	35.98°
570	4.383	7.47°	15.08°	22.96°	31.35°	40.56°
700	4.383	9.19°	18.63°	28.63°	39.70°	52.99°
470	4.851	5.56°	11.17°	16.90°	22.80°	28.98°
520	4.851	6.09°	12.26°	18.57°	25.13°	32.06°
570	4.851	6.75°	13.59°	20.64°	28.03°	35.98°
700	4.851	8.30°	16.77°	25.65°	35.25°	46.18°
470	5.957	4.52°	9.08°	13.69°	18.40°	23.23°
520	5.957	4.96°	9.96°	15.03°	20.23°	25.61°
570	5.957	5.49°	11.03°	16.68°	22.50°	28.58°
700	5.957	6.75°	13.59°	20.64°	28.03°	35.98°

Table 4.3: Computed angles of diffraction at 0° incident angle for their respective orders.

Because the area of the detector is approximately 200 μm in length, the diffraction grating needs to be of at least that length. To be on the safe side and allow for some margin of error during assembly, the length of the grid is set to 300 μm. An illustration of the main structure of the proposed diffraction grating is shown in figure 4.5. It can be seen that the diffraction grating is supported by diverging beams, which also act as the springs. The length of the vertical component of the spring beams is $L/4$, while the grating beams themselves are 300 μm as previously

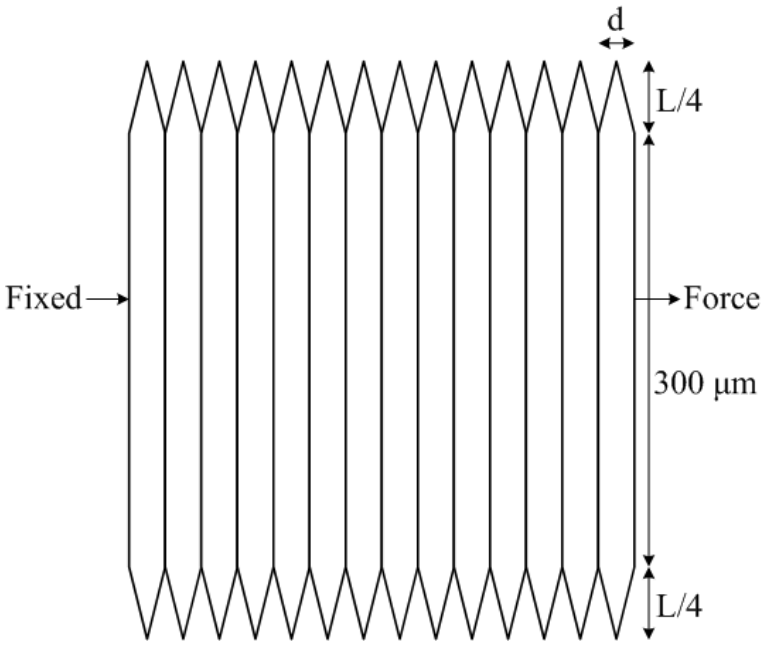

Figure 4.5: Diagram of the body of the proposed diffraction grating.

stated. Providing a horizontal force will stretch the springs and effectively change the grating period d. One end of the diffraction grating will be secured to suspend the grating as well as to ensure that the grating will only be stretched to one side. This type of spring system can be modeled as a doubly-clamped beam with a centre load. This structure is illustrated in figure 4.6, where both ends of the beam are fixed. In the textbook "Microsystem Design" by Senturia [78], an equation for such a structure is derived. Equation 10.62 of [78] is the general equation describing the properties of the doubly-clamped spring, and for this case the equation is:

$$F = C_b \left[\frac{EHW^3}{L^3}\right] c + C_s \left[\frac{EWH}{L^3}\right] c^3 \tag{4.10}$$

Note that the W and H have effectively been swapped since the force is now acting

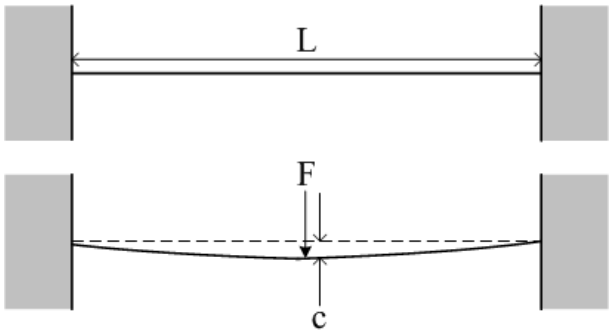

Figure 4.6: Illustration of a doubly-clamped beam with a centre load F causing a deflection c. The length of the spring in this case is the entire beam, and is of length L.

along the W direction instead of the H direction. In the equation, F is the force required, C_b and C_s are numerical constants that may need to be obtained from simulations, L is the total length of the flexures, and c is the deflection. This type of model can be used for the proposed diffraction grating body because the end points located at the mass can be considered to be fixed points. Thus, it is in theory possible to rotate the beam out of plane by 180° to form a longer flexure such that it is of the form shown in figure 4.6. This concept, as described in [78] by Senturia, is illustrated in figure 4.7. Since the support beams connected to the diffraction grating beams are all fixed to each other, and because there is no pivoting allowed due to how the device will be fabricated, the springs in the diffraction grating can employ the same technique to change into a doubly-clamped structure. This approximation by beam swivelling is allowed since deformations in beams parallel to the force, such as along the horizontal beams marked as x, is minimal when compared to beams perpendicular to the force. In other words, the bulk of the deflections will occur in a direction perpendicular to the structure if it is sufficiently thin. This is quite intuitive since the thickness of the material under

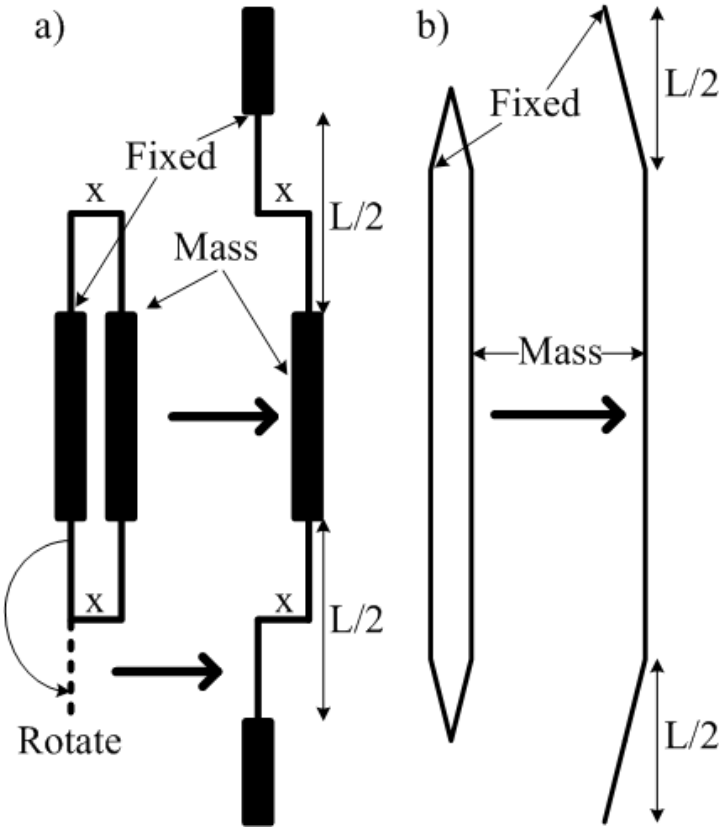

Figure 4.7: (a) Illustration of a doubly-clamped structure with masses at the centre. It can be changed into a doubly-clamped spring format by rotating the set of beams connected to the same mass outwards, as described by Senturia. (b) Illustration of the same concept, but applied to the proposed diffraction grating.

pressure is significantly greater if acting along the beams labelled as x. There will be considerably less resistance if there are fewer materials to act against the force. The reason why the lengths of the springs or support beams were labeled as $L/4$ in figure 4.5 is also apparent now. Because the length has effectively doubled after rotating the second set of beams on both sides of the mass, the flexure length on each side is now $L/2$. Adding the beams on both sides will yield an overall flexure or spring length of L, which can now be directly applied to equation 4.10. Another

advantage of the equation is that it directly determines the relative deflection per unit grating period. Adding additional gratings will not change the calculated force required to achieve a specific grating displacement or period. This is because for each grating that is added, it is effectively adding another spring. The end result is that applying the same force to the longer spring or diffraction grating will produce a greater overall displacement, but will still yield the same deflection per unit grating period. As a result, the calculations and the design of the grating are considerably simplified.

It was previously mentioned that the numerical constants C_b and C_s in equation 4.10 will need to be determined from simulations. Consequently, several simulations of the diffraction grating under different loads and grating thicknesses were performed to obtain the coefficients. The results of the simulations are summarized in table 4.4, where c is the deflection in μm, and H is the thickness of the material. Since PolyMUMPs have thicknesses of 2 and 1.5 μm for Poly 1 and Poly 2 respectively, then the maximum achievable thickness using only those two layers is 3.5 μm. This does not take into consideration of using oxide layers and Poly 0 to further increase the thickness, but that is not required since these are only initial values. Adjustments can be made in the future after the gratings have been fabricated and tested.

It can be seen that the C_s term depends heavily on the deflection c by a power of three, and increases at a much faster rate than the C_b term as the magnitude of the deflection becomes comparable to the material thickness. In addition, it is interesting to note that the C_b term increases at the same rate as the applied force. For example, when the applied force is doubled and tripled, the C_b term is also respectively doubled and tripled. Considering the fact that the C_s term increases at a much faster rate, yet this proportional relationship between C_b and the ap-

Applied Force (μN)	H = 2 μm			H = 3.5 μm		
	c	EHW^3c/L^3	$EHWc^3/L^3$	c	EHW^3c/L^3	$EHWc^3/L^3$
2	0.0990	0.0313	7.68×10^{-5}	0.0566	0.0313	2.51×10^{-5}
4	0.1981	0.0626	6.14×10^{-4}	0.1132	0.0626	2.00×10^{-4}
6	0.2972	0.0939	2.07×10^{-3}	0.1698	0.0939	6.77×10^{-4}
8	0.3962	0.1252	4.91×10^{-3}	0.2264	0.1252	1.60×10^{-3}
10	0.4952	0.1565	9.60×10^{-3}	0.2830	0.1565	3.13×10^{-3}

Table 4.4: Summary of deflection values c, and C_b and C_s terms obtained from simulations in ANSYS for different loads and material thicknesses when L=200 μm.

plied force must be maintained, it is suspected that the value of $C_s = 0$. Solving these systems of equations in MATLAB confirms this suspicion, yielding values of $C_b \approx 64$ and $C_s \approx 0$. Therefore, equation 4.10 now becomes:

$$F \approx 64 \left[\frac{EHW^3}{L^3} \right] c \tag{4.11}$$

which is of the form of the more commonly known spring equation:

$$F = kx$$

In a paper by Shih *et al.* [80] with a similar diffraction grating and springs, they determined that their spring constant can be estimated by:

$$k_f = \frac{8EHW^3}{L_f^3}$$

However, in their case, the length L_f is equal to the total length of the beam of only one side. Consequently, one must set $L = 2 \times L_f$ to consider the total length of the beam or spring. In fact, plugging $L = 2 \times L_f$ into equation 4.11 that was

previously derived will yield their spring constant. This further verifies that the values $C_b \approx 64$ and $C_s \approx 0$ are valid. Therefore, the forces that are required to achieve the desired grating periods are calculated and shown in table 4.5.

Grating Period (μm)	Beam Displacement (μm)	Force Required (μN)
4.000	0.000	0.00
4.383	0.383	13.55
4.851	0.851	30.12
5.957	1.957	69.26

Table 4.5: Forces needed to attain the necessary beam displacements. The parameters used are $E = 158GPa$, $H = 3.5\mu m$, $W = 2\mu m$, and $L = 200\mu m$.

From the table, it is clear that a force of up to 70 μN is required.

Because one of the most common forms of MEMS actuation is the comb drive, and it is a proven actuator, the diffraction grating is to be actuated by a comb drive. Ignoring any edge effects, such as fringe effects, the force provided by a comb drive can be approximated by [80]:

$$F = \frac{N\varepsilon H}{2g}V^2 \tag{4.12}$$

where N is the number of finger pairs, ε is the permittivity of the material, which in this case is just air, g is the gap distance between the fingers, and V is the applied voltage. A sample finger pair is illustrated in figure 4.8. Note that the gap distance is set to 2 μm because the PolyMUMPs process requires a spacing of at least 2 μm between features to ensure that they are properly fabricated, meaning a total of $5 \times 2\mu m = 10\mu m$ is required for each set. This also means that the current specifications for the diffraction grating will need to be changed if the PolyMUMPs process is used. The springs illustrated in figure 4.5 have features spaced at less than 2 μm apart. As a result, a grating with springs of the form shown in figure 4.9

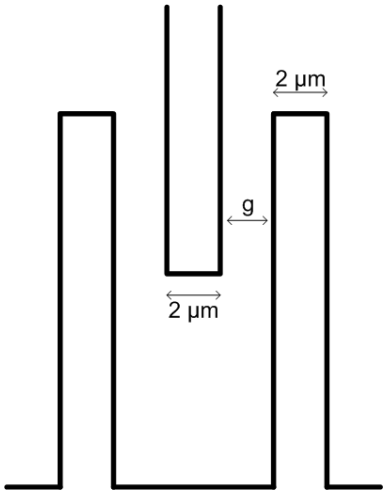

Figure 4.8: Diagram of a sample finger pair. The gap distance in this case will be g = 2 μm.

will be used. In this case, every single feature is spaced 2 μm apart to meet the

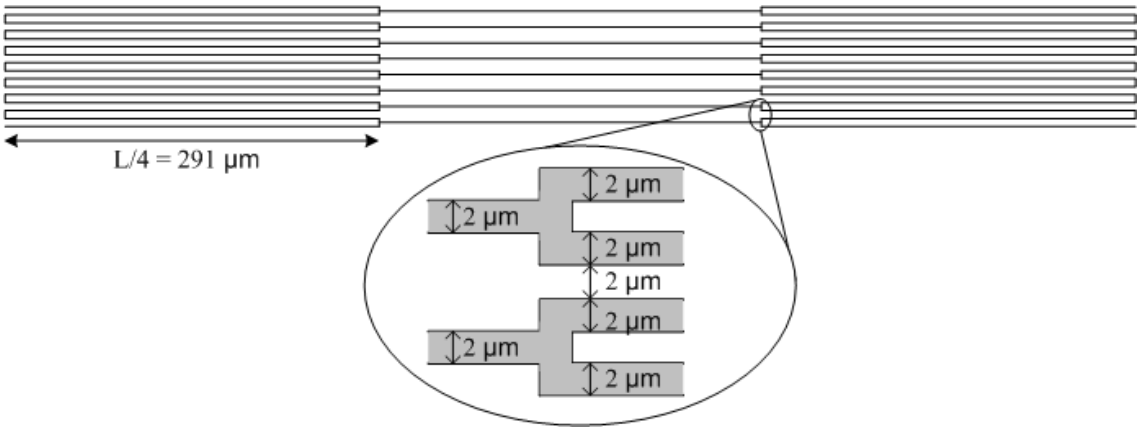

Figure 4.9: Diagram of a part of the new diffraction grating to meet PolyMUMPs' design rules.

PolyMUMPs process requirements. However, since the period is now increased to 8 μm, meaning there are now fewer gratings per unit length, the resolving power is

now halved, as determined by equation 4.6. Consequently, if a fabrication process capable of producing diffraction gratings with a period of the old value of 4 μm is available, then it should be considered to achieve higher resolving power.

It has been previously determined that a maximum of 70 μN is required. If assuming that 100 finger pairs are used, then approximately 301 V is needed for actuation. This is clearly not acceptable for a portable device. To reduce the voltage requirement, one can combine equations 4.11 and 4.12 together to solve for the required spring length L by setting a lower operating voltage:

$$L = \sqrt[3]{\frac{128EW^3cg}{N\varepsilon V^2}}$$

Using values of $E = 158GPa$, $W = 2\mu m$, $c = 3.915\mu m$, $g = 2\mu m$, $N = 70$, $\varepsilon = 8.85pF/m$, and $V = 36V$, it has been determined that the spring length needs to be 1164 μm long. The voltage has been increased to 36 V since it is reasonable and much simpler to add more 9 V batteries than to have to include more finger pairs in the MEMS design. Note that the deflection c is now 3.915 μm because the new grating period of d = 8 μm is being used instead of d = 4 μm. Therefore, with the new values of d = 8 μm, the new diffraction angle, grating deflections, and forces required are shown in table 4.6.

Wavelength (nm)	Diffraction Angle (Order 1)	Beam Displacement (μm)	Force Required (nN)
470	3.37°	0.000	0.0
520	3.37°	0.766	137.4
570	3.37°	1.702	305.4
700	3.37°	3.915	702.5

Table 4.6: Forces needed to attain the necessary beam displacements. The parameters used are $E = 158GPa$, $H = 3.5\mu m$, $W = 2\mu m$, and $L = 1164\mu m$.

4.2.2 Layout

A diagram of the layout of the proposed diffraction grating is shown in figure 4.10. The diagram is not to scale, and the comb drives have been considerably magnified for clarity. It can be seen that the Poly 0 layers are not connected to each other to allow bias to be applied across both sections. The diagram also illustrates that most of the bottom of the grating should be etched away, including Poly 0 and the nitride layer. This is to allow the light to be transmitted through the grating. Also, a metal layer is deposited on top of Poly 2 of the grating beams to help block any light transmission. The dimples are used to help prevent the grating from deforming due to its mass. It should be noted that calculations of the actuation force did not take into account of friction or stiction caused by any polysilicon in contact with each other, as well as fringe effects. As this thesis is only focused on the basic design of the grating itself, problems affecting actuation are not directly dealt with. However, if the device is fabricated and tested, and it has shown that its behaviour deviated significantly, then forces that were not previously considered should be taken into account. It can also be seen that the device is of approximately 3.5 μm in thickness by depositing Poly 2 directly on top of the Poly 1 layer, and the figure also shows that the beam width is 2 μm.

4.3 Diffraction Results

To confirm that the equations and solutions derived from previous sections are valid, several simulations in ANSYS were performed. In addition, slides containing diffraction gratings of the same dimensions as those initially calculated in the previous section were also fabricated and tested with. All of the results are discussed

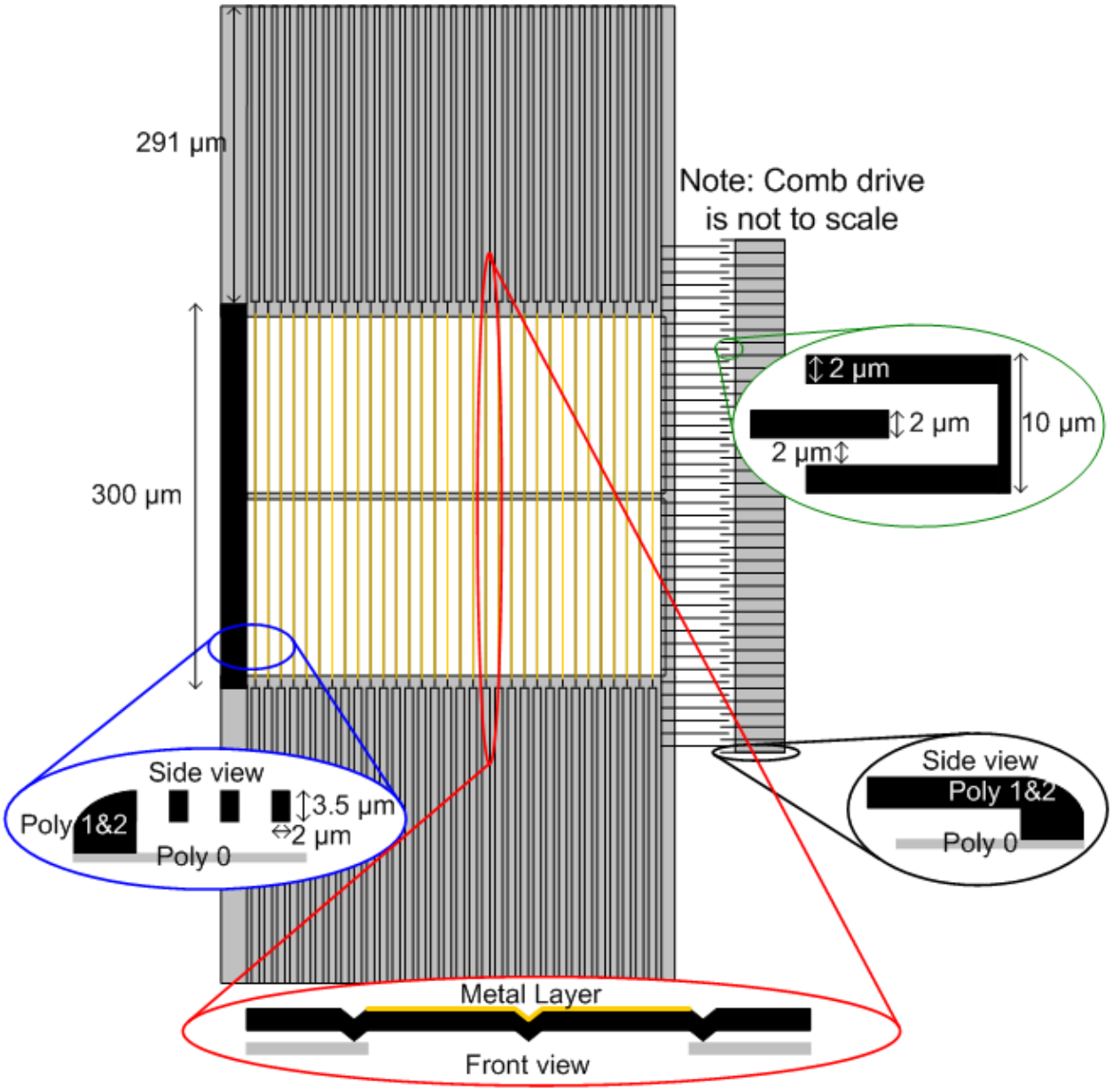

Figure 4.10: Diagram of the overall layout of the diffraction grating. Please note that the diagram is not to scale.

in this section.

4.3.1 Simulations

It has already been verified that the assumptions made regarding the polysilicon material and the beam element used (BEAM3) in ANSYS are valid. Having determined the forces required to achieve the desired diffraction grating period, these forces are applied to the model and the results are simulated. A sample simulation from ANSYS is shown in figure 4.11, where a small portion of the diffraction grating is simulated. The top side of the diffraction grating has a rectangular support structure to prevent the first few beams from bending. This is required since the force is applied as a point force at the two topmost corners. Without the support beams, then the grating will be distorted and the results would not be representative of the actual grating. In the actual design, the topmost structure will be a long array of comb drives since an actuator is needed to provide a force to move the diffraction gratings. The end result will be the same as the array will be of sufficient stiffness to prevent the initial grating beams from being distorted. In addition, the comb drive array should provide a uniform force, further reducing the chances of pulling the diffraction gratings unevenly. The simulated results are also listed in table 4.7 and compared to the desired values. The results indicate that the equations previously derived, such as equation 4.11, and the values calculated to obtain the necessary displacements are correct. The percentage errors between the simulated results and the calculated results are relatively low. All of the simulated values differ from the desired values by less than five percent, and all appear to be deforming the beam more than predicted. If this simulation holds, then that means a maximum of 36 V may not be necessary since the force required to alter

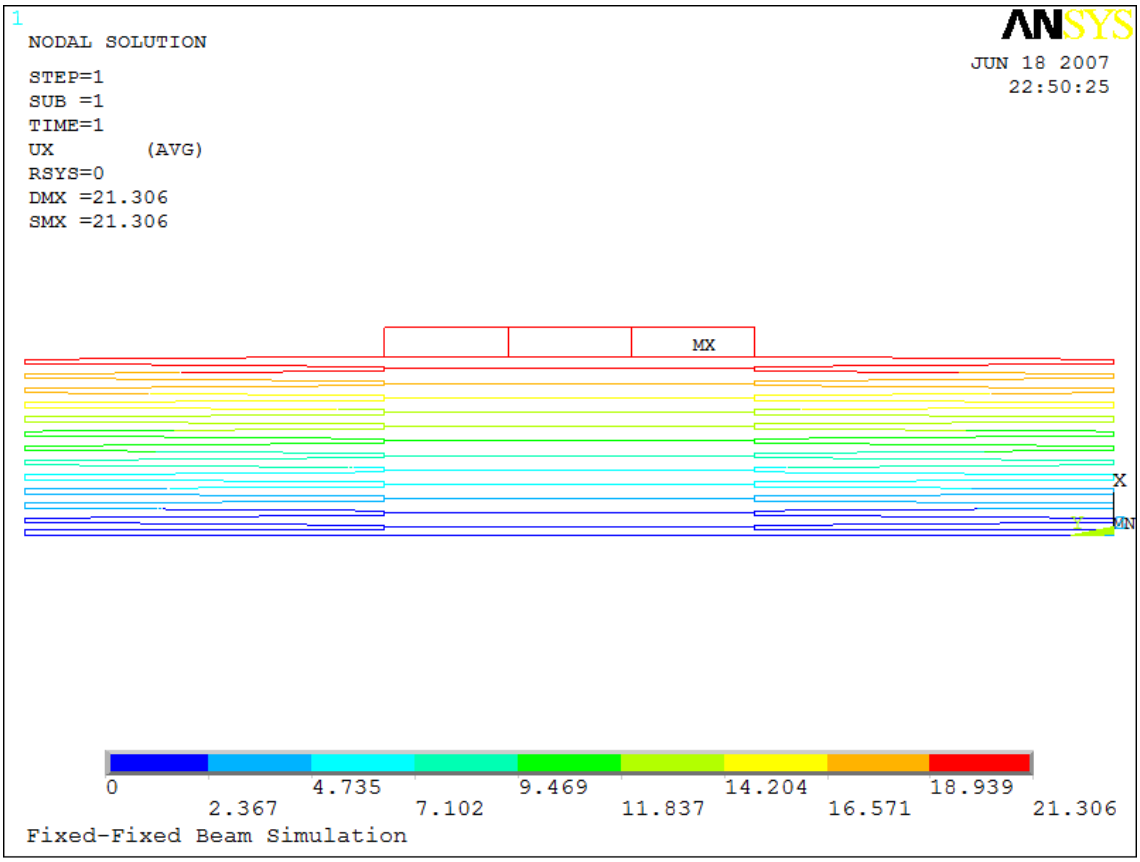

Figure 4.11: Image showing the total displacement experienced by the grating structure.

the grating is actually slightly less than originally calculated.

Force Applied (nN)	Desired Displacement (μm)	Simulated Displacement (μm)	Percentage Error
137.4	0.766	0.797	4.091%
305.4	1.702	1.772	4.087%
702.5	3.915	4.075	4.090%

Table 4.7: Simulated results from ANSYS indicating that the equations previously derived and values calculated are adequate due to the low percentage errors achieved.

4.3.2 Measurements

To help verify the calculations and simulation results, slides containing diffraction gratings of the same periods as those initially calculated in previous sections were also fabricated and tested with. Advance Reproductions Corporation was used to fabricate the grating slides. The quartz glass slides were originally coated with chrome, followed by the application of photoresist. After patterning, the photoresist was developed by e-beam lithography and the chrome was then etched. The process has an error tolerance of $\pm 0.1\ \mu m$. Seven 70 mm $\times$ 10 mm $\times$ 3 mm glass strips were fabricated, each with nine distinct chrome diffraction gratings of 5 mm $\times$ 6 mm. The properties of the gratings are listed in table 4.8 and a sample diagram provided by the fabrication company illustrating a sample slide is shown in figure 4.12.

Grating Number	Grating Period (μm)	Grating Beam Width (μm)	Grating Spacing (μm)
1	4.0	2	2.0
2	4.4	2	2.4
3	4.6	2	2.6
4	4.8	2	2.8
5	5.0	2	3.0
6	5.4	2	3.4
7	5.6	2	3.6
8	5.8	2	3.8
9	6.0	2	4.0

Table 4.8: Diffraction grating specifications for each diffraction grating in figure 4.12.

Figure 4.13 shows several magnified pictures of gratings 4 to 6. Using these diffraction gratings, diffraction angles of red light emitted from a HeNe gas laser by Uniphase (model 507-0) was measured. A laser was used due to their low beam

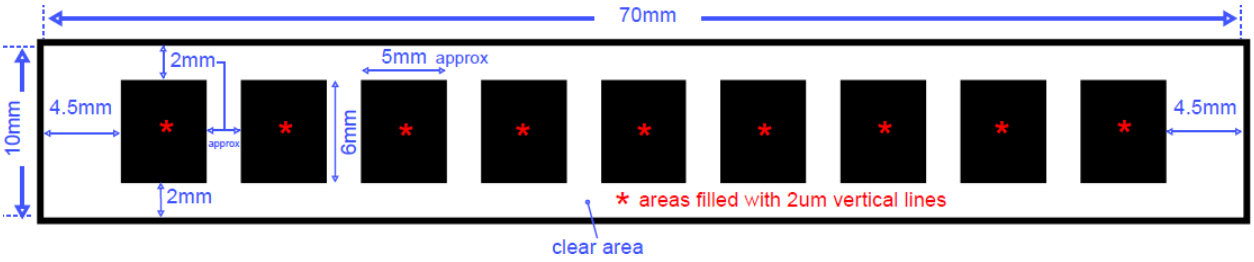

Figure 4.12: Diagram of a sample diffraction grating slide. It contains nine diffraction gratings, each with a different grating period.

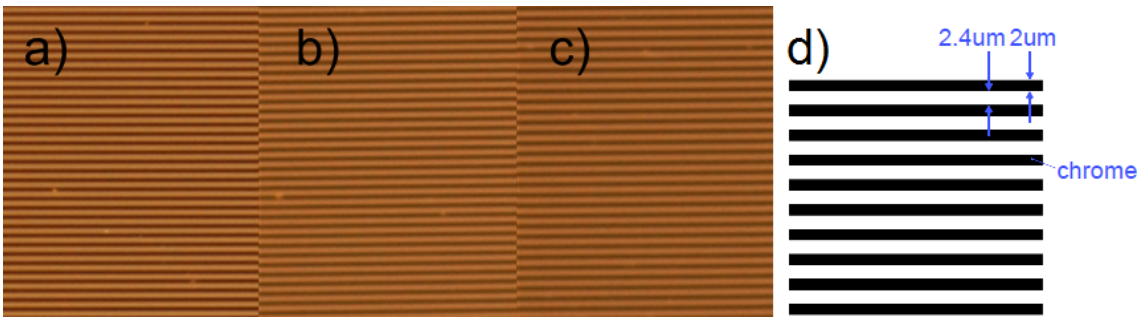

Figure 4.13: $(a)-(c)$ Images of actual chrome gratings from grids 4 to 6 respectively. Different spacings between various grids are quite evident. (d) Illustration of sample grid showing 2 μm chrome grating beam and 2.4 μm spacing to form a 4.4 μm grating period.

spreading, which is necessary for testing and calibration of diffraction gratings. This is because the incident angle is crucial in determining the diffraction angle, so having minimal beam spread is ideal. The setup used to calculate the diffraction angle is illustrated in figure 4.14 and the values are summarized in table 4.9.

The results indicate that the gratings performed as expected. This is shown in figure 4.15, where the colour separation of the three colour LED is evident. The top part of each image was taken when grid #9 was used, which is designed for the red wavelength, while the bottom part corresponds to when grid #1 is used, which

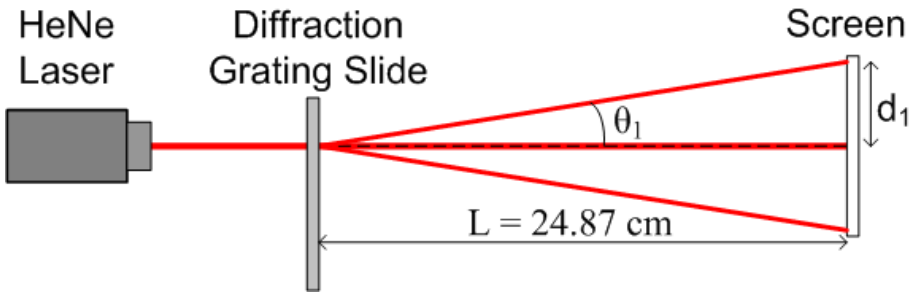

Figure 4.14: Diagram of setup used to determine diffraction angle. Using simple trigonometry, it is possible to determine the first order diffraction angle θ_1.

Grating Number	Grating Period (μm)	Diffraction Angle		Percent Error
		Calculated	Measured	
1	4.0	9.10°	9.14°	0.38%
2	4.4	8.27°	8.35°	0.97%
3	4.6	7.91°	7.78°	1.55%
4	4.8	7.58°	7.56°	-0.23%
5	5.0	7.27°	7.28°	0.06%
6	5.4	6.73°	6.88°	2.21%
7	5.6	6.49°	6.54°	0.76%
8	5.8	6.26°	6.31°	0.74%
9	6.0	6.05°	6.03°	-0.48%

Table 4.9: Calculated and measured diffraction angles based on a laser wavelength of 632.8 nm.

is designed for the blue wavelength at the same diffraction angle. It can be seen that the positions of the diffracted red wavelengths in the top images correspond to the same positions as the blue wavelengths in the bottom images. The images also indicate that colour separation is indeed achieved and that the first order has lower intensity than the zeroth order. This corroborates with the spacings calculated and equations used in previous sections. Although the images show substantial overlap between different colours, one can see that the centre of each LED colour is consid-

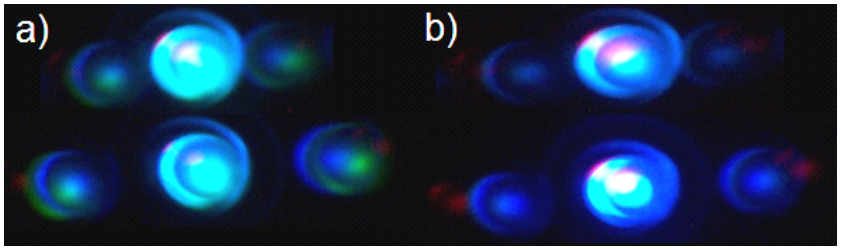

Figure 4.15: Images illustrating colour separation of (a) all three primary wavelengths and (b) blue and red wavelengths only. The zeroth and first orders are shown. Top images correspond to grid #9 while bottom images correspond to grid #1.

erably far apart from each other. The overlap currently seen is mainly due to the size of the LED; however, when working with real samples, the incident light will be focused to the size of the detector for maximum power. This will also prevent the overlapping evident in the figure.

4.4 Summary

It is shown that the concept of a MEMS diffraction grating for wavelength tuning is possible. A diffraction grating for the visible spectrum was proposed, and simulations and testing on diffraction grating slides have demonstrated that it has great promise. The grating slides were fabricated using specifications identical to the original specifications of the MEMS diffraction grating where possible. Therefore, the chrome lines are also of 2 μm wide, and grating periods of 4, 4.4, 4.8, and 6 μm were patterned on the slide, as well as gratings with other periods in between. Grating periods of 4 μm were used to achieve higher resolving power since there were no springs to fabricate. As previously mentioned, if a fabrication process that can produce springs shown in figure 4.5 is available, then they should be consid-

ered. Thus it is shown that this idea should be further investigated since adding the wavelength tuning capability to an LOC device will significantly increase its capability.

Chapter 5

Conclusions and Future Work

This chapter summarizes the main points and results obtained from chapters 3 and 4. The limitations and errors are discussed. Possible extensions or additions to the device in terms of future work will be suggested as well.

5.1 Summary

Chapter 2 gave an overview of the various studies on fluorescence detection systems. From fluorescence setups for microfluidic applications to handheld PCR analysers, several different devices and setups were described. From the results of their studies, it is clear that it is possible to integrate semiconductor based optoelectronic components such as laser diodes, LEDs, and detectors such as PMTs, APDs and photon counters to build their own fluorescence systems. The main drawback with most of their proposed devices is that they are targeting for specific applications, such as PCR and chlorophyll analysis, so their instruments are permanently de-

signed for those applications. Although that is fine for their research, the goal of this thesis is to provide a general fluorescence system capable of many different applications or be easily modified to be able to execute them. In addition, there are cases where their proposed devices are not truly self-sufficient, whereby they had a need of external processing and display systems such as a computer. This defeats the purpose of a LOC device since one of their main features is their portability such that they can be used on-site.

Chapter 3 discussed the background theories of the main components used as well as reasons why they were chosen. It has been shown in the chapter that it is possible to use LEDs as excitation sources, thereby confirming the results reported by other groups. In addition, it is shown that a photoresistor can be used as a fluorescence detector, which is an application of the photoresistor that has not been rigorously studied by other groups. The reason is that most of their detectors are based on APD technology. Consequently, an APD based device was also implemented and the results from both the photoresistor and APD based device show promise since their measurements were similar to the results obtained by commercial analysers. The inner-filter effect was also clearly demonstrated, further verifying the results previously reported by others.

Chapter 4 discussed the background theories of diffraction and related physics. It has been shown in the chapter that the concept of using a diffraction grating for wavelength tuning is possible, thereby confirming the results reported by other groups. Simulation results from ANSYS as well as actual diffraction pattern measurements from slides fabricated with similar grating properties were used to support the calculations and design.

5.2 Contributions

This thesis contributes to the field of fluorescence detection system for LOC devices by furthering their research and implementing a completely self-sufficient system. It is shown that it is possible to use photoresistors and APDs as cost-effective fluorescence detectors for LOC devices. As well, a microcontroller is used for processing and output display, demonstrating that low cost components can be used instead of the more expensive computer processors. Therefore, it is shown that with all of these low powered, low cost components, it is still possible to design a usable fluorescence detection system for a LOC device. The thesis also contributes by proposing a MEMS diffraction grating that can be implemented for wavelength tuning. This will greatly enhance the versatility of optical based LOC devices. It is shown that diffraction gratings with grating beam widths and periods determined in this thesis can be used for colour separation. Therefore, it is demonstrated that the concept of a MEMS diffraction grating to be used in devices such as LOC for wavelength tuning is feasible.

5.3 Limitations of the Research

Although the results measured by the photoresistor and APD device follow closely with the measurements provided by retail fluorometers, there were still noticeable differences. One of the main problems is due to contamination. Since different equipment require different cuvettes or sample holders, it is not possible to accurately measure the same sample without transferring from one holder to another, thus there will always be a chance of cross contamination. Until both devices accept samples in the same format, there will always be a possibility of contamination with

the movement of samples. Another problem is that fluorophores are susceptible to photobleaching. It was not previously mentioned, but when fluorescent dyes are exposed to excitation light, they will eventually lose their ability to fluoresce. The emission intensity decreases over time as the fluorophores are destroyed by the high powered incident light. Consequently, taking measurements over a long period of time will yield a lower reading than when the samples were first tested. Thus far this did not pose a problem since there were little to no fluctuations when reading the samples, but once the samples start to degrade, a new batch will need to be made. With a new batch, all of the measurements will need to be repeated again since the concentration may not be exactly the same as the original sample. This leads to the third problem, which is that when samples were created, not all "identical" concentrations may be exactly the same. This is due to the extremely low concentrations used, so measurement errors made during sample preparation can become quite significant. Thus, to minimize the effects of this error, it is best to reuse the same sample instead of constantly making new batches since new ones may contain a different concentration.

Because an actual MEMS diffraction grating was not fabricated in time and tested, no true confirmation of the values calculated and of the design can be made with confidence. Although results highly suggest that the design is feasible, and compared to designs and results reported by other groups, the values obtained seem reasonable, actual testing is required. In addition, effects such as fringe effects and stiction were ignored in the design of the grating as a first design. Once testing is performed, the design can be further refined. It can also be noticed that one major limitation of the grating is the operating voltage required. Because the device needs to be portable, drastically high voltages are prohibited. Possible alternatives can include adding a tilting capability to the MEMS diffraction grating, such as

those used for MEMS micromirrors. Being able to tilt can be beneficial since the diffraction angle is also dependent on the incident angle. Thus, it may be possible to achieve the same overall diffraction angle without having to change the grating period by up to 2 μm by simply tilting the grating. If a considerable amount of grating deflection is required, then another possibility is to use something similar to the rhomboid heatuators proposed by Zhang *et al.* [41]. It was capable of achieving a 5 μm deflection, which is more than twice the amount required for the proposed diffraction grating.

5.4 Future Work

Because the current being measured from the APD is in the nanoamperes range, introductions of low level noise can still become quite significant. Consequently, a noise cancelling circuit should be investigated and implemented in the near future. One possibility is to build something in the form of figure 5.1 as suggested by [81]. In this setup, APD#1 is exposed to the incident light while APD#2 is kept in the dark. If both APDs are identical in terms of performance, then any noise detected by APD#1, such as due to environmental EM excitation, may also be detected by APD#2. The result is that both should produce the same noise signature. Thus, in a differential op-amp configuration, the noise from APD#2 is subtracted from APD#1 to yield a cleaner signal overall. Both feedback resistors should also be identical to ensure the same noise gain is being cancelled. Another feature that would be greatly useful is the ability for the device to store data and transmit them wirelessly. Although it can currently be used on-site, being able to store measurement data points can help make the device more useful. In addition, having

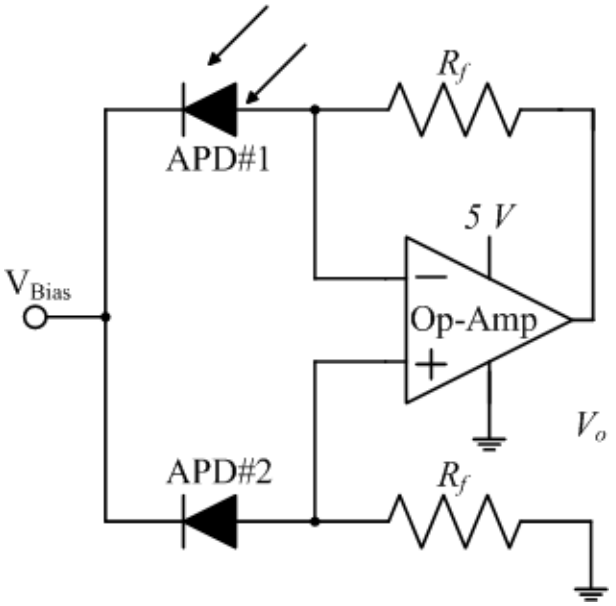

Figure 5.1: Using differential configuration to cancel APD noise.

an electronic version of the data can allow for complex data processing techniques to be performed. With the use of a microcontroller, some of these processing techniques can be performed directly on the device. The wireless feature will also help make the device easier to use. Applications can include implementing the system on a remote sensor to monitor areas not easily accessible or to work with another LOC device that is performing another set of tests to develop a general conclusion. This feature can be important since the device is designed to be simple, yet easily modified. As a result, there could be several variations of these devices, each only responsible for one of several tests that may need to be performed. With each device executing their own tasks, the results can then be sent to each other to yield an overall result.

If the MEMS diffraction grating is fabricated and tested, then the design should be further refined. In addition, concepts such as adding a tilting capability or

designing an actuator that can allow for greater deflection with low power should be considered. A comb drive actuator was chosen since it is a proven concept. However, it is only capable of electrostatic attraction, whereas other actuators, such as magnetic actuation, can be capable of both repulsion and attraction. Being able to perform both may be able to improve the performance of the actuators. Consequently, they are also good candidates for future work. A way to integrate diffraction gratings into materials such as PDMS should also be investigated, since that will greatly benefit microfluidic devices. Clearly, the possibilities associated with MEMS diffraction gratings are numerous, with many opportunities available for future work.

Bibliography

[1] L. Novak, P. Neuzil, J. Pipper, Y. Zhang, and S. Lee. An integrated fluorescence detection system for lab-on-a-chip applications. *Lab. Chip*, 7:27–29, 2007.

[2] P. Belgrader, S. Young, B. Yuan, M. Primeau, L. A. Christel, F. Pourahmadi, and M. A. Northrup. A battery-powered notebook thermal cycler for rapid multiplex real-time pcr analysis. *Anal. Chem.*, 73(2):286–289, 2001.

[3] J. D. Yantzi and J. T.W. Yeow. Carbon nanotube enhanced pulsed electric field electroporation for biomedical applications. In *Proceedings of the IEEE International Conference on Mechatronics and Automation*, volume 4, pages 1872–1877, 2005.

[4] S. Brenner, M. Johnson, J. Bridgham, G. Golda, D. H. Lloyd, D. Johnson, S. Luo, S. McCurdy, M. Foy, M. Ewan, R. Roth, D. George, S. Eletr, G. Albrecht, E. Vermaas, S. R. Williams, K. Moon, T. Burcham, M. Pallas, R. B. DuBridge, J. Kirchner, K. Fearon, J.-I Mao, and K. Corcoran. Gene expression analysis by massively parallel signature sequencing (mpss) on microbead arrays. *Nature Biotechnology*, 18:630–634, 2000.

[5] Q. Yan, R. S. Chen, and J.-K. Cheng. Highly sensitive fluorescence detection with hg-lamp and photon counter in microchip capillary electrophoresis. *Anal. Chim. Acta*, 555(2):246–249, 2006.

[6] P. K. Dasgupta, I.-Y. Eom, K. J. Morris, and J. Li. Light emitting diode-based detectors: Absorbance, fluorescence and spectroelectrochemical measurements in a planar flow-through cell. *Anal. Chim. Acta*, 500(1):337–364, 2003.

[7] J. S. Kuo, C. L. Kuyper, P. B. Allen, G. S. Fiorini, and D. T. Chiu. High-power blue/uv light-emitting diodes as excitation sources for sensitive detection. *Electrophoresis*, 25:3796–3804, 2004.

[8] C. Sakamoto, N. Yamaguchi, and M. Nasu. Rapid and simple quantification of bacterial cells by using a microfluidic device. *App. and Env. Micro.*, 71(2):1117–1121, 2005.

[9] A. Dodabalapur, L. J. Rothberg, R. H. Jordan, T. M. Miller, R. E. Slusher, and J. M. Phillips. Physics and applications of organic microcavity light emitting diodes. *J. Appl. Phys.*, 80(12):6954–6964, 1996.

[10] Y.-A. Chen, B.-F. Chen, W.-C. Tsay, L.-H. Laih, M.-N. Chang, J.-I. Chyi, J.-W. Hong, and C.-Y. Chang. Porous silicon light-emitting diode with tunable color. *Solid-State Electronics*, 41(5):757–759, 1997.

[11] A. Guttman. High-performance ultrathin layer agarose gel electrophoresis. *Trends in Anal. Chem.*, 18(11):694–702, 1999.

[12] Y. Guo, K. Uchiyama, T. Nakagama, T. Shimosaka, and T. Hobo. An integrated microfluidic device in polyester for electrophoretic analysis of amino acids. *Electrophoresis*, 26:1843–1848, 2005.

[13] R. Irawan, T. S. Chuan, and F. C. Yaw. Integration of a fluorescence detection system and a laminate-based disposable microfluidic chip. *Microwave Opt. Tech. Letters*, 45(5):456–460, 2005.

[14] K. Schult, A. Katerkamp, D. Trau, F. Grawe, K. Cammann, and M. Meusel. Disposable optical sensor chip for medical diagnostics: New ways in bioanalysis. *Anal. Chem.*, 71(23):5430–5435, 1999.

[15] A. Barócsi, L. Kocsányi, S. Várkonyi, P. Richter, Z. Csintalan, and K. Szente. Two-wavelength, multipurpose, truly portable chlorophyll fluorometer and its application in field monitoring of phytoremediation. *Meas. Sci. Technol.*, 11:717–729, 2000.

[16] T. D. Lacoste, X. Michalet, F. Pinaud, D. S. Chemla, A. P. Alivisatos, and S. Weiss. Ultrahigh-resolution multicolor colocalization of single fluorescent probes. *Biophys.*, 97(17):9461–9466, 2000.

[17] G. Ocvirk, H. Salimi-Moosavi, R. J. Szarka, E. A. Arriaga, P. E. Andersson, R. Smith, N. J. Dovichi, and D. J. Harrison. Beta-galactosidase assays of single-cell lysates on a microchip: A complementary method for enzymatic analysis of single cells. In *Proceedings of the IEEE*, volume 92, pages 115–125, 2004.

[18] J. A. Higgins, S. Nasarabadi, J. S. Karns, D. R. Shelton, M. Cooper, A. Gbakima, and R. P. Koopman. A handheld real time thermal cycler for bacterial pathogen detection. *Biosen. Bioelec.*, 18:1115–1123, 2003.

[19] E. T. Lagally, J. R. Scherer, R. G. Blazej, N. M. Toriello, B. A. Diep, M. Ramchandani, G. F. Sensabaugh, L. W. Riley, and R. A. Mathies. Integrated portable genetic analysis microsystem for pathogen/infectious disease detection. *Anal. Chem.*, 76(11):3162–3170, 2004.

[20] N. C. Cady, S. Stelick, M. V. Kunnavakkam, Y. Liu, and C. A. Batt. A microchip-based dna purification and real-time pcr biosensor for bacterial detection. In *Proceedings of the IEEE Sensors*, volume 3, pages 1191–1194, 2004.

[21] J. M. K. Ng, I. Gitlin, A. D. Stroock, and G. M. Whitesides. Components for integrated poly(dimethylsiloxane) microfluidic systems. *Electrophoresis*, 23:3461–3473, 2002.

[22] N. Pamme, R. Koyama, and A. Manz. Counting and sizing of particles and particle agglomerates in a microfluidic device using laser light scattering: application to a particle-enhanced immunoassay. *Lab. Chip*, 3:187–192, 2003.

[23] A. Wolff, I. R. Perch-Nielsen, U. D. Larsen, P. Friis, G. Goranovic, C. R. Poulsen, J. P. Kutter, and P. Telleman. Integrating advanced functionality in a microfabricated high-throughput fluorescent-activated cell sorter. *Lab. Chip*, 3:22–27, 2003.

[24] L.-M. Fu and C.-H. Lin. High-resolution dna separation in microcapillary electrophoresis chips utilizing double-l injection techniques. *Electrophoresis*, 25:3652–3659, 2004.

[25] Z. Wang, J. El-Ali, M. Engelund, T. Gotsaed, I. R. Perch-Nielsen, K. B. Mogensen, D. Snakenborg, J. P. Kutter, and A. Wolff. Measurements of scattered light on a microchip flow cytometer with integrated polymer based optical elements. *Lab. Chip*, 4:372–377, 2004.

[26] J. Kruger, K. Singh, A. O'Neill, C. Jackson, A. Morrison, and P. O'Brien. Development of a microfluidic device for fluorescence activated cell sorting. *J. Micromech. Microeng.*, 12:486–494, 2002.

[27] V. P. Iordanov, B. P. Iliev, A. Bossche, J. Bastemeijer, P. M. Sarro, I. T. Young, G. W. K. van Dedem, and M. J. Vellekoop. Integrated sensor arrays

for bioluminescence and fluorescence bio-chemical analysis. In *Proceedings of the IEEE Sensors*, volume 2, pages 810–813, 2004.

[28] P. Y. Chiou, M. C. Wu, H. Moon, C.-J. Kim, and H. Toshiyoshi. Optical actuation of microfluidics based on opto-electrowetting. In *Proceedings of the Solid-State Sensor, Actuator and Microsystems Workshop*, pages 269–272, 2002.

[29] F. Fixe, V. Chu, D. M. F. Prazeres, and J. P. Conde. An on-chip thin film photodetector for the quantification of dna probes and targets in microarrays. *Nucleic Acids Research*, 32(9):e70, 2004.

[30] Y. Takabayashi, M. Uemoto, K. Aoki, T. Odake, and T. Korenaga. Development and optimization of a lab-on-a-chip device for the measurement of trace nitrogen dioxide gas in the atmosphere. 131:573–578, 2006.

[31] C. Estes, A. Duncan, B. Wade, C. Lloyd, W. Ellis Jr., and L. Powers. Reagentless detection of microorganisms by intrinsic fluorescence. *Biosen. Bioelec.*, 18:511–519, 2003.

[32] H.-Y. Kim, C. R. Estes, A. G. Duncan, B. D. Wade, F. C. Cleary, C. R. Lloyd, W. R. Ellis Jr., and L. S. Powers. Real-time detection of microbial contamination. *IEEE Eng. Med. Bio. Magazine*, 23(1):122–129, 2004.

[33] J. A. Chediak, Z. Luo, J. Seo, N. Cheung, L. P. Lee, and T. D. Sands. Hybrid integration of cds filters with gan leds for biophotonic chips. In *Proceedings of the 16th IEEE International Conference on MEMS*, pages 323–326, 2003.

[34] J. A. Chediak, Z. Luo, J. Seo, N. Cheung, L. P. Lee, and T. D. Sands. Heterogeneous integration of cds filters with gan leds for fluorescence detection microsystems. *Sens. Actuators A*, 111(1):1–7, 2004.

[35] V. Namasivayam, R. Lin, B. Johnson, S. Brahmasandra, Z. Razzacki, D. T. Burke, and M. A. Burns. Advances in on-chip photodetection for applications in miniaturized genetic analysis systems. *J. Micromech. Microeng.*, 14:81–90, 2004.

[36] D.E. Nivens, T.E. McKnight, S.A. Moser, S.J. Osbourn, M.L. Simpson, and G.S. Sayler. Bioluminescent bioreporter integrated circuits: potentially small, rugged and inexpensive whole-cell biosensors for remote environmental monitoring. *J. Appl. Microbiology*, 96(1):33–46, 2004.

[37] H. Schaefer, K. Seibel, M. Walder, L. Schoeler, T. Pletzer, M. Waidelich, H. Ihmels, D. Ehrhardt, and M. Boehm. Monolithic integrated optical detection for microfluidic systems using thin film photodiodes based on amorphous silicon. In *Proceedings of the 18th IEEE International Conference on MEMS*, pages 758–761, 2005.

[38] A. Piruska, I. Nikcevic, S. H. Lee, C. Ahn, W. R. Heineman, P. A. Limbach, and C. J. Seliskar. The autofluorescence of plastic materials and chips measured under laser irradiation. *Lab. Chip*, 5:1348–1354, 2005.

[39] C. W. Wong, Y. Jeon, G. Barbastathis, and S.-G. Kim. Analog piezoelectric-driven tunable gratings with nanometer resolution. *J. Microelectromech. Sys.*, 13(6):998–1005, 2004.

[40] W.-C. Shih, C. Hidrovo, S.-G. Kim, and G. Barbastathis. Optical diversity by nanoscale actuation. *IEEE Conf. NANO '03*, 2:892–895, 2003.

[41] X. M. Zhang and A. Q. Liu. A mems pitch-tunable grating add/drop multiplexers. *IEEE Conf. Opt. MEMS '00*, pages 25–26, 2000.

[42] D. M. Burns and V. M. Bright. Development of microelectromechanical variable blaze gratings. *Sens. Actuators A*, 64(1):7–15, 1998.

[43] X. Li, C. Antoine, D. Lee, J.-S. Wang, and O. Solgaard. Tunable blazed gratings. *J. Microelectromech. Sys.*, 15(3):597–604, 2006.

[44] M.-H. Kiang, J. T. Nee, K. Y. Lau, and R. S. Muller. Surface-micromachined diffraction gratings for scanning spectroscopic applications. *Solid State Sens. Actuators Transducers '97*, 1:343–345, 97.

[45] A. A. Yasseen, S. W. Smith, F. L. Merat, and M. Mehregany. Diffraction grating scanners using polysilicon micromotors. *IEEE J. Selected Topics in Quantum Elect.*, 5(1):75–82, 1999.

[46] D. M. Bloom. The grating light valve: revolutionizing display technology. http://www.siliconlight.com.

[47] G. B. Hocker, D. Youngner, E. Deutsch, A. Volpicelli, S. Senturia, M. Butler, M. Sinclair, T. Plowman, and A. J. Ricco. The polychromator: A programmable mems diffraction grating for synthetic spectra. In *Proc. Tech. Digest of Solid-State Sensors and Actuators Workshop*, pages 89–92, 2000.

[48] Y.-C. Tung and K. Kurabayashi. Nanoimprinted strain-controlled elastomeric gratings for optical wavelength tuning. *Appl. Phys. Lett.*, 86, 2005.

[49] S.-H. Kong, G. de Graat, and R. F. Wolffenbuttel. Spectral performance of a silicon ir microspectrometer. *Solid State Sens. Actuators Tranducers '03*, 2:1610–1613, 2003.

[50] T. A. Kwa and R. F. Wolffenbuttel. Integrated grating/detector array fabricated in silicon using micromachining techniques. *Sens. Actuators A*, 31(1):259–266, 1992.

[51] J. Mohr, B. Anderer, and W. Ehrfeld. Fabrication of a planar grating spectrograph by deep-etch lithography with synchrotron radiation. *Sens. Actuators A*, 27(1):571–585, 1991.

[52] S. Krawczyk. Discussion on optical integration in lab-on-a-chip microsystems for medical diagnostics. *Phys. Stat. Sol.*, 0(3):998–1012, 2003.

[53] D. S. Goldman, P. L. White, and N. C. Anheier. Miniaturized spectrometer employing planar waveguides and grating couplers for chemical analysis. *Applied Optics*, 29(31):4583–4589, 1990.

[54] K. Chaganti, I. Salakhutdinov, I. Avrutsky, and G. W. Auner. A simple miniature optical spectrometer with a planar waveguide grating coupler in combination with a plano-convex lens. *Optics Express*, 14(9):4064–4072, 2006.

[55] S. Ungar. *Fibre Optics: Theory and Applications*. John Wiley & Sons Ltd., Chichester, UK, 1990.

[56] S.O. Kasap. *Principles of Electronic Materials and Devices*. McGraw-Hill, Boston, MA, second edition, 2002.

[57] R. Joray, M. Ilegems, R.P. Stanley, W. Schmid, R. Butendeich, R. Wirth, A. Jaeger, and K. Streubel. Far-field radiation pattern of red emitting thin-film resonant cavity leds. *IEEE Photonics Technology Letters*, 18(9):1052–1054, 2006.

[58] K.D. Möller. *Optics*. University Science Books, Mill Valley, CA, first edition, 1988.

[59] D. Albin, D. Rose, R. Dhere, D. Levi, L. Woods, A. Swartzlander, and P. Sheldon. Comparison study of close-spaced sublimated and chemical bath deposited cds films: effects on cdte solar cells. *Record 26th IEEE Conf. Photov. Spec.*, pages 367–370, 1997.

[60] E. Klugmann and O. E. Onyeogu. Measurement of insolation using cds photoresistor. *Energy Conversion*, 19(3):153–157, 1979.

[61] J. N. Ross. Thick-film photosensors. *Meas. Sci. Technol.*, 6:405–409, 1995.

[62] R. Schoolar. Photoconductivity in photodiodes. *Infrared Physics*, 31(5):467–474, 1991.

[63] J. R. Biard and W. N. Shaunfield Jr. A model of the avalanche photodiode. *IEEE Trans. on Electron Devices*, 14(5):233–238, 1967.

[64] F. Capasso, W. T. Tsang, A. L. Hutchinson, and G. F. Williams. Enhancement of electron impact ionization in a superlattice: A new avalanche photodiode with a large ionization rate ratio. *Appl. Phys. Lett.*, 40(1):38–40, 1982.

[65] C. Hu, K. A. Anselm, B. G. Streetman, and J. C. Campbell. Noise characteristics of thin multiplication region gaas avalanche photodiodes. *Appl. Phys. Lett.*, 69(24):3734–3736, 1996.

[66] R. J. McIntyre. The distribution of gains in uniformly multiplying avalanche photodiodes: Theory. *IEEE Trans. on Electron Devices*, 19(6):703–713, 1972.

[67] Photomultiplier tubes: Basics and applications, 3rd edition, 2006. http://sales.hamamatsu.com/assets/applications/ETD/pmt_handbook_complete.pdf.

[68] Photon counting using photomultiplier tubes, 2005. http://sales.hamamatsu.com/assets/applications/ETD/PhotonCounting_TPHO9001E04.pdf.

[69] Avalanche photodiodes: A user's guide, 2003. http://optoelectronics.perkinelmer.com/content/ApplicationNotes/APP_APDUsersGuide.pdf.

[70] I. E. Borissevitch. More about the inner filter effect: corrections of stern-volmer fluorescence quenching constants are necessary at very low optical absorption of the quencher. *J. Luminescence*, 81(3):219–224, 1999.

[71] B. C. MacDonald, S. J. Lvin, and H. Patterson. Correction of fluorescence inner filter effects and the partitioning of pyrene to dissolved organic carbon. *Anal. Chim. Acta*, 338(1):155–168, 1997.

[72] S9073, 2004. http://www.sales.hamamatsu.com/assets/pdf/parts_S/S5343_etc.pdf.

[73] Ad8627, 2004. http://www.analog.com/UploadedFiles/Data_Sheets/AD8625_8626_8627.pdf.

[74] Pic16f818, 2004. http://ww1.microchip.com/downloads/en/DeviceDoc/39598e.pdf.

[75] Tps7150, 2003. http://focus.ti.com/lit/ds/symlink/tps7150.pdf.

[76] J.W. Goodman. *Introduction to Fourier Optics*. McGraw-Hill, Montreal, Quebec, second edition, 1996.

[77] H. Sagberg. *Micromechanical optical filters for spectrometry*. PhD thesis, University of Oslo, 2005.

[78] S. D. Senturia. *Microsystem Design*. Kluwer Academic Publishers, New York, 2002.

[79] Cmc, 2005. http://www.cmc.ca/.

[80] W.-C. Shih, S.-G. Kim, and G. Barbastathis. High-resolution electrostatic analog tunable grating with a single-mask fabrication process. *J. Microelectromech. Sys.*, 15(4):763–769, 2006.

[81] J. Graeme. *Photodiode Amplifiers: Op-Amp Solutions*. McGraw-Hill, Montreal, Quebec, 1996.